國立交通大學

材料科學與工程系

碩士論文

多孔性低介電奈米群集二氧化矽薄膜結構
與性質關係之探討

Investigation on the Structure-Property Relationship of

Nano-Clustering Silica (NCS) Porous Low-k Thin Films

研 究 生：莊茹媖

指導教授：呂志鵬 博士

中 華 民 國 九 十 八 年 七 月

多介孔性低電奈米群集二氧化矽薄膜結構與性質關係之探討

Investigation on the Structure-Property Relationship of Nano-Clustering Silica (NCS)
Porous Low-k Thin Films

研 究 生： 莊 茹 媖   Student：Shindy Chuang

指導教授： 呂志鵬 教授   Advisor：Dr. Jihperng (Jim) Leu

國 立 交 通 大 學

材 料 科 學 與 工 程 系

碩 士 論 文

A Thesis

Submitted to Department of Material Science and Engineering

College of Engineering

National Chiao Tung University

In partial Fulfillment of the Requirements

for the Degree of

Master

in

Materials Science and Engineering

July 2009

Hsinchu, Taiwan, Republic of China

中 華 民 國 九 十 八 年 七 月

多孔性低介電奈米群集二氧化矽薄膜結構與性質關係之探討

研 究 生： 莊 茹 媖　　　　　　　　指導教授： 呂志鵬 教授

國立交通大學

材料科學與工程系碩士班

摘 要

　　本研究探討奈米群集二氧化矽多孔性低介電薄膜(k ~2.8 to 2.0) 由控制母體 TEOS/MTMS 比率以及結構抑制劑(起孔洞劑) TPAOH 之含量對於結構性質之關係。研究著重在結構之因素，例如：化學以及分子鍵結、孔隙率、孔洞形狀、大小、以及孔洞之分部。並且探討以上結構因素對於電性、機械性質、以及熱應力之影響。

　　NCS2~NCS5 多孔性低介電薄膜具有介電常數介於 κ =2.3~2.8。在二氧化矽(TEOS)之母體內加入了適當的甲基起始物(MTMS)。孔隙率因此隨著 TPAOH 的增加而提升，NCS2~NCS5 具有孔隙率<27%。因此 NCS2~NCS5 具有 Si-O-Si 很好的交聯程度而且孔隙率的增加並尚未破壞整個 Si-O-Si 交聯的情形，所以最終還是可達到很好的機械強度(E~10GPa)。孔洞的形貌是為圓形，且具有很窄的孔洞大小分佈並且孔洞大小皆集中在 0.5 nm。

　　為了更降低 NCS 多孔性低介電薄膜的 κ =2.0，因此 NCS1 具有較高的孔隙率 (38.6%)、Si-O-Si 交聯結構較鬆散、以及具有較低極性 Si-CH$_3$ 之鍵結，以上因素皆有利於降低介電常數。NCS1 具有大量的 MTMS (Si-CH$_3$)比起 TEOS (Si-O-Si)。儘管得到最低之 κ 值，相對而言其機械強度也受到損害(E=2.76GPa)。Si-O-Si 交聯結構較鬆散之母體中具有高孔隙率 38.6%的孔洞，則是高孔隙率以

及鬆散之母體無法撐住來自加熱過程中之熱應力而倒塌，原先圓形的孔洞也因此變成橢圓形($d_{in-plane}$ = 3.3 nm $d_{out-of-plane}$ = 1.9 nm)。

　　總結而言，控制母體的 Si-O-Si 交聯程度 (TEOS/MTMS) 以及孔隙率 (TPAOH) 是有利於增加最終的機械強度，加入適當的較低極性的 Si-CH$_3$ 鍵結和孔隙率，亦可降低介電常數且不破壞薄膜的機械強度。最後，NCS2 奈米群集二氧化矽薄膜是具有最好的薄模性質 k=2.3、E=9.2GPa 且有利於將來多孔性低介電材料薄膜進行銅鑲嵌後段製程整合的主要選擇之一。

Investigation on the Structure-Property Relationship of Nano-Clustering Silica (NCS) Porous Low-k Thin Films

Student: Shindy Chuang   Advisor: Dr. Jihperng (Jim) Leu

Department of Materials Science and Engineering

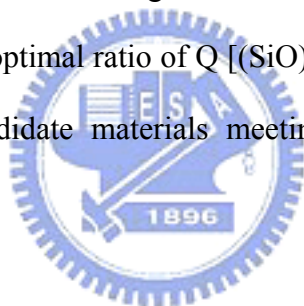National Chiao Tung University

Abstract

The structure-property relationship of nano-clustering silica (NCS) porous low-k films (k ~2.8 to 2.0) was investigated by controlling silica matrix TEOS/MTMS ratio and structure directing agent or also acted as pore generator TPAOH concentration. Emphasize had been laid on structure parameters such as the chemical and molecular bonding, porosity, pore size, pore shape and pore size distribution and the influence on ultimate electrical, mechanical, thermal stress properties.

NCS2 to NCS5 porous low-k film have κ-value ranging from κ =2.3 to κ =2.8. The silica matrix was composed by the addition of MTMS (Si-CH$_3$) in balance with TEOS (Si-O-Si). Therefore high modulus porous low-k film was obtained (E~10GPa). NCS2 through NCS5 film possessed spherical pore shape. The accommodation of Si-CH$_3$ was equilibrated by the addition of Si-O precursor, in the agreement that the Si-O-Si linkage of NCS low-k film still preserved in the present of Si-CH$_3$ groups. By adding more TPAOH, the porosity increased from NCS5 to NCS2 (ρ <27%) without causing much deterioration on mechanical modulus. Pore size was well controlled in the order of d<10nm with most population in the d=0.5nm.

In order to push κ-value <2.3, NCS1 porous low-k film was proposed with κ=2.0,

that was obtained from less cross-link structure and higher porosity. The silica matrix was composed by higher content of MTMS (Si-CH$_3$) instead of TEOS. Moreover, the incorporation of high methyl content and high porosity (ρ =38%) to NCS1 significantly reduced the κ value. But the modulus substantially dropped to E=2.76GPa. Nevertheless, its Si-O-Si cross-linking was not rigid enough and also the higher porosity cause matrix could not sustain the thermal stress, therefore collapsed to form more stable structure, and formed elliptic cylindrical pore shape (d$_{in-plane}$=3.3nm d$_{out-of-plane}$=1.9nm).

Overall, the degree of Si-O-Si cross-link (TEOS/MTMS ratio) and porosity (TPAOH ratio) must be controlled in order to obtain high mechanical modulus NCS film with low dielectric constant. Among these NCS films, NCS2 with k=2.3 and E=9.2 GPa, which possessed optimal ratio of Q [(SiO)$_4$Si] to T [(SiO)$_3$Si(CH$_3$)] group, would be the best ILD candidate materials meeting the requirements of device integration.

Acknowledgements

This thesis was carried out in the period from July 2007 until May 2009 at Department of Material Science and Engineering, National Chiao Tung University, under the supervision of Dr. Jihperng (Jim) Leu. This project was financially supported in part by Catalysts & Chemicals Industries Co., Ltd and National Science Council (Taiwan) under Contract No. 96-2221-E-009-216.

First of all, I am very grateful to join Nano-Interconnect & Package (NIP) laboratory. For these years, I am very glad to meet every members of NIP lab. NIP lab has already been my second home during my study in Taiwan. I feel very convenience and happy to be one of NIP member. I am grateful for these experiences, which have certainly influenced my own life in a significant way.

I have to express my gratitude to Dr. Jihperng (Jim) Leu for giving me the chance to manage CCIC Japan project, all kinds of discussion during the project and all priceless helps. I also would like to express my gratitude to Dr. U-Ser Jeng at NSRRC (National Synchrotron Radiation Research Center, Taiwan) for his valuable discussion about GISAXS data analysis.

I would also like to thank the seniors at NIP lab: special thank to Kima Che for his guidance and assistance, special thanks to Yu-Han Chen for his GISAXS discussion, to Kuo-Yuan Hsu for the assistance in TGA, to Hsin-Ling Hsu for every discussions about chemical part. I would like to thank every member of NIP lab for being so friendly. I would like to thank Christine Chiu, Ben Chang, Alan Tu, Gavin Liu, Tai-In Lin, Vincent Hsu, Anthony Wang, Po-Cheng Lai, Yu-Hsiu Ho, Wan-Ding Hsu for the nice office atmosphere and the fellowship at work and during the social events.

Last, but not least, I would like to thank my parents, my sisters and brother for their deep love and encouragement in all situations of my life. Also I would like to thank my boyfriend for supporting me on everything.

Contents

Table Captions

Figure Captions

Chapter 1 Introduction

1.1 Background

The downscaling of feature size in integrated circuit has developed in astonishing and remarkable rate. Such pursuit of minimization has exacerbated several difficult challenges, such as RC (Resistance-Capacitance) delay, crosstalk noise and power dissipation. [1] Presently, the utilization of copper (Cu) as a metal conductor combined with low dielectric constant (low-κ) material as an insulator has been a preferable material solution, in addition to other design solutions such as additional metal layers, repeaters, or geometrical trade-off in aspect ratio of metal and dielectric.[2] The original insulator is silicon dioxide (SiO_2) with κ= 4.2-3.9. When device dimension is reduced below 250nm, SiO_2 insulator is no longer suitable. Therefore, the need of lowering the κ-value of bulk SiO_2 can be attained by lowering the density of matrix and/or addition of lower polarizability atoms or bonds. As a result of fervent R&D of low-k material in the past decade, the development of low-κ material yielded fruitful progresses. Organic SiLK (κ=2.65) was first introduced by IBM at 0.13 μm technology node. [3] However, inorganic dielectric such as carbon-doped oxide (CDO) was adopted by the majority of semiconductor companies mainly in 90nm and beyond. Major commercially available carbon-doped oxide (CDO)s are Aurora^{TM} (κ=2.9, ASM), Coral^{TM} (κ=2.85, Novellus), and Black Diamond^{TM} (κ=2.65-3.0, Applied Materials) [4,5,6].

Since the dense low-κ dielectric has reached its lower limit of κ=2.5 [7]. Inducing porosity in low-κ dielectric material is one possible strategy to achieve κ-value<2.5. [8] Therefore, porous low-k dielectric material is critically needed and has become one of the prominent candidates. Nevertheless, the feasibility of porous low k dielectric film into Cu-interconnect still meets various kinds of integration

issues. As reported by Lin *et a.l*, [9] the CMP feasibility of a low-k material was related to its mechanical properties. Young's modulus (*E*) larger than 4 GPa and hardness (*H*) larger than 0.5 GPa were required to pass conventional CMP. Therefore, the mechanically weak porous low-k dielectric film has become the priority concern. [11, 12] They were particularly prone to damage during processes inducing stress like CMP, assembly, thermal processes and electromigration reliability test. [13, 14, 15] Particularly, porous low-k films were amorphous in nature and exhibited low mechanical modulus, such as porous carbon doped oxide that possessed k~2.3 but has modulus as low as 2.8 GPa, [16, 17] or porous spin on glass that incorporated sacrificial material into amorphous silica matrix also demonstrated low elastic modulus of < 3 GPa with dielectric constant equal to k~2.2. [18, 19].

In recent years, researchers have focused on high mechanical modulus type low-k films such as pure silica-zeolite low-k film. Pure silica-zeolite (PSZ) low-k film offered several potential advantages which including crystalline structure, intrinsically uniform and small pore size over amorphous silica. [20] Typical PSZ has high modulus and low dielectric constant, but the problems such as high surface roughness and high moisture absorption. [21] Therefore, another thrust was to advance the development of silica-zeolite type low-k film with low surface roughness and low moisture absorption by the direct incorporation of hydrophobic methyl groups such as methyltrimethoxysilane (MTMS). Hence, a modified silica-zeolite low-k materials, nano-clustering silica (NCS), was proposed by Catalysts & Chemicals Industries Co., Ltd. [22] NCS has been successfully integrated into 65nm CMOS technology by Fujitsu Ltd. [23,24,25]

The concept of NCS formation was based on zeolite MFI framework structure which yielded high elastic modulus and low dielectric constant. [26] Generally, the NCS was manufactured by hydrolyzing tetraethyl orthosilicate (TEOS) as silica

precursor in the existence of tetra-n-propylammonium hydroxide (TPAOH) as structure directing agent (SDA) or pore generator (porogen). In order to emerge the hydrophobicity, the silica precursor was modified by adding the hybrid model of methyltrimethoxysilane (MTMS) as the component of the silica matrix. [17]

The objective of this study was to explore the structure-property relationship of NCS porous low-k thin films. The structures of NCS porous low-k films were manipulated by the ratio of tetraethoxysilane/methyltrimethoxysilane (TEOS/MTMS), which control the matrix formation and hydrophobicity, and an organic structure directing agent, tetrapropylammonium hydroxide (TPAOH) loadings. Hence, the structure parameters which consisted of chemical/molecular bonding, porosity, and pore size/shape/size distribution were first investigated. Their impact on the final properties of NCS porous low-k thin film such as mechanical modulus, dielectric constant, surface roughness and residual stress were also examined. Finally, we make a thorough assessment on the structure-property relationship of NCS low-κ dielectric materials in terms of their applicability in the copper/low-k damascene processing, then make recommendation the best candidate as ILD materials.

1.2 Overview

This thesis is organized into six chapters. Following a brief introduction, Chapter 2 reviews the concepts and needs of low-k material, also accommodate our study motivation and outlook. Chapter 3 presents the experimental methods and instrumentation. Chapter 4 studies the porosity, chemical and molecular bonding environment effects on the ultimate electrical, mechanical and thermo-mechanical properties. Chapter 5 summarizes key results in this study. Chapter 6 presents a few suggestions for future study.

Chapter 2 Literature Review

2.1 Recent trends in device scaling and interconnect signal delay

The future of integrated electronics or microelectronics was firstly predicted by Gordon. E Moore in 1965 who projected that: "The number of transistors that can be placed inexpensively on an integrated circuit(IC) has increased exponentially, doubling approximately every two years ", which was also well-known as Moore's Law. [27, 28] Figure 2.1 shows the trend of various device gate length scaling. [29] Even though it only displays the front-end gate length half-pitch size trend, but it also appropriately can represent the backend interconnect feature size. The scaling itself refers to the continued shrinking in vertical and horizontal directions of chips on the purpose of improve the density (maximum production in a constant silicon area) and device performance (speed and power) under high reliability value.
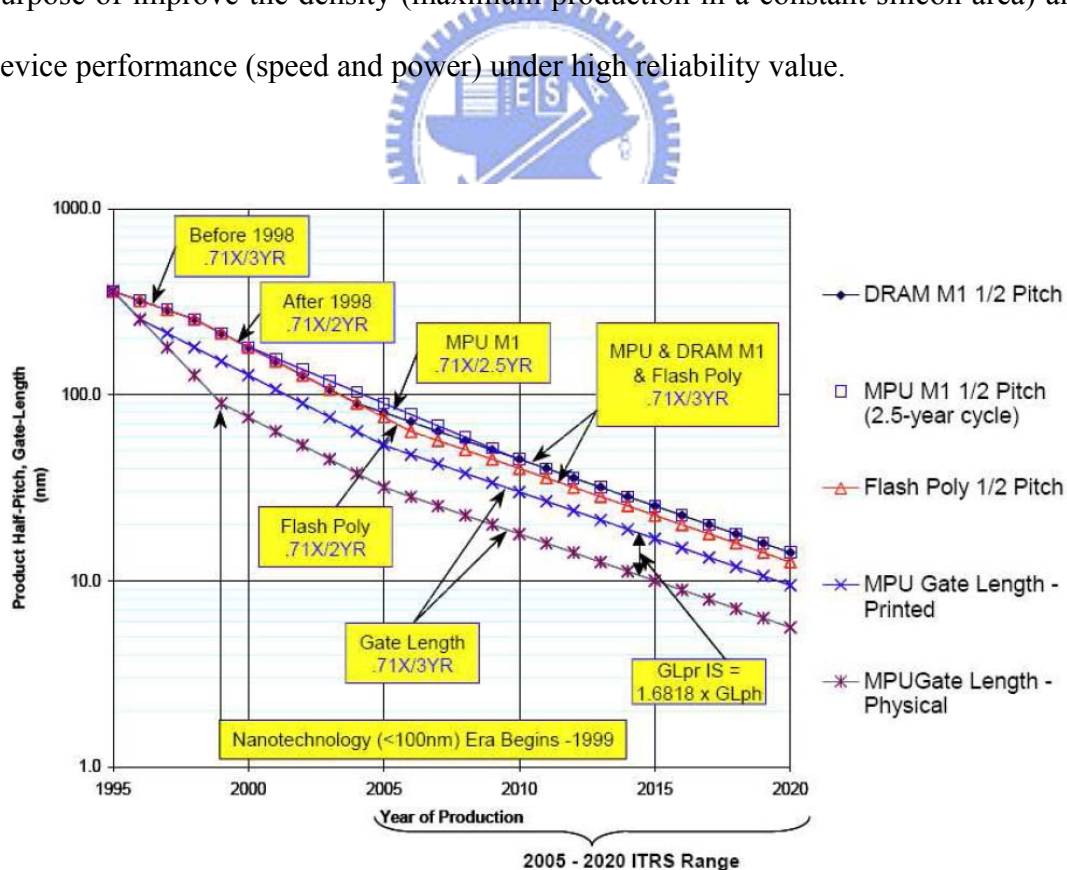
Figure 2.1 Device scaling projection trend shown in terms of gate length (half pitch) for various microelectronics products.

However, the continuous feature size shrinking has brought attention to several interconnect issues, such as resistance capacitance (RC) delay, crosstalk noise and power dissipation. Figure 2.2 shows the typical schematic interconnect cross-section with parasitic capacitance. The size reduction in line and space width of metal enlarges metal line resistance and parasitic capacitance, resulting in serious impact on signal propagation delay and crosstalk noises between metal lines of interconnect. Since one of the major signal delays is associated with interconnect delay, RC delay have become our main concern. Generally, RC delay can be described according to Figure 2.2. By assuming the minimum metal pitch is twice the metal width (W) and the dielectric thickness between the metal lines is the same as the metal height (T), the following equation can be used to predict and calculate the RC delay respectively.[30]
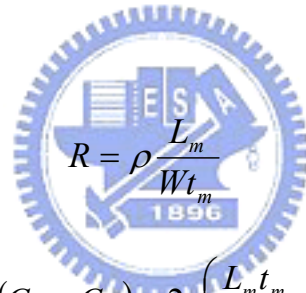
$$R = \rho \frac{L_m}{W t_m} \tag{2.1}$$

$$C = 2(C_L + C_V) = 2\varepsilon \left(\frac{L_m t_m}{W} + \frac{L_m W}{t_m} \right) \tag{2.2}$$

$$\tau = RC = 2\rho\varepsilon \left(\frac{L_m^2}{W^2} + \frac{L_m^2}{t_m^2} \right) \tag{2.3}$$

Where R is the resistivity, L_m is the interconnect line length, W is the interconnect line width, ε is the permittivity, and t_m is the thickness of metal. Continuous scaling down for achieve higher packing density will lead to the size reduction of W and tm, that will induce higher RC delay. Therefore, according to above RC delay approximation equation, proper improvement of RC delay can be achieved by modification of resistivity (ρ) of metal line and relative dielectric constant (ε) of inter dielectric layer (ILD).
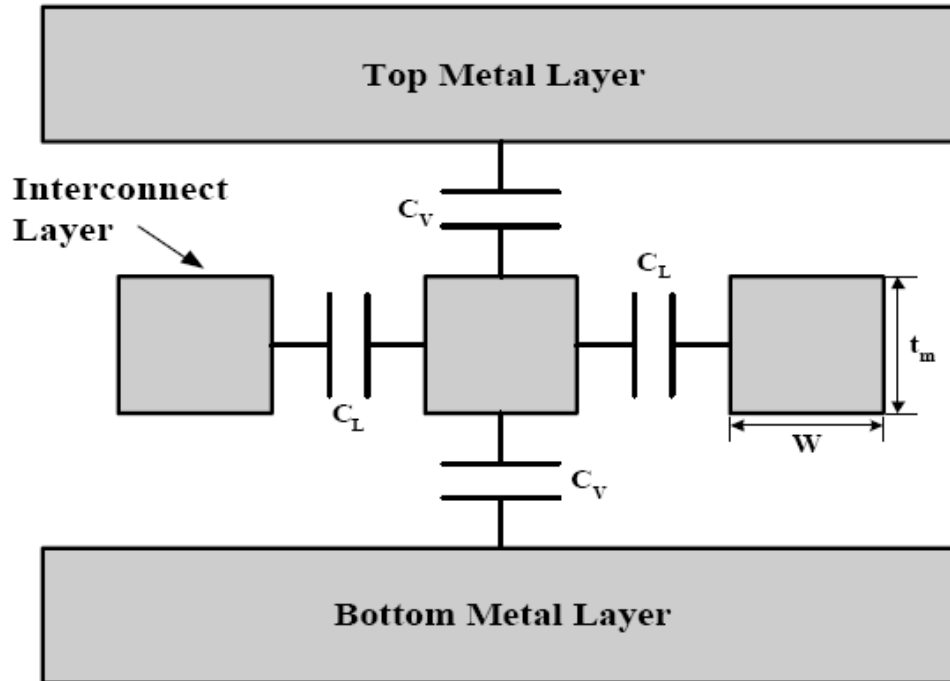
Figure 2.2 Typical schematic interconnect cross-section with parasitic capacitance

In the early dawn of integrated circuit era, the combination of aluminum (Al) alloys with ρ= 2.7 $\mu\Omega$.cm and silicon dioxide (SiO$_2$) dielectric has been utilized extensively on the interconnect on account of theirs convenient mature subtractive dry-etch processes and the production compatibility with fabricated device which have no performance issues. Even so, the relentlessly ICs marched down toward smaller geometry size in the pursuit of higher integration density and higher speed has even more demanded on material selection integration. Al/SiO$_2$ interconnect system was no longer eligible to fulfill the device geometry shrinkage requirement as shown in Figure 2.3. [1,31] To overcome above mentioned problems, new essential material with low resistivity and low dielectric constant (low-k) for apply as metal line and ILD materials are urgently needed and intensively investigated. Copper (Cu) interconnect are pronounced as one of the most prominent metallization. Possess low resistivity of ρ=1.8 $\mu\Omega$.cm, Cu-interconnect is widely developed. Lower interconnect delay is gained from Cu/low-k interconnect system compare to Al/SiO$_2$ interconnect

system, utilizing copper's 37% lower resistivity than aluminum. [32] However, when technology node has run down to 250nm, the limiting factor of Cu-implementation became obviously observe. The capacitance of interconnect is dominated by line-to-line capacitance. Therefore, a lower dielectric constant material is indeed crucially needed.
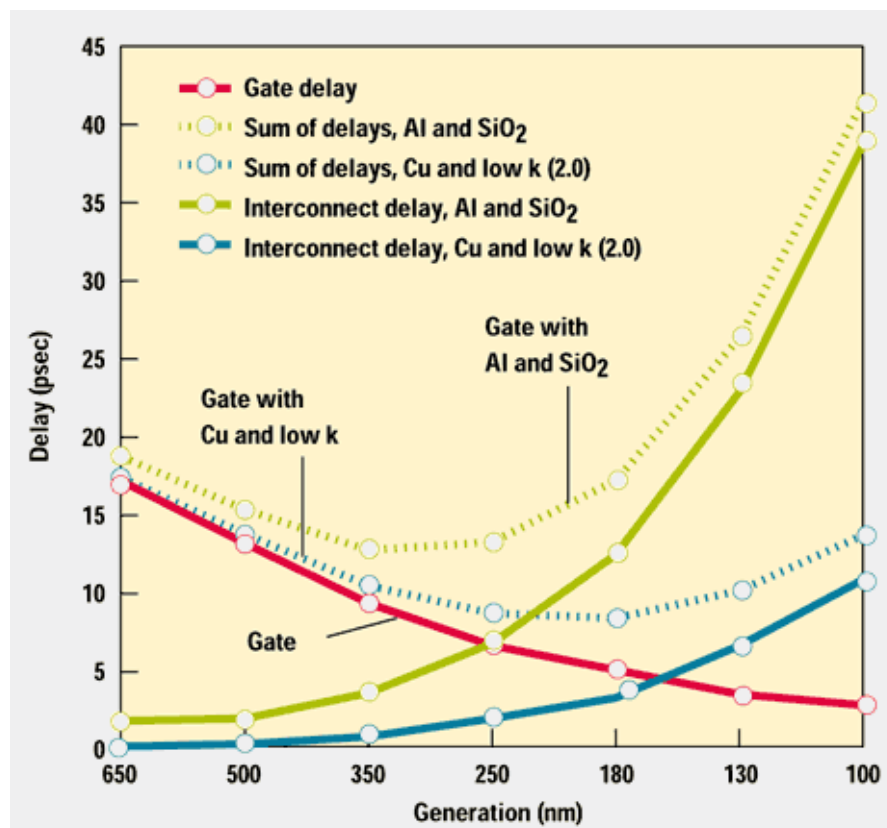
Figure 2.3 Decrease in interconnect delay and improved performance are achieved by using Cu and low-k dielectric.

2.2 Future challenges for ILD materials in interconnect processes

In recent years, the back-end ITRS roadmap was re-adjusted year to year as shown in Figure 2.4, the slope displays steeper in ITRS 1999 compare to ITRS 2005 which demonstrating the difficulties and challenges in integrating new types of ILD materials in the Cu-interconnect. The ITRS 1999 projected for 90 nm node k=2.0, but

this was later postponed for 32nm node of ITRS 2003. The ITRS stated "Introduction of new materials to….reduce the dielectric permittivity" as one of the key "Five difficult challenges through 2009" for the semiconductor industry. Therefore, low-κ material integration is closely related with the optimization between several tradeoffs, especially material properties, device architectures, and process flows. The principle driving forces for future challenge in integrated low-κ material are lower dielectric constant, minimum process cost and higher process reliability/robustness. The ultimatum for any particular technology node will be resolved by the best compromise among these 3 factors. [35]
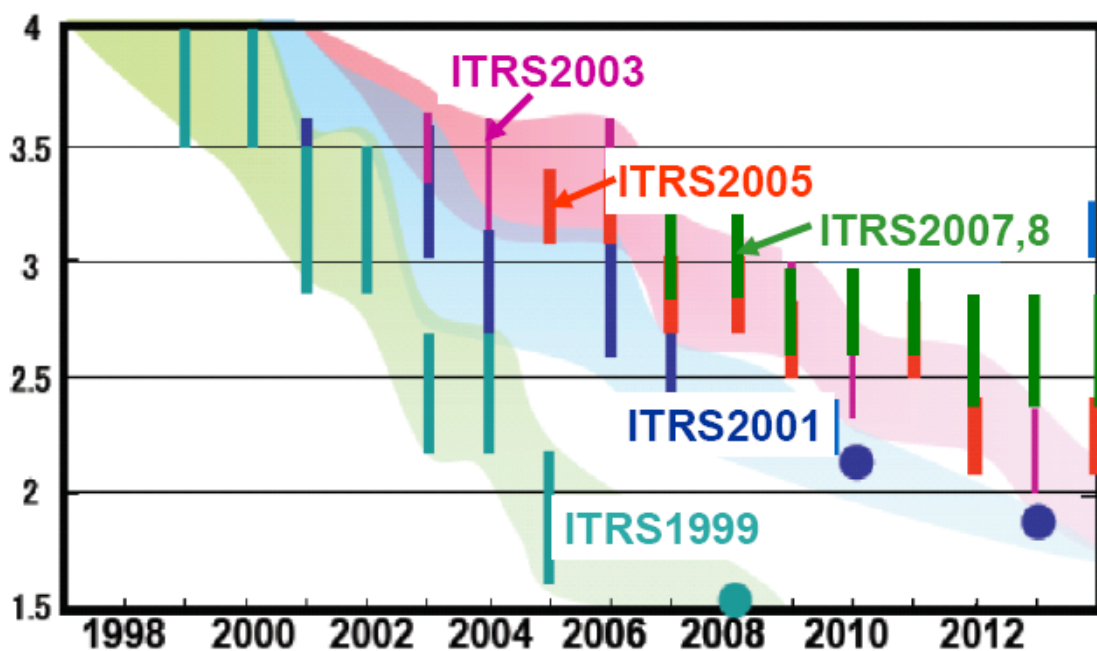
Figure 2.4 Historical transition of ITRS low-k roadmap

2.3 Definition of low-k dielectric material

2.3.1 Definition of dielectric constant

Dielectric constant (κ) (also called relative permittivity (εr)) is defined as the ratio of the permittivity of substance (ε) to that of vacuum (ε_0). When an alternating electric field is applied through two plates of capacitor/conducting plate with a

medium other than vacuum (Figure 2.5), ex. dielectric substance, the dielectric constant will therefore increase. Generally, capacitance(C) is defined as the ratio of charge ±Q on each conductor to the voltage V between them. Conductor plates area (A), by assuming the distance between those two capacitor plates is d, Thus, finalize the capacitance relationship with dielectric constant can be revealed as

$$C = \frac{Q}{V} = \varepsilon \frac{A}{d} = \kappa \varepsilon_0 \frac{A}{d} \tag{2.4}$$

In which ε_0 is the permittivity of vacuum (ε_0=8.845.10^{-12}F/m). Consequently, the capacitance is greatest in devices made from materials with a high permittivity.
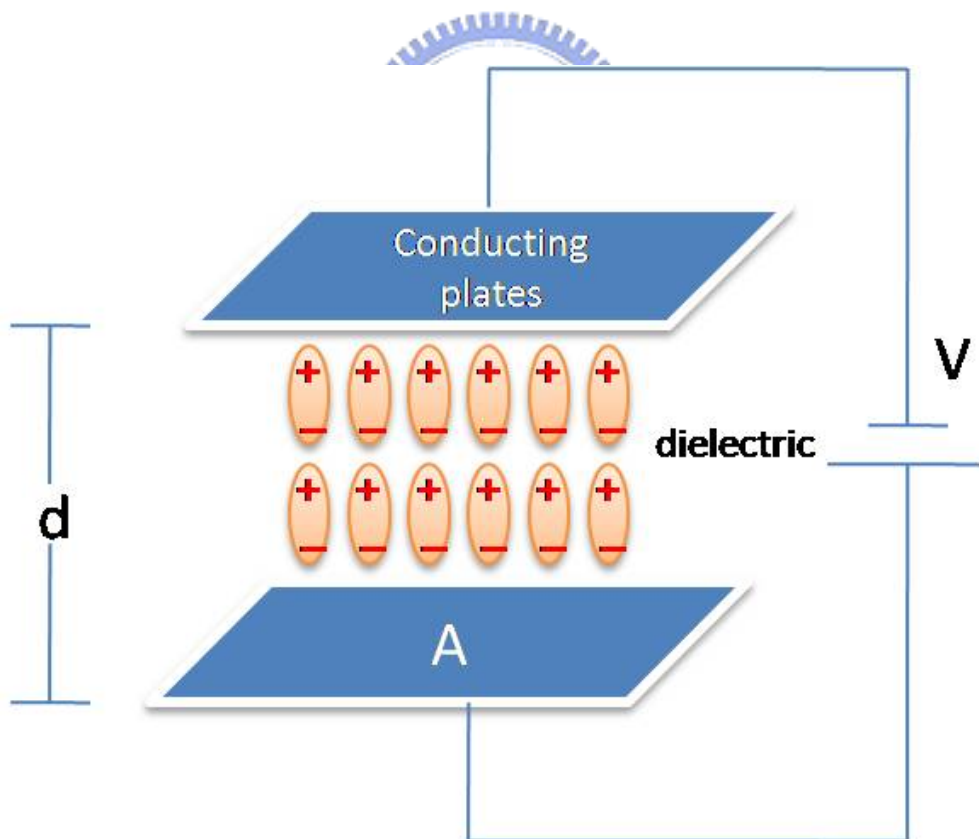
Figure 2.5 Dielectric is placed between two conducting plates, each of area A and with a separation of d.

2.3.2 Polarization contribution to dielectric constant

Any kind of materials containing polar component is represented as dipoles (separation of positive and negative charge in the present of electric field). Dipoles can be characterized by their dipole moment. Many molecules (polar chemical bond) have such dipole moment. From Figure 2.6 which shows the dipoles formation is build up from electronic polarization, ionic polarization and orientation polarization. [36] Electronic polarization is due to the separation of positive charges from negative charges in atoms or molecules of dielectric material due to applied electric field. Ionic polarization occurs in ionic solids whose the dipole moment is disrupted by the application of electric field. Orientation polarization happens in polar dielectric material, which posses permanent electric dipoles. The relationship between polarizability and dielectric constant can be approximately explained by Clausius - Mossotti equation (eq. 2.5) [37] below

$$\frac{\varepsilon_r - 1}{\varepsilon_r + 2} = \frac{1}{3\varepsilon_0}\left[N_e\alpha_e + N_i\alpha_i + N_{dip}\alpha_{dip}\right] \qquad (2.5)$$

Where ε_r is the relative permittivity or dielectric constant, α_e is the electronic polarization, N_e is the number of atoms/ions per unit volume exhibiting electronic polarization, α_i is the effective ionic polarizability per ion pair and N_i is the number of ion pair per unit volume. N_{dip} is the number of permanent electric dipole, and α_{dip} is the dipole orientation polarization.
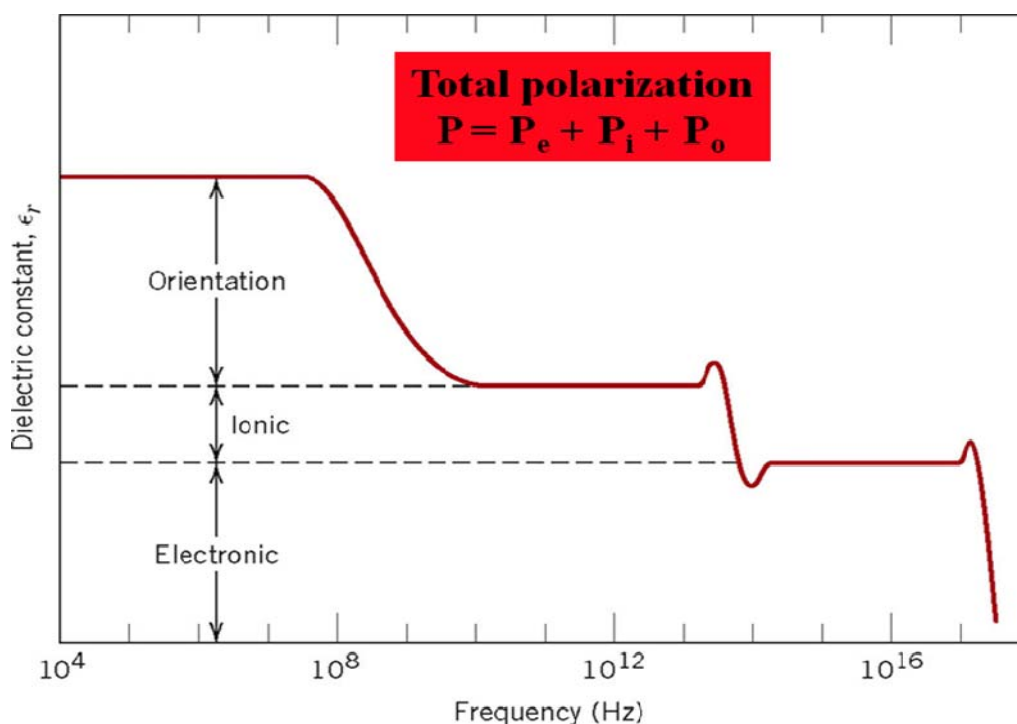
Figure 2.6 Variation of dielectric constant with frequency of an alternating electric field. Electronic, ionic, and orientation polarization contribution to the dielectric constant are indicated.

2.3.3 Chemical compound and density reduction

General bond electronic polarizabilities and related bond enthalpies are listed in Table 2.1. [38] The minimum of polarizability is achieved by single C-C bond. Thereby C-C aliphatic hydrocarbon is being the one of the great potential for low dielectric. Low dielectric might also be obtained by element with small configurational such as smaller atomic radii ex: C-F, C-O and C-H bonds. Conversely, bonding such as C=C double bond or triple bond, need to be avoid, since those bonds have larger polarization due to its increase mobility in π electrons. Although bond enthalpy reveals higher value for double bond and triple bond, which will be an advantages to the higher bond strength compare to single bond. Thus, trade-off stays between lower polarizability that has weaker bond strength while higher bond enthalpy which has higher polarizability.

11

Table 2.1 Polarizability and bond enthalpy of some chemical bonds

Bond	Polarizability ($Å^3$)	Bond enthalpy (kcal/mol)
C–C	0.531	83
C–F	0.555	116
C–O	0.584	84
C–H	0.652	99
O–H	0.706	102
C=O	1.020	176
C=C	1.643	146
C≡C	2.036	200
C≡N	2.239	213

Instead of bonding polarity influence on reduction of dielectric constant, the density of low-k film also one of the dramatic concern. To lower the density can be achieved through increasing the free volume by rearranging the material main structure or introducing porosity. In term of porosity itself, can be divided into constitutive or subtractive. Constitutive porosity indicates to the self organization of the material, the porous structure is formed without any additional treatment. Pore size less than 2nm usually observed for constitutive porosity and the porosity is relatively low (<15%). Subtractive porosity involves the addition of thermally degradable substance call porogen. Porogen means pore generator which can induce pores in the material after subsequently removal by an annealing process. Pore size ranging from 2nm to tens of nanometers observes for subtractive porosity and the porosity can reach as high as 90%. [39] As a conclusion, organic polymer can combine three approaches. Those include low polarizability bonding, constutive porosity (introduction of free volume) and the use of porogen by subtractive porosity.

2.4   Classification of low-k dielectric materials

2.4.1 Deposition Method of low-k dielectric materials

Generally, the major deposition techniques for formation of ILD are divided into primary chemical vapor deposition (CVD) known as "dry" process which has been widely adopted by chip manufacturers and showed highly reliable. The second one knows as "wet" process called spin-on method which has not been greatly developed in the process. There are some trade-off between CVD method and spin-on method. Spin-on process simply involves the coating of liquid/viscous precursor on the substrate before final curing to remove the solvent. It provides planarizing property that shows in a smoother surface which is highly desirable. Compare to CVD method which involves various gases flow and deposit on the substrate, this benefit on cleanliness and minimal waste production. CVD method also provides better conformal coverage of the topography. Table 2.2 listed the CVD and spin-on of various ILD materials with their dielectric constant value. [40]
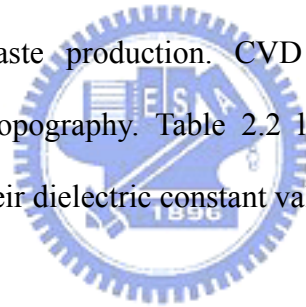
Table 2.2 Type of ILD materials

Material	Dielectric constant	Deposition method
	Low-k materials	
Polyimides	3.0-3.6	Spin-on
Spin-on glasses	2.7-3.1	Spin-on
Fluorinated polyimides	2.6-2.9	Spin-on
DLC (diamond-like carbon)	2.8-3.0	CVD
Hydrogen silsesquioxane (HSQ)	2.8-3.0	Spin-on
SILK ^{TM}	2.7	Spin-on
Black Diamond ^{TM} (SiCOH)	2.7-3.3	CVD
Poly(arylene ethers)	2.6-2.9	Spin-on
Poly(arylenes)	2.6-2.8	Spin-on
Methyl silsesquioxane (MSQ)	2.6-2.9	Spin-on
Poly(norbornenes)	2.5-2.7	Spin-on
Fluorinated Parylene	2.5	CVD
Polyimide-SSQ hybrids	2.7-3.0	Spin-on
	Ultralow k	
Teflon microemulsion	1.9-2.1	Spin-on
	Porous dielectrics	
Polyimide nanofoams	2.2	Spin-on
Silica aerogels	1.1-2.2	Spin-on
Silica xerogels	1.5-2.2	Spin-on
Mesoporous silica	1.9-2.2	Spin-on
(Source:IBM)		

2.4.2 The candidate for low-k dielectric materials and related issues.

2.4.2.1 Fluorinated Silicates Glasses (FSG)

The first generation of low-k material were fluorinated silicate glasses (FSG) invented by Novellus System Inc. FSG has dielectric constant value as low as k=3.6. FSG posses lower dielectric constant than SiO_2 due to incorporation of fluorine into SiO_2 matrix film. Fluorine incorporation leads to a less dense, more porous film by creating voids in the SiO_2 matrix. Typical FSG film matrix shows in Figure 2.7. Replacing Si–O in the SiO_2 matrix with Si–F reduces the polarizability of the matrix. The above reasons contribute to a lower dielectric constant of the FSG dielectric layer. [42, 43] FSG film has some drawback, for instance SiOF film is hydrophobic, in the meantime the fluorine atom will tend to react with hydrogen atom from water absorb in the release of HF moisture when heated to elevate temperature. The moisture of HF will travel along the interface of ILD and metal causing adhesion become poorer as explained by Figure 2.8. [44]
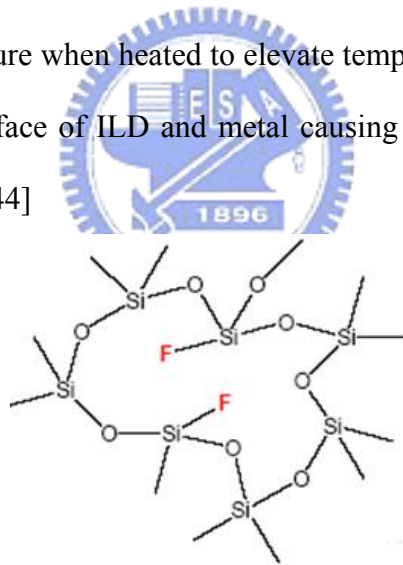
Figure 2.7 Basic structure of FSG matrix
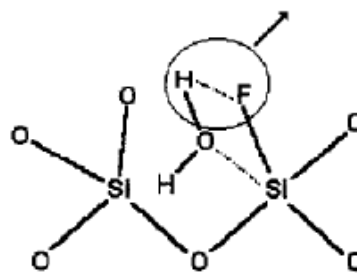
Figure 2.8 Depiction of possible bond rearrangements upon SiOF film hydration to produce Si-OH bonding and the release of HF from the film

2.4.2.2 Silsesquioxane (SSQ) based

Silsesquioxane (SSQ) based low-k material or commonly called T-resin are organic-inorganic polymer with empirical chemical formula $RSiO_{1.5}$. The substituents (R) can include hydrogen, alkyl, alkenyl, alkoxy and aryl. The contribution of these organic substituents benefit in lowering the dielectric constant because they provide lower density of the matrix structure. For the addition, they also attributed to less polarizability organic bond ($Si-CH_3$) compare with Si-O bonds in SiO_2. SSQ based low-k also known as organosilica glasses (OSG) which yield k=2.7-3.0. The common used SSQ based materials for microelectronic application are mainly hydrogen-silsesquioxane (HSQ) and methyl-silsesquioxane (MSQ). HSQ has hydrogen as a terminal group and MSQ has methyl as a terminal group. The structure of basic units of SSQ shows in Figure 2.9. [45]
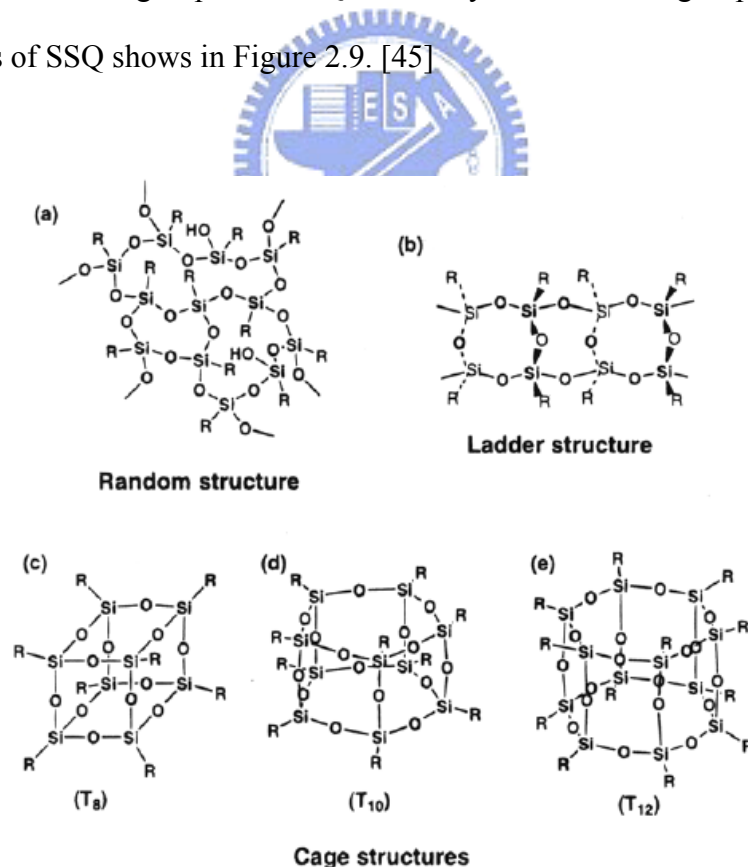
Figure 2.9 Basic structure units of SSQ dielectric materials consist of random, ladder and cage structures. R= H, CH_3 for HSQ and MSQ respectively.

MSQ material has lower dielectric constant compare to HSQ. The contribution of larger –CH$_3$ group that will cause steric hindrance rather than smaller –H group will lower the density of MSQ matrix. The Si-CH$_3$ bond is also a less polarizable bond compare to Si-H. Thus greatly reduce the dielectric constant of MSQ. Table 2.3 summarizes the principle properties of SSQ based dielectric materials compare with SiO$_2$. Subsequently, the commercially available SSQ based low-k materials are summarized in Table 2.4 which has k < 3.0. [46, 47]

Table 2.3 Principle properties of SSQ based dielectric materials (ref)

Property	MSQ	HSQ	SiO$_2$
Dielectric Constant κ	2.8	3.0	4.0
E Modulus (GPa)	3-5	6	59
Density (g/cm^3)	1.2-1.3	1.4-1.5	2.4
Tensile Strength σ (MPa)	50	80	-

Table 2.4 Commercially available SSQ-based low-k materials (ref)

Material	Trade Name	k-value	Company
HSQ	Fox (flowable oxide)	2.9-3.0	Dow Corning
MSQ	RZ25-15	2.6	Hitachi
MSQ	HOSP	2.6	Honeywell
Porous HSQ	XLK	2.2	Dow Corning
Porous HSQ	LKD 5109	2.2-2.3	JSR
Porous MSQ	Zirkon	2.3	Shipley

2.4.2.3 Carbon-doped oxide (CDO)

Basically, CDO manage to utilize the chemical vapor deposition (CVD) processing method. CDO low-k is also often designated as SiCOH (carbon-doped silicon oxide). The CDO matrix exists organic bonding such as CH_3 backbone that concern lower polarizability in comparison to Si-O as shows in Figure 2.10. Instead of lower polarizability, CH_3 also reduce the density of matrix by induced the matrix steric hindrance. Regardless of the precursor used, SiCOH can reach k value in the range of 2.4-3. The k-value depends on the number of CH_3 groups build into the structure. The widely studied precursor for SiCOH low-k have been deposited by CVD methods were monometylsilane (1MS), dimethylsilane (2MS), trimethylsilane (3MS), tetra-methylsilane (4MS), Hexamethyldisiloxane, (HMDSO), bis-trimethylsilylmethane (BTMSM), tetravinyltetramethylcyclotetrasiloxane (TVTMCTSO), Vinyltrimethylsilane (VTMS), and tetramethylcyclotetrasiloxane (TMCTS) [48, 49, 50, 51, 52, 53, 54]

CVD CDOs are mainly use in 90nm node. Commercially, the most common CVD OSG materials are Aurora[TM] (k=2.9, ASM), Coral[TM] (k=2.85, Novellus), Black Diamond[TM] (k=2.65-3.0, Applied Materials). [55, 56]

(a)   (b)
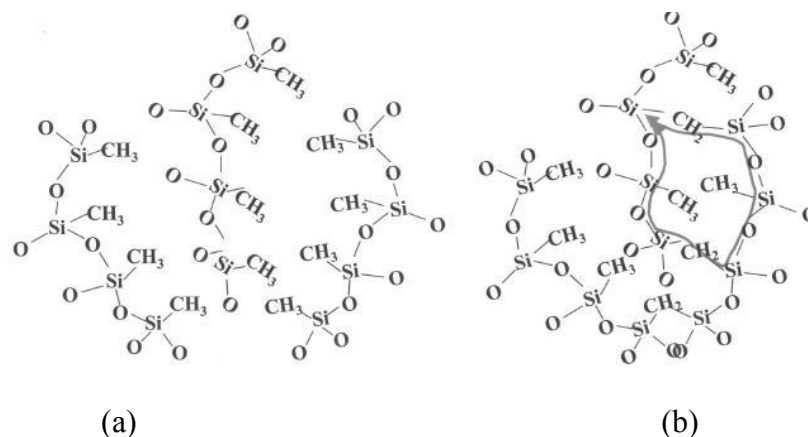
Figure 2.10 Carbon-doped silica glass and schematic bonding structure (a) before and
(b) after cross-linking

2.4.2.4 SiLK[TM]

Spin-coated base SiLK[TM] was an organic polymer dielectric founded by Dow Chemical in mid 1997. In April 2000, IBM reported the complete integration of SiLK[TM] dielectric and copper wiring, and announced its intent to commercially fabricate integrated circuits using SiLK[TM] resin. Toshiba/Sony and Fujitsu also accommodated SiLK resin with hybrid stacks. Aromatic thermosetting polymer SiLK[TM] with k=2.65 has been proved its compatibility with Cu-dual damascene 0.13 um technology node system. [57] However, the relatively weak mechanical properties of SiLK[TM] and its poor mismatch of coefficient of thermal expansion (CTE) with copper wires and substrates have prevented a wide adoption of SiLK[TM] in high-volume semiconductor manufacturing. The comparative properties of SiLK with SiO_2 are shown in Table 2.5. [3] Structure repeating unit of organic SiLK[TM] shows in Figure 2.11. [58]
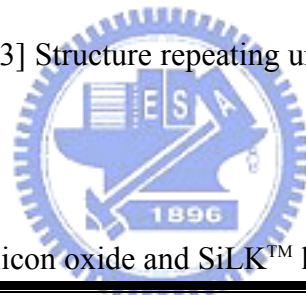
Table 2.5 Key properties of silicon oxide and SiLK[TM] low-k material.

Properties	SiLK[TM]	Silicon Oxide
Platform	Spin-on organic polymer	SiO_2
Dielectric constant, k	2.65	3.9
Elastic Modulus (GPa)	3	55 to 70
CTE (ppm/^{o}C)	66 to 165	0.45
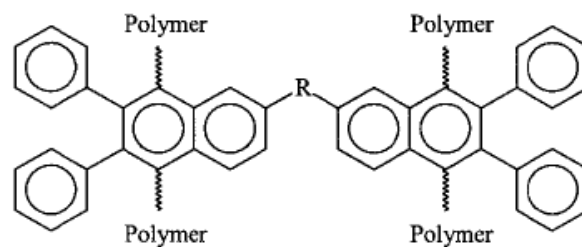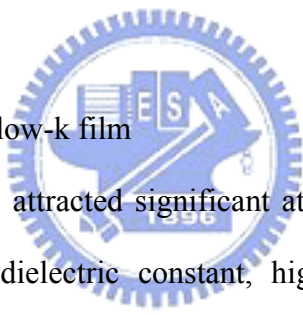
Figure 2.11 Organic SiLK[TM] chemical structure units

2.4.2.5 Porous low-k materials

The above mentioned low-k materials were all classified into dense low-k materials. In order to reach k<2, fully densified materials has seemingly reached theirs lowest capability. Hence, the research has to move on with introduction of porosity onto the dense materials. There are two type pore formation inside the dense low-k matrix. The primary one is pores that are inherently formed inside the matrix through sol-gel process, ex: aerogel and xerogel low-k film. The secondary one is formed though the template type which accommodate the present of sacrificial materials which are also called "porogen" or pore generator that are decomposed upon the thermal process. Following we will discuss the fact and issue of each porous low-k materials.

1. Silica aerogel and xerogel low-k film

SiO_2 aerogel thin film has attracted significant attention because of their unique properties such as ultralow dielectric constant, high porosity, and high thermal stability. SiO_2 aerogel thin films usually take the advantage of aging processes. However, SiO_2 aerogel thin films usually synthesis above the supercritical pressure (>60 bar) and high temperature of drying solvent process, which is very expensive and hazardous. Thus, it will become constraint for the production in industrial application. [59] Due to their high porosity, SiO_2 aerogel thin film have not display superior mechanical properties. [60] SiO_2 xerogel thin films also employ the same aging technique as SiO_2 aerogel thin film. The differences between aerogel and xerogel is SiO_2 xerogel prepared by the ambient drying process which involve pre-drying step that called surface modification process known as silylation. The intention of silylation process is to change the surface hydroxyl (-OH) groups into inert methyl (-CH_3) groups. This procedure ensure the film absorb minimal moisture

20

from the environment. [61] Both SiO_2 xerogel and aerogel has been reported to reach k-value <2 at porosity level of 70-90%. [, 62, 63, 64, 65]

2. Template-type (porogen) low-k films

Furthermore, the incorporation of thermally-labile pore generator also can produce porous SiO_2 thin film. The removal of porogen upon high temperature heating will be replaced by pores inside the matrix of SiO_2. First method, incorporation of porogen into the SiO_2 matrix can be accomplished by simply dispersing or mixing the porogen into the solution of SiO_2 precursor. [66, 67, 68] Porogen size determines the final pore size that exists inside the matrix. Percentage of porogen added or also called porogen loading determines degree of porosity inside the final cured matrix. [69, 70] However, during thermal heating process, the random distribution of pores tends to agglomerate and coalescence which cause a burden to the mechanical strength of final SiO_2 film especially when the porogen loading is increased as shown in Figure 2.12. [71, 72] The mechanical property of porogen templated low-k film results on lower elastic modulus, the present of porogen in the surrounding of silanol matrix will disturb the condensation of silanol groups (2SiOH➔Si-O-Si+H_2O) to form Si-O-Si skeleton. Since Si-O-Si skeleton cross-linking determines the modulus of film, therefore the incorporation of higher porogen loading to obtain lower κ will cause the deterioration of film modulus. [73]. Second method, the porogen is chemically linked or grafted to the SiO_2 polymer. [74, 75, 76] This method can achieve better control of porogen distribution in the SiO_2 dielectric film. Porogen selection must compatible with SiO_2 matrix precursor in order to avoid phase separation. Closely to this theory, phase separation method can be utilized when choosing the suitable porogen.
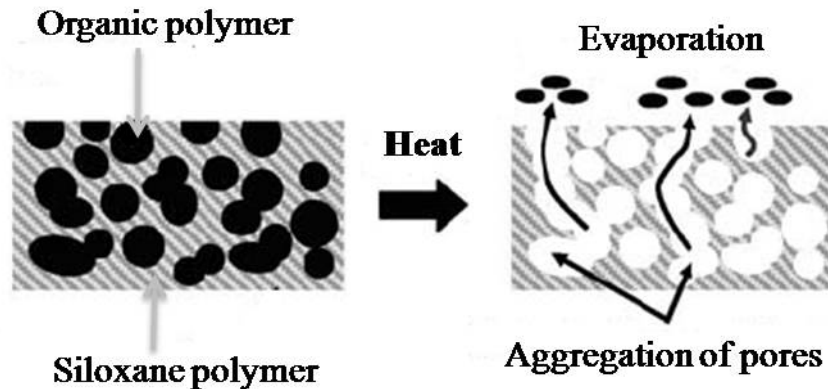
Figure 2.12 The conventional formation of porous low-k by using template-type
porogen method.

Recently studies have shown that various organic or inorganic polymer could be
applied to form more ordered pore size and pore shape with narrower pore size
distribution. Regarding to their ability to self assembly and form micelle when the
thermal curing process takes place, block copolymers have become one of the
promising candidates for low-k dielectric. Amphibilic di-(or tri-) block copolymer
such as PEO-b-PPO-b-PEO [77], PS-b-PEO [78], PS-b-P2VP [79], PS-b-P4VP [42],
etc have been studied widely. Various nanoporous low dielectric films have been
realized using poly(methyl silsesquioxane) (PMSSQ) as a matrix material with a wide
variety of pore generating materials (porogens) such as star-shaped polymers
(Polycaprolactone (PCL)) [80, 81, 82], block copolymers [83, 84], cyclodextrines
[85, 86, 87], norbornenes [88, 89], dendrimers [90, 91], and hybrid type porogens
[92, 93, 94, 95].

Another way to overcome the aggregation issue of porogen is by adopting fast
curing and slow curing process [96]. Slow ramp-curing allows porogen diffusion and
slow matrix cross-linking. During this curing, porogen percolation leads to form
surface agglomerates. Using faster ramp curing, the matrix is cross-linked around
porogen nanoparticles faster, and afterward the porogen is degraded at high
temperature to leave a network of nanopores in a rigid ULK dielectric matrix.

Controlling Curing temperature and ramping rate are important factor for nanoporous ULK dielectrics quality. [96] Moreover, alternative curing process, such as UV, or e-beam assisted thermal cures, would be helpful in providing good film performance. [97, 98] For example, UV radiation could be used to break porogen bonds, leading more easily to their extraction and it also promotes cross-linking that will improve mechanical modulus. [99] The problem that UV-cure meets in the packaging process is the increase in film stress that will cause cracking of film stack and delamination. [100] Therefore, the entire list of the UV cure performance specifications that ultimately determine the quality of the UV cure process must be considered. [101] E-beam assisted thermal cure can improve crosslinking, but it also causes charge damage. [102]

2.4.2.6 Pure Silica-Zeolite low-k film (PSZ-LK)

　　Pure silica zeolite low-k films (PSZ-LK) have been pronounced as a promising low-k material. A key advantage of PSZ was the ability of decreasing κ value while maintaining much higher mechanical modulus compare to amorphous porous low-k materials. The PSZ has been investigated to possess two film-deposition processes: in situ crystallization and spin-on of a zeolite nanoparticle suspension. [16,103,104, 101,102,103]　 The in-situ films were pure zeolitic silica films that clearly revealing the intrinsic property of zeolites. The spin-on films were composites of PSZs and amorphous silica which were not totally the intrinsic properties of pure zeolites. Nevertheless the spin-on films have the advantage of obtaining a k-value in the ultralow-k range. Moreover, the spin-on deposition technique was more viable for the manufacturing of integrated circuit. The silica zeolite coating film having the MFI crystalline structure has elastic modulus of 16 to 18 GPa with κ=2.3 [105,106]. The PS-ZLK was developed to take advantage of both the intrinsic zeolite mircoporosity

(d=0.55nm) and interparticle mesoporosity (d=2.7-3.3nm). [107] Figure 2.13 depicted

the comparison of amorphous silica with PSZ modulus (E) versus dielectric constant

(κ) plot. [15,108] It was obvious that PSZ low-k film offered a significantly superior

elastic modulus to amorphous silicas at any given k-value.
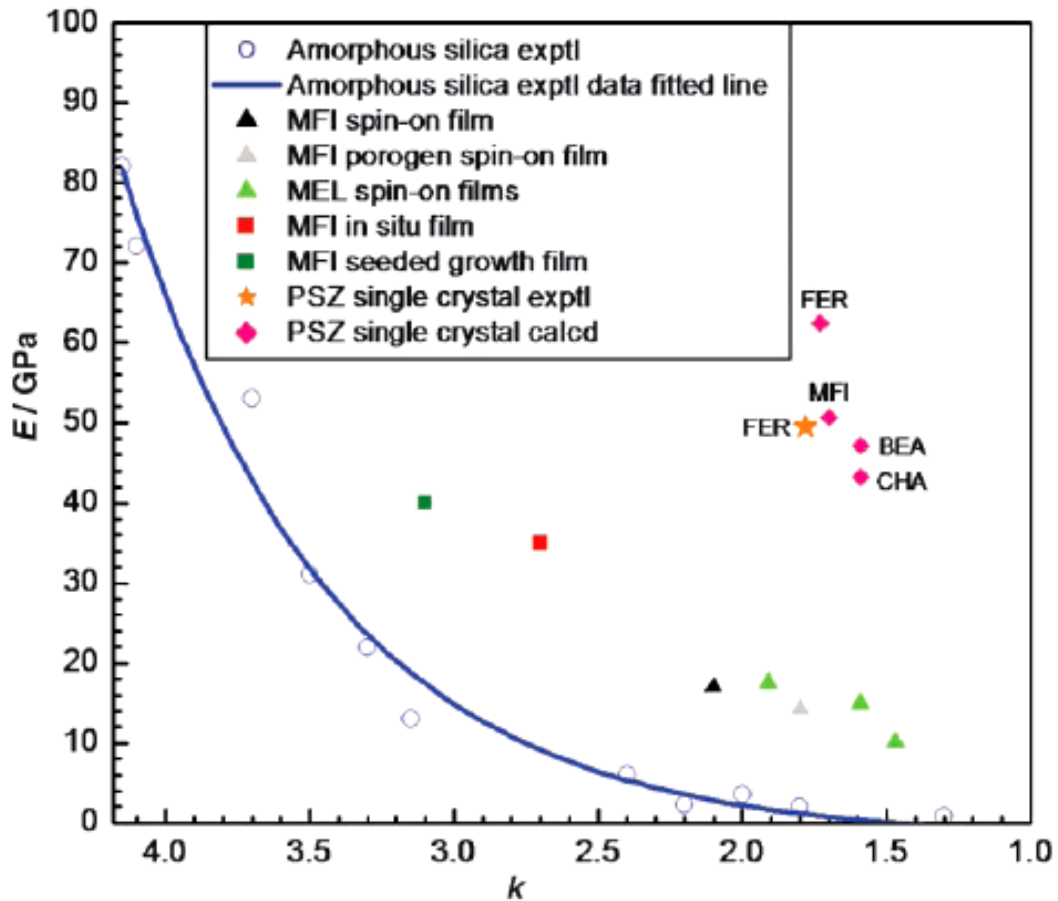
Figure 2.13 Elastic modulus (E) vesus dielectric constant (κ) for amorphous silicas
          and various PSZ

The major problem of this high elastic modulus PSZ low-k film was the

moisture-absorption was too high. [109, 110] The κ rapidly increased from 2.3 to 3.9.

Absorption of moisture could result in significant increase of κ because of water has a

very high κ (κ=80-90). This was disadvantageous lost for the practicability of PSZ

film. Therefore, there have been some efforts to overcome this problem such as extra

post spin-on treatment, by subjecting the PSZ film to silylation (vapor phase silylation

using chlorotrimethylsilane (CTMS) or hexamethyldisilazane (HMDS)) to make the surface become more hydrophilic. [111, 112]. Overall, the disadvantages of PSZ low-k film were:

a.   Although silylation step was effective, it was considered highly undesirable in semiconductor industry because silylation step was an extra step. It would also increase the manufacturing cost.

b.   The silylation step was only hydrophobized the surface of PSZ low-k film. It was also some difficulty for CTMS or HMDS molecules to diffuse into the pore of MFI (micropore=0.55nm). Therefore may have difficulty in assessing the silanol groups inside the micropore. [113] This was inevitably when the PSZ low-k film was subjected to etch or ash process; it would cause the moisture absorption inside the pores and worsen the κ.

c.   The size of zeolite particles was around 40-70nm. [114] The surface obtained from zeolite coating film was substantially rough. For instance, further polishing was needed to smooth the surface. This would also increase the manufacturing cost.

2.4.2.7 Nano-Clustering Silica (NCS)

A novel pore forming method based on spin-on nano-clustering silica (NCS), schematically illustrated in Figure 2.15. [20] The nano-clustering silica, a MFI-type zeolite film was prepared by sol-gel method. NCS precursor prepared by mixing main matrix of silica source tetraethoxysilane (TEOS) as a soldier in the existence of organic structure directing agent such as tetrapropylammonium hydroxide (TPAOH) as a commander in the present of appropriate solvent such as ethanol. The hydrophobicity of the surface of precursor was modified by adding alkoxysilane (AS) such as methyltrimethoxysilane (MTMS) as a component of the matrix. The

difference between pure zeolite low-k and NCS is the addition of methyl (-CH$_3$) groups directly into the precursor.

The sol-gel preparation composed of two steps:

1. The hydrolysis of TEOS and MTMS

   $Si(OC_2H_5)_4 + H_2O \rightarrow (C_2H_5O)_3Si\text{-}OH + C_2H_5OH$

   $H_3CSi(OCH_3)_3 + H_2O \rightarrow (CH_3O)_2Si\text{-}OH + CH_3OH$
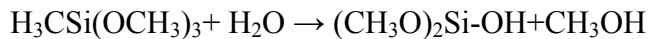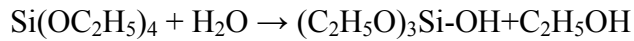
2. Water Condensation reaction

   $(C_2H_5O)_3Si\text{-}OH + (C_2H_5O)_3Si\text{-}OH \rightarrow (C_2H_5O)_3Si\text{-}O\text{-}Si(OC_2H_5)_3 + H_2O$

   $(C_2H_5O)_3Si\text{-}OH + (CH_3O)_2Si\text{-}OH \rightarrow (C_2H_5O)_3Si\text{-}O\text{-}Si(OCH_3)_2 + H_2O$

3. Alcohol Condensation

   $(C_2H_5O)_3Si\text{-}OC_2H_5 + HO\text{-}Si(OC_2H_5)_3 \rightarrow (C_2H_5O)_3Si\text{-}O\text{-}Si\text{-}(OC_2H_5)_3 + C_2H_5OH$
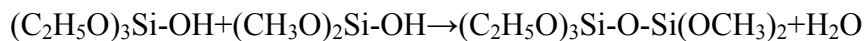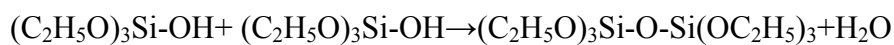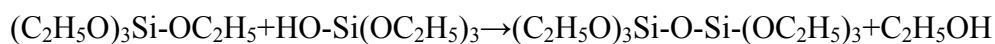
Water and ethanol were produced by the formation of siloxane (Si-O-Si) bonding. To avoid the formation of striation in the spin-on films due to low boiling point solvents present in the suspension ex: water, ethanol, and methanol. Therefore, solvent substitute processes were followed after sol-gel process by replacing with propylene glycol monomethyl ether (PGME) and propylene glycol monopropyl ether (PGP).The addition of aqueous TPA$^+$OH$^-$ would promote the hydrolysis of TEOS due to nucleophilic displacement reaction (SN2-type mechanism) as following mentioned [115]
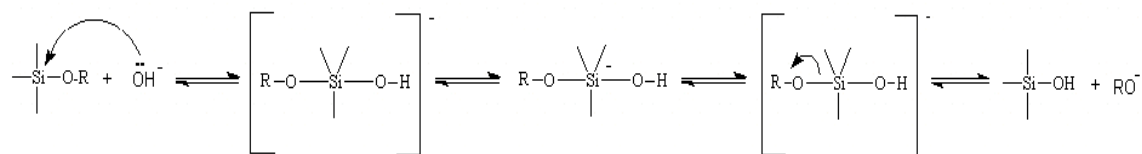
Figure 2.14 Base-catalyzed hydrolysis by nucleophilic displacement
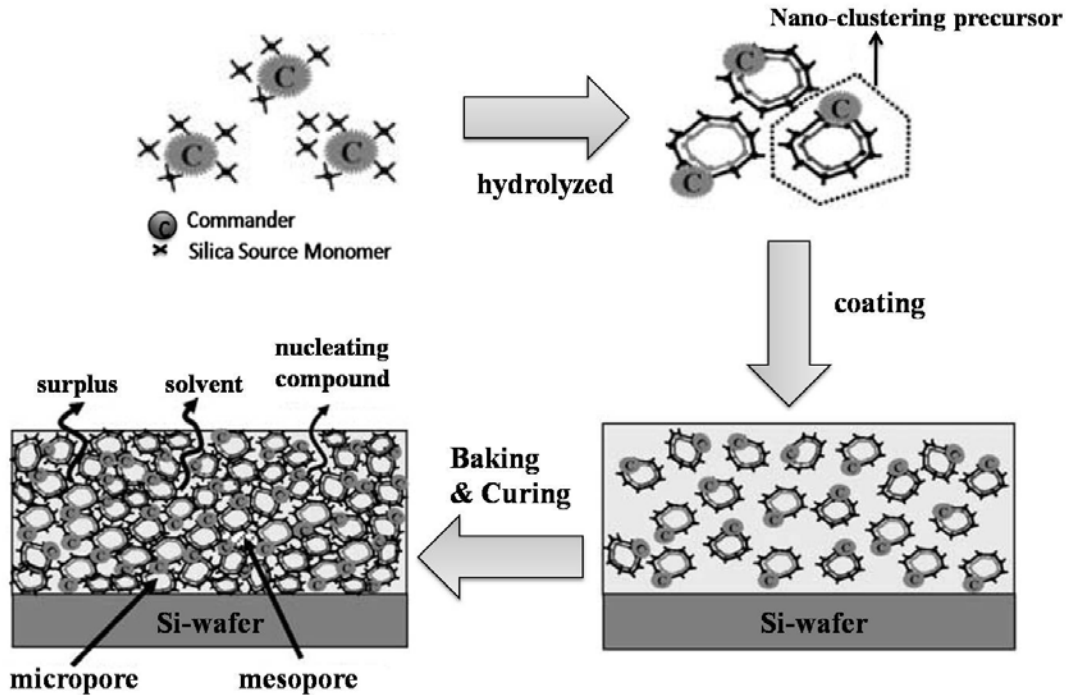
Figure 2.15 Schematics of the nano clustering silica formulation and its film deposition and curing processes.

2.5 Structure-property relationship of common porous low-k films

From above reviewed, porous low-k material was obtained through the incorporation of pores into the dense matrix. Generally the incorporation of pores would sacrifice the elastic modulus of the porous low-k film. The most common PECVD deposited carbon doped oxide film has $\kappa= 3\sim2.5$ with modulus higher than 10GPa, along with the incorporation of 35% porosity, the modulus was largely dropped to 2.8GPa if the porogen was removed through furnace curing. Nevertheless, the low modulus of furnace curing could be improved through e-beam treatment which could increase the modulus to 5.8 GPa with $\kappa= 2.3$. The modulus of was improved due to higher network/cage ratio of e-beam treated film compared to furnace cured. [116] From theoretical investigation also revealed the same behavior, higher crosslink of hydrocarbon components instead of terminal methyl groups (-CH$_3$ group) would improved the mechanical strength without adversely affecting the small

27

dielectric constant. [117] The incorporation of more methyl groups was beneficially in reducing the dielectric constant since by replacing the Si-O by Si-CH$_n$ bonds would also increasing the porosity, as Si-CH$_n$ bonds could generate voids. The nano-voids formed due to the steric hindrance offered by Si-CH$_n$ bonds. [118, 119] As the porosity of porous SiOC:H films increase approximately 30-60%, the modulus decreased from approximately 5 GPa with κ~2.4 to 1 GPa. With κ~2.0 as shown in figure 2.16 [120]
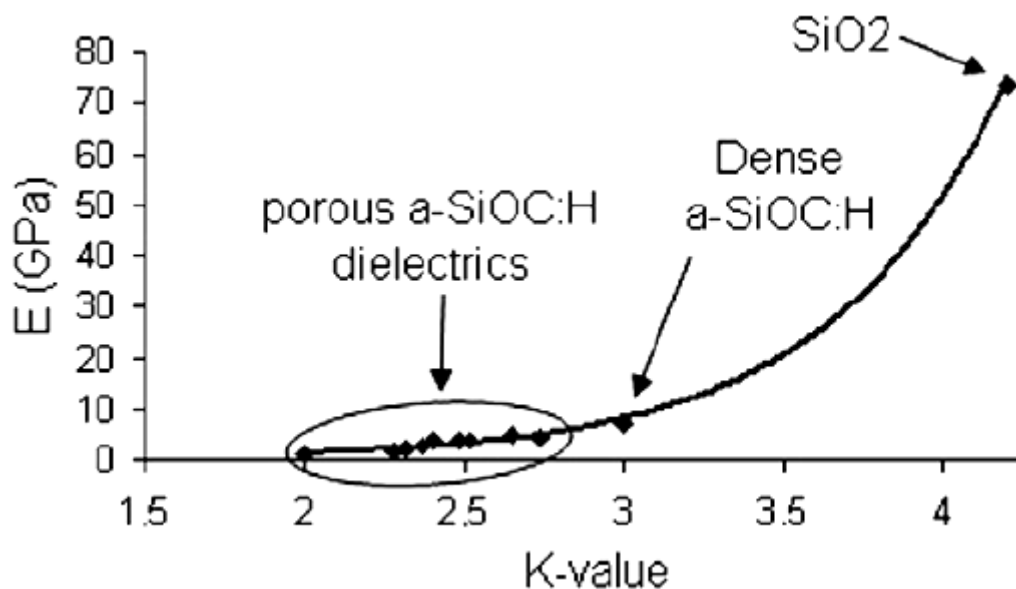
Figure 2.16 Modulus versus k-value for PECVD SiOC:H low-k film.

For a given porogen, increasing the volume fraction from ~10% to ~40% depresses the value of k from 2.7 to 2.0, with a corresponding increase of the pore size. The mechanical improvement with UV-assisted curing was then mainly related to chemical changes in the skeleton. Porous film containing large voids were observed at the porogen loading between 20% and 30%. This transition represents percolation threshold of the cavities when they were becoming fully interconnected.[121] If the porosity is increased to above ~25-30% the pores will percolate (coalesce together to

form interconnected pores). The pore diameter also tends to increase with increasing porosity, and the pore size distribution may increase. Higher porosity, interconnected pores, and a large pore size distribution all degrade mechanical strength. The empirical elastic modulus versus porosity for organo-silicate glass (OSG) relationship could be predicted by percolation theory as shown in Figure 2.17.[122] Increasing the carbon doping further reduces strength by lowering the density of strong Si-O bonds. Dense oxide was a network of tetrahedral Si-O bonding, and introducing Si-CH$_3$ bonds resulted in domains with only two or three Si-O bonds instead of four. Thus the ability to control the film structure at a molecular level would allow the maximum possible mechanical strength at a given κ-value. [123, 124]
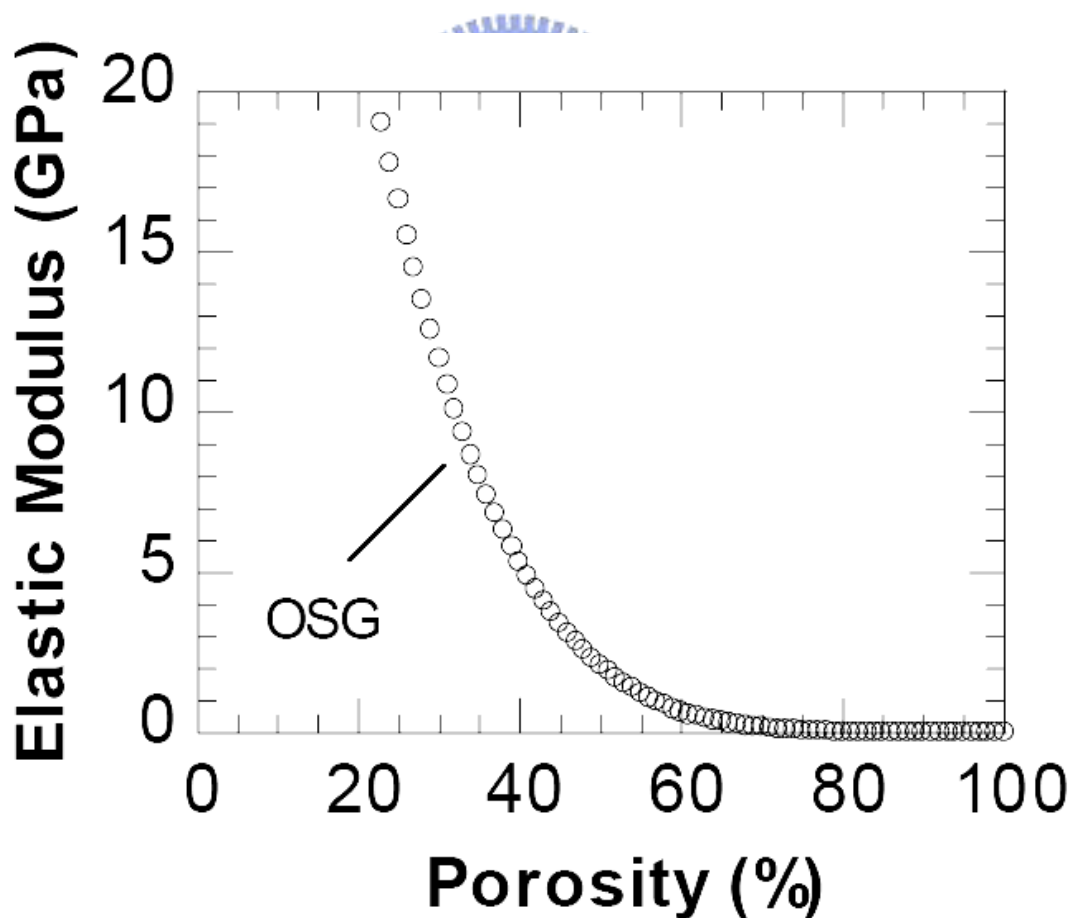
Figure 2.17 Elastic modulus as a function of porosity for organo-silicate glass.

From FEM results, an empirical formula, which describes the relation between density and elastic modulus for porous films as a function of pore aggregation, can be obtained. **As** shown in Figure 2.18, logarithmic values of elastic modulus linearly depend on logarithmic values of density of porous films calculated for ordered pore structure and random pore structure. [125]
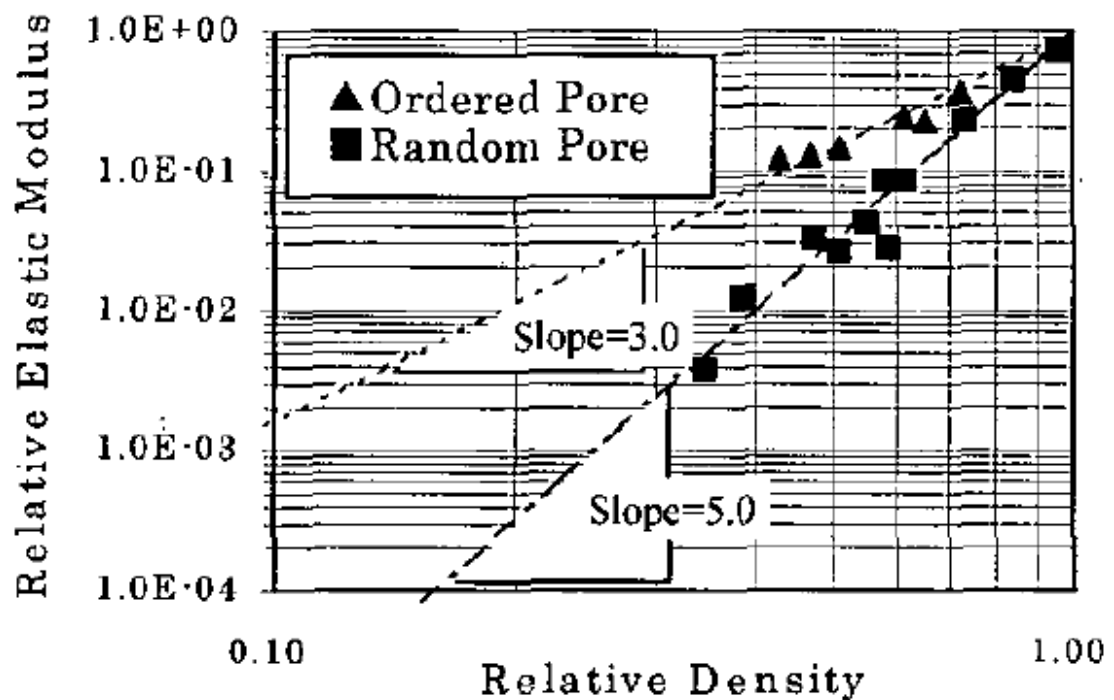
Figure 2.18 Logarithmic plots .of relative elastic modulus and relative density for porous films calculated by FEM.

2.6 Properties requirements and challenges in the implementation of low-k dielectrics in the back-end of line

ILD materials which well known as low-k materials were used in the replacement of conventional SiO_2 in the multilayered microelectronic structure. The application must agree with the processing and packaging conditions. Therefore, several important properties are needed to be focused on, as listed in Table 2.6. The thermal stability must able to withstand the elevate temperature processing of copper metallization that occur at 250°C and usually followed by thermal annealing in the

range of 400°C-450°C to ensure the void free copper deposition. Therefore, during this thermal curing, the thermal mismatch issue between Cu and ILD also cannot be neglected. Coefficient of thermal expansion (CTE) of Cu is 16.5ppm/°C, and SiO_2's CTE is 0.5ppm/°C which is relevant to each other.[126] However, new ILD materials mostly consist of organic dielectric have high CTE in the range of 50ppm/°C which is not prefer in the processing since it might cause thermal mismatch and highly stress that might also cause reliability issue.

Mechanically, the low-k layers must be strong enough to endure the chemical mechanical polishing (CMP) process. The young's modulus, hardness must be high enough to prevent cracking or delamination. The lowest young's modulus which can pass the CMP process is 5GPa and hardness larger than 0.5GPa. [127, 128] The chemical resistance must also agree with the requirement, hydrophobic surface which can result on low moisture absorption.

Another advance in development of low-k materials can be obtained by inherent pores into the system. Since k_{air} =1, thus it is benefit to lower the k-value. The structural problematic is also required. Pores with small size, closed shape, no interconnect geometry are flawlessly needed. Closed nanopores are preferred to prevent any unfavorable metal (copper or other metals) diffuse into the ILD layer during integration process. The nanopores should be as small as possible 5-10 times smaller than the minimum IC metal feature size. Thus the nanopores should be 5-10nm size. [129, 130]

Figure 2.19 shows various integration challenges and issues that will come about accompanied by porous low-k introduce in interconnect. The tremendous number of difficulties emerges when porosity is introduced into the dense low-k matrix. Hence, optimum properties of low-k material are fully demanded to minimize the possibility of problematic issue during integration process. Therefore, low-κ materials need to

overcome the stringent material property requirements for successful integration into interconnects structure.

Table 2.6 Important properties for materials in low-k application

Electrical	Mechanical	Chemical	Thermal	Structural
Low-k	High Young's	Low moisture	High thermal	Small, closed
Low leakage	Modulus	absorption	stability	pore
current	High hardness	No metal	Low CTE	Thickness
Low charge	Low residual	corrosion	Low thermal	uniformity
trapping	stress	Etch	shrinkage	No channel
Low dielectric	High thickness	selectivity	High thermal	continuity
loss	threshold		conductivity	
High	High adhesion			
breakdown	strength			
resistance				
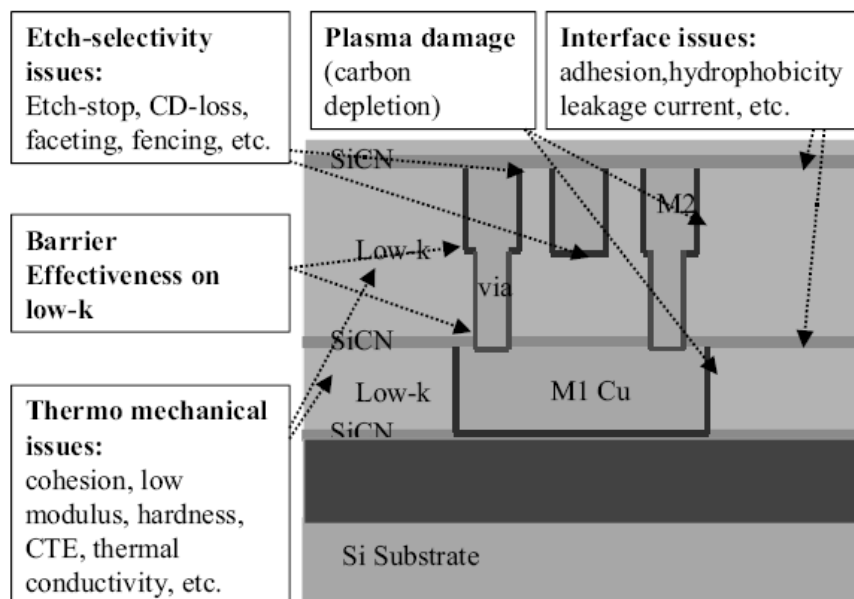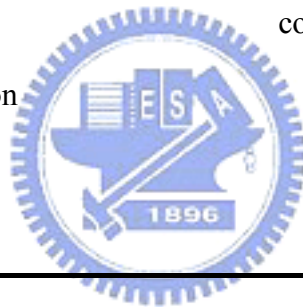
Figure 2.19 Porous low-k integration challenges and issues in the interconnect

Chapter 3 Experimental Section

3.1 Experimental Materials

The experimental raw material solutions were provided by JGC Catalysts and Chemicals Ltd., Japan. Overall, five different kinds spin-on low-k solutions with different chemical compositions designated as NCS1 through NCS5, were summarized in Table 3.1. These low-k solutions were also known as nano-clustering silica (NCS) low-k materials. The specific organosilica chemicals in NCS1 through NCS5 are proprietary information of JGC Catalysts and Chemical Ltd., Japan. The MTMS content was highest in NCS5, whose TPOAH content was the lowest, instead. The chemical structures of TEOS, MTMS, and TPAOH were shown in Figure 3.1 below.

tetraethoxysilane

methyltrimethoxysilane

(a)   (b)

Tetrapropylammonium hydroxide

(c)
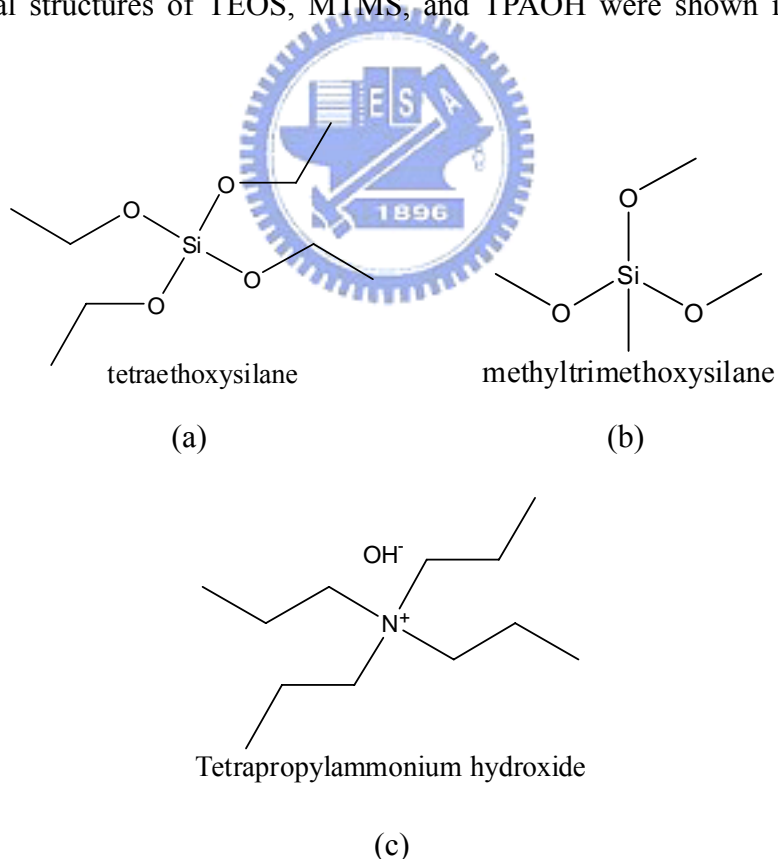
Figure 3.1 The chemical structure of NCS low-k (NCS) precursor (a). tetraethyoxysilane (TEOS) (b). methyltrimethoxysilane (MTMS) (c). tetrapropylammonium hydroxide (TPAOH).

Table 3.1 The compositions of various NCS low-k solutions designated as NCS1 through NCS5

Low-k solution Components	Chemical formula	NCS1	NCS2	NCS3	NCS4	NCS5
TEOS /MTMS, %	$Si(OC_2H_5)_4$ $H_3CSi(OCH_3)_3$	5	8	7	10	12
TPAOH(78 °C), %	Proprietary	7	5	4	5	3

3.2 Sample preparation

The NCS low-k solution was filtered through a 0.45 μm PTFE filter, followed by spin coating onto a (100) silicon wafer using a 2000 rpm rotation speed for 60 seconds. Then, a pre-bake at 150°C for 1 minute using a hot-plate was employed to remove the solvent after spin coating. For multiple coats, the film was immediately cooled down for 3 minutes after 150°C pre-bake. Subsequently, the films either in single coat or multiple coats were further cured in a vacuum furnace under nitrogen purge (low O_2 impurity < 50 ppm) at 250°C for 10 minutes using a ramp rate of 5°C/min, then cured to 400°C for one hour using the same ramping rate. The films were then taken out of furnace after the system was cooled down to room temperature overnight.

For the measurement tool that required the sample in the powder form, the NCS low-k solution was directly underwent the baking processes. The curing recipe was 150°C for 3 hours to ensure the complete removal of solvent, then subsequently heated to 400°C for 1 hour at the same ramping rate as the thin films formation method.

3.3 Experimental procedures and flow chart diagram

The thickness and the refractive index of NCS low-k thin films were analyzed by using n&k Analyzer which was an optically non-destructive measurement tool. In order to understand the chemical bondings in NCS low-k thin films, Fourier transform infrared spectroscopy (FT-IR) was used to verify the chemical makeup and structural information of Si-O of the films. Furthermore, molecular structure was also observed by using ^{29}Si nuclear magnetic resonance (NMR). As well as chemical bonding evidence, molecular structure verification would lead to the early stage of explanation about chemical system identification.

. X-ray reflectivity (XRR) was utilized to characterize the density of NCS films. Porosity was also calculated based on density data. Moreover, the pore geometry parameters such as pore size, pore shape, and pore size distribution were characterized by using grazing incidence small angle X-ray scattering (GISAXS) tools. GISAXS was a prominent tool that could absolutely told the entire information about these parameters effectively.

Mechanical modulus and hardness were measured by using nano-identation (NI) that was by applying load to the diamond tip that suppress into the film. One of the main properties of low-k film was dielectric constant value (κ). This electrical property was measure by employed MIS (metal-insulator-semiconductor) structure or MOS (metal-oxide-semiconductor) method. The surface roughness was determined from atomic force microscope (AFM) tools, which could resolve the particle size that existed on the surface. Thermal stress was measured by using home-build two-laser bending beam method. Thermal was applied through the film on silicon; the deformation of film during heating would determine the thermal stress. Generally, the experimental procedures could be summarized in the flowcharts as shown in Figure 3.2.
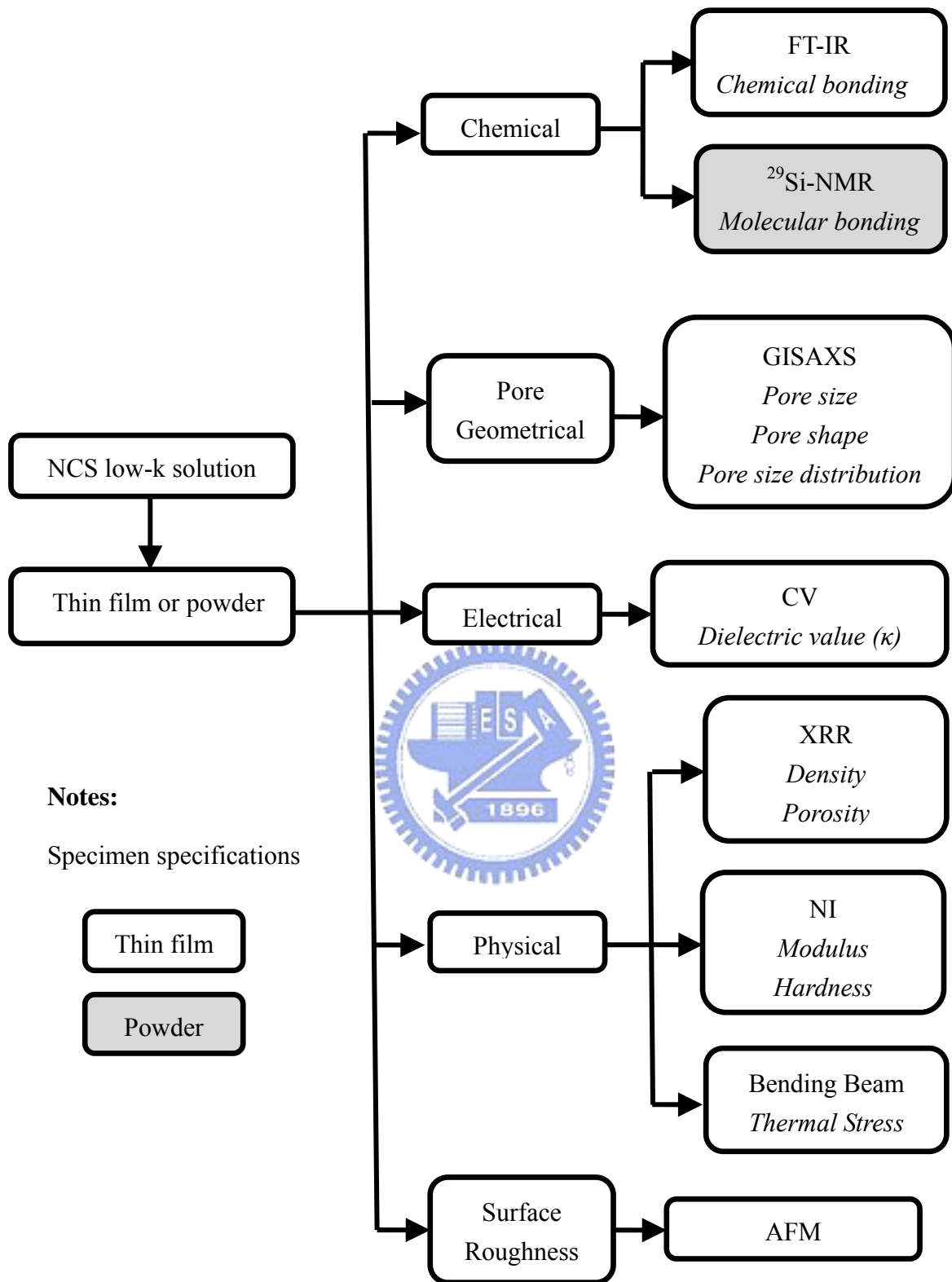
Figure 3.2 Experimental procedure flow-chart diagram

3.4 Characterization Methodologies

3.4.1 Fourier Transform Infrared Spectroscopy (FT-IR)

FTIR is most useful for identifying chemical bonding that is either organic or inorganic. The frequency of the vibrations can be associated with a particular bond type. A Perkir Elmer Spectrum 100 FT-IR was employed in our analysis. Also, transmission mode of low-k films/silicon wafer sample was chosen to characterize the chemical makeup and structural information of Si-O-Si bonding. The spectrum was taken in the wavenumber region of 4000 to 400 cm^{-1} at a resolution of 4cm^{-1} and a total of 32 scans.

3.4.2 Nuclear Magnetic Resonance Spectroscopy (^{29}Si-NMR)

Solid-state Bruker DSX 400WB ^{29}Si NMR (Bruker DSX 400WB) with 9.4 Tesla superconducting magnet was employed to determine the molecular structure of Si-bonding environment. Powder specimen was prepared and spun at rate 6.5 kHz. Chemical shift for ^{29}Si-NMR was reported ranging from -200 ppm to 0 ppm.

3.4.3 X-ray Reflectivity (XRR)

XRR was utilized to measure the density of NCS low-k film. The films were scanned by PANalytical X'Pert Pro (MRD) with Cu Kα source (λ=0.154nm) usingθ-2θ or also called ω-2θ. X-ray reflectivity (XRR) was conveniently applied for the structural studies of both crystalline and amorphous multilayer samples. XRR was an adequate tool to analyze density, thickness, and roughness of thin films. The method involved capturing the intensity of the x-ray beam reflected by a sample at grazing angles. A monochromatic x-ray beam of wavelength λ (usually Cu Kα = 0.154nm) irradiated a sample at a grazing angle ω and the reflected intensity at an angle 2θ was recorded as shown in Figure 3.3. This type of scanning also called ω-2θ

scan. The initial ω angle was set to 0.3°. Theθscanning region started from 0° to 2°.
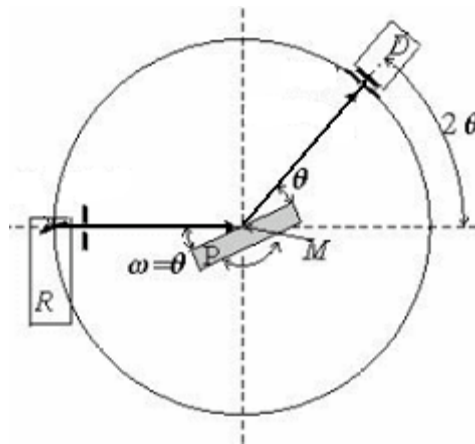
Figure 3.3 Definition of the angle of incidence and reflection in an XRR experiment

The reflection at surface and interfaces was as a result of the distinct electron densities from different layers or films. Due to its different reflective index from different layers, it would emerge different reflection intensity. The complex refractive index of x-ray region was slightly less than 1 and could be expressed by equation 3.1 below. [131]

$$n = 1 - \delta - i\beta \tag{3.1}$$
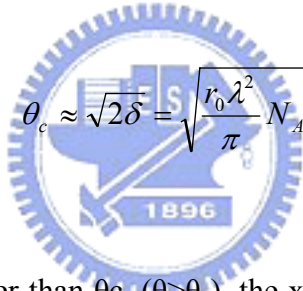
With N_A = 6.022x10^{23} mol^{-1}; r_0, the classical electron radius; λ,the wavelength; Z, the atomic number; A, atomic mass; and ρ, mass density. δand β represented the dispersion and absorption respectively. For the frequency greater than resonance frequency, δcould be further expressed by equation 3.2

$$\delta = \frac{e^2 n_e}{2\varepsilon_0 m (2\pi c)^2} \lambda^2 = \frac{r_0 \lambda^2}{2\pi} . n_e \tag{3.2}$$

Where r_0 was the Bohr atomic radius and n_e was the electron density. Electron density n_e was the number of electron per atom (Z) multiplied by number of atom (n_{atom}). Z was usually replaced by complex atom form factor $f=f_0+f'+if''=Z+f'+if''$. Furthermore, n_{atom} was related to the density of material (ρ) by equation 3.3

$$n_{atom} = \frac{N_A}{A}\rho \qquad (3.3)$$

With N_A and A were the Avogadro number and the atomic weight respectively. For incident angles below a critical angle, θ_c, ($\theta<\theta_c$), total reflection occurs. The θ_c could be finally reduced to relate with ρ by equation 3.4

$$\theta_c \approx \sqrt{2\delta} = \sqrt{\frac{r_0\lambda^2}{\pi}N_A\frac{(Z+f')}{A}.\rho} \qquad (3.4)$$

For incident angles greater than θ_c, ($\theta>\theta_c$), the x-ray beam penetrated inside the film. Therefore, reflection occurred at the top and bottom surfaces of the film. Interference between the rays reflected from the top and the bottom of the film surface would generate interference fringes which related to the thickness of film (d) by equation 3.5

$$d \approx \frac{\lambda}{2}\frac{1}{\theta_{m+1}-\theta_m} \quad \text{for } \theta_m>>\theta_c \qquad (3.5)$$

The other important quantity from XRR measurement was surface roughness. Roughness would tend to diffuse scattering the reflected beam, causing drop of the intensity of reflected beam. For a rough surface, increasing the angle would decrease

the intensity even stronger than the smooth surface that could be stated as equation 3.6 for smooth surface and equation 3.7 for rough surface. σ described the root mean square roughness. θ_i was the angle of incidence and K equal to $2\pi/\lambda$.

$$R_F \propto \frac{\delta^2}{4\theta_i^{\,4}} \tag{3.6}$$

$$R \propto R_F \exp(-(2K\theta_i)^2 \sigma^2) \tag{3.7}$$

3.4.4 Grazing Incidence Small Angle Scattering X-ray (GISAXS)

Grazing-Incidence Small-Angle X-ray Scattering (GISAXS) was a versatile tool for characterizing nanoscale density correlations and/or the shape of nanoscopic objects at surfaces, at buried interfaces, or in thin films. GISAXS combines features from Small-Angle X-ray Scattering (the mesoscopic length scale, incident beam definition by multiple slits, area detector) and diffuse X-ray Reflectivity (the scattering geometry and sample goniometer). In order to make x-ray scattering surface sensitive, a grazing incidence angle a is chosen between about half the critical angle α_c and several critical angles of the film material GISAXS measurements were performed at the BL23A beam-line of the National Synchrotron Radiation Research Center (NSRRC). The incidence beam, extracted from a super-conducting wavelength-shifter (SWLC) X-ray source, was monochromated to a wavelength λ of 1.55°A by a Ge(111) double crystal monochromator, with $\Delta\lambda/\lambda \sim 10^{-3}$. The two dimensional image were recorded by a low-noise 16-bit charge-coupled device (CCD) camera. All the GISAXS data were corrected for sample transmission, background, and the detector sensitivity.   The typical geometry of GISAXS measurement was

depicted in Figure 3.4. The area detector records the scattering intensity of scattered rays over a range of exit angles β and scattering angles φ in the surface plane. [132]
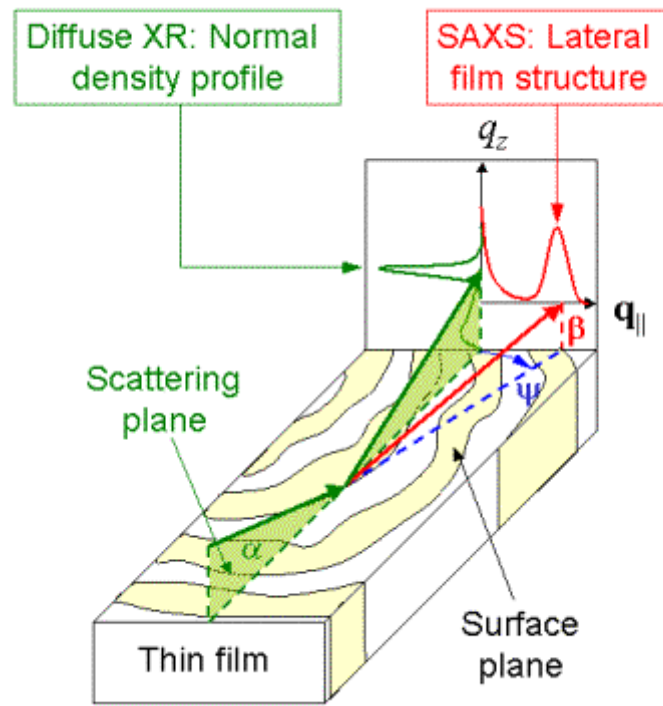
Figure 3.4 Typical geometry of GISAXS measurement.

3.4.5 Capacitance-Voltage measurement (C-V measurement)

A MIS (Metal-Insulator-Semiconductor) configuration, i.e. Al/low-k film/silicon wafer, as illustrated in Figure 3.5 was employed in our capacitance measurement. The silicon substrate has (100) orientation and resistivity 10~100Ω.cm (p-type). Then low-k materials with a nominal thickness of 3000 **Å** were prepared according to the procedure described in previous section. The Al dots were deposited by thermal evaporation of 5000 A thick Al through a contact mask with three different dot sizes (400 μm, 800 μm, and 1000 μm) as illustrated by Figure 3.6. Subsequently, capacitance values of various dots were measured in a vacuum chamber by Helwett

Packard 4280A using CV mode. The capacitor MOS was biased with ±20V at room temperature. The dielectric constant value was obtained from the linear fitting of capacitance versus area. Such method can eliminate the fringes effect of CV dots from edges and error from inaccuracy of area size measurement.
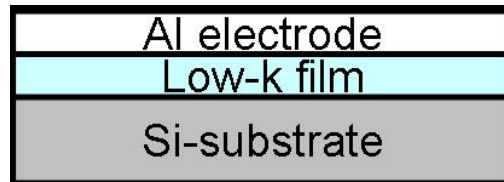
Figure 3.5 Film stack of MIS structure for CV measurement
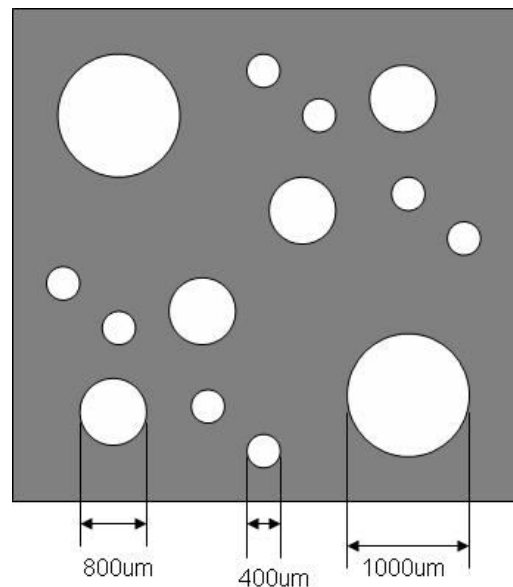
Figure 3.6 Top-view of Al-mask with 3 different dot sizes

3.4.6 Nano-Indenter (N-I)

Mechanical properties of low-k films were characterized by using nano-identer. Specifically, Nano Identer XP system (MTS Corp.) with a diamond tip of Berkovich geometry was utilized to measure the hardness and elastic modulus of low-k film. Load as large as 0.5~20mN was applied to the films by diamond tip constantly. Before the tip was unloaded with constant rate, the system was introduced to holding

section after each loaded section for system equilibrate. As the load is increased, the indenter sinks into the material due to both elastic and plastic deformation. If the load is held constant, the indenter continues to sink into the material due to time-dependent deformation (creep). When the indenter is unloaded, the material recovers by a process that is primarily elastic as shown in Figure 3.7.
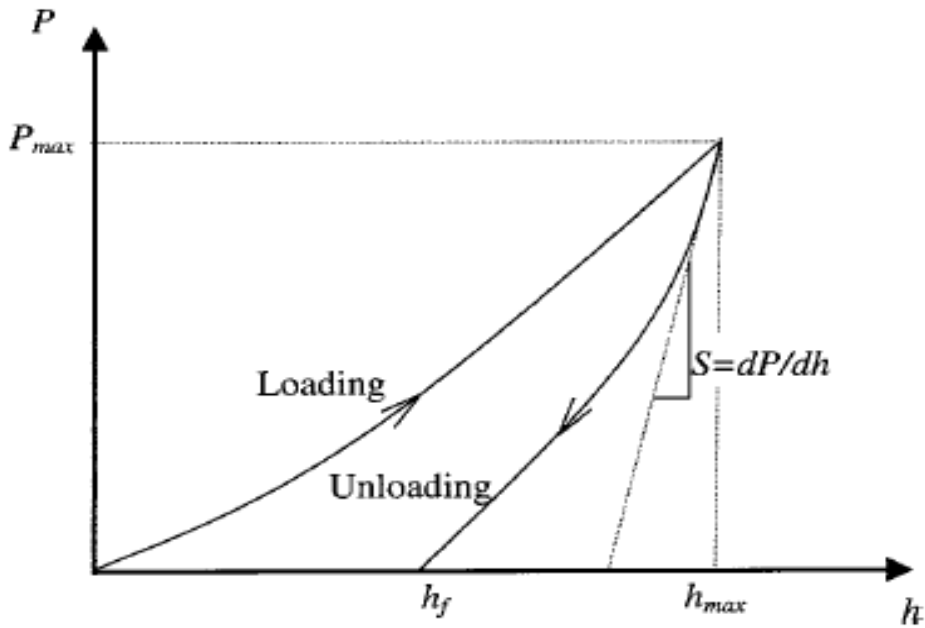
Figure 3. 7 Schematic plot of a typical load-displacement curve

The indentation depth of measurement was about one tenth of film thickness. In case of reduction of substrate effect and other inaccuracy, only 10% initial thickness of a film was used to determine the hardness and elastic modulus of low-k film. Since early slope of the unloaded curve(S) can be interpreted as: [133]

$$S = \frac{dP}{dh} = \frac{2\beta}{\sqrt{\pi}} E_r \sqrt{A}$$

(3.8)

The unloading stiffness S was measured from the experiment. E_r was the reduced

modulus and A was the projected area of elastic contact. Furthermore, the reduced modulus was defined by

$$\frac{1}{E_r} = \frac{(1-v^2)}{E} + \frac{(1-v_i^2)}{E_i}$$

(3.9)

Where E and E_i were Young's modulus of thin film and indenter. v and v_i were both Poisson's ratio for thin film and indenter, respectively. Thus the modulus could be determined above-mentioned method. In addition, the hardness could easily be interpreted by

$$H = \frac{P_m}{A}$$

(3.10)

Where P_m: maximum load and

A: contact area.

3.4.7 Bending Beam measurement

A bending beam method has been developed in our laboratory to measure the stress and coefficient of thermal expansion (CTE) of low-k films. A homemade bending beam system as shown in Figure 3.8 can handle one cantilever beam (or samples) in a vacuum chamber with temperature up to 400°C. Thin film stress measurement was based on the change of curvature radius of low-k film as a function of temperature for a specific substrate, such as silicon wafer. The stress of low-k films on a substrate can be obtained from the change in the radius of curvature based on Stoney's equation: [134]

$$\sigma = \frac{E_s t_s^2}{6(1-v_s)t_f}(\frac{1}{R} - \frac{1}{R_0})$$

(3.11)

where R_0 was the radius of curvature of the bare substrate and R was the radius of curvature after film being deposited. E_s and v_s were both substrate's Young's

modulus and Poisson ratio, respectively, and t_s and t_f were substrate and film thicknesses, respectively.
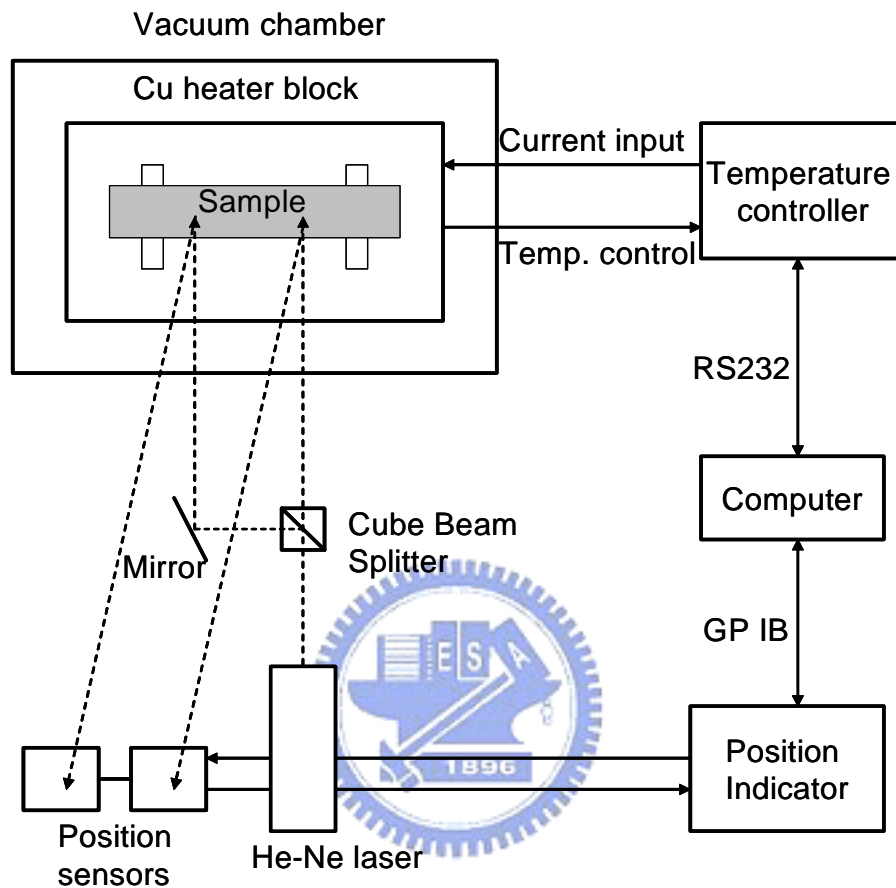
Figure 3. 8 Schematic diagram of our home-built bending beam system

3.4.8 Atomic Force Microscope (AFM)

AFM (Veeco D5000) was employed to quantify the surface roughness of NCS low-k film. In the operation mode, the cantilever was biased with AC and DC voltages and sensed the distance between the tip and the sample surface by Van der Waal's force. As the interaction force changed between the cantilever tip and the surface, the deflections of the cantilever were varied. Finally, the deflections were measured and derived a topographic image of the surface.

Chapter 4 Results and Discussion

4.1 Overview

The organization of the results and discussion chapter was classified into structure characterization and property analysis.

The structure characterization was started by the investigation of silica precursor loading (TEOS/MTMS) impact on chemical and molecular bonding such as Si-O-Si crosslink degree. Moreover, the effect of TPAOH loading on density and porosity of NCS low-k films was also being analyzed. The discussion was followed by the correlation of porosity and Si-O-Si matrix cross-link impact on film structure. On the next section pore morphology such as pore size, shape and pore size distribution were also accommodated. After a summary on the structure characterization, the models for the pore formation and pore collapse mechanism were proposed.

On the next section, property of NCS porous low-k such as electrical, mechanical, thermo-mechanical and surface roughness were analyzed. The discussion would cover the impact of Si-O-Si matrix cross-link, porosity and pore shape on dielectric constant and modulus, the impact of porosity on thermal stress range. Finally, the discussion about the root causes of modulus degradation was also being articulated. Last but not least, the surface roughness of NCS porous low-k was compared to pure silica-zeolite low-k film.

4.2 Structure characterization

4.2.1 The impact of silica precursor loading (TEOS/MTMS) on chemical bonding

The Fourier-transform infrared spectra of various NCS low-k films (from NCS1 to NCS5) were performed in the range from 400 cm^{-1} to 4000 cm^{-1}. The major absorption peaks were found in the region of 950 cm^{-1} to 1350 cm^{-1} as depicted in Figure 4.1. The important absorption peaks were the methyl (CH_3) group at 1274 cm^{-1}, the Si-O-Si with angle around 140° (network like structure) peak at 1046 cm^{-1}, Si-O-Si with angle around 150° (cage like structure) peak at 1130 cm^{-1}, and the Si-O-Si (sub-oxide like) with angle less than 140° peak at 1020 cm^{-1}. In contrast, peaks between 950 cm^{-1} and 700 cm^{-1} were mainly linked to Si-C bonds. [135] Major FT-IR peaks and their assignments were summarized in Table 4.1

Table 4.1 Peak position and assignment for each chemical bonding between 700 and 1300 cm^{-1} (υ-stretching, δ-bending)

Peak position, cm^{-1}	Chemical Bonding assignment
1274	δ-methyl (C-H_3)
1046	υ-Si-O-Si (network)
1130	υ-Si-O-Si (cage)
950-700	υ-Si-C
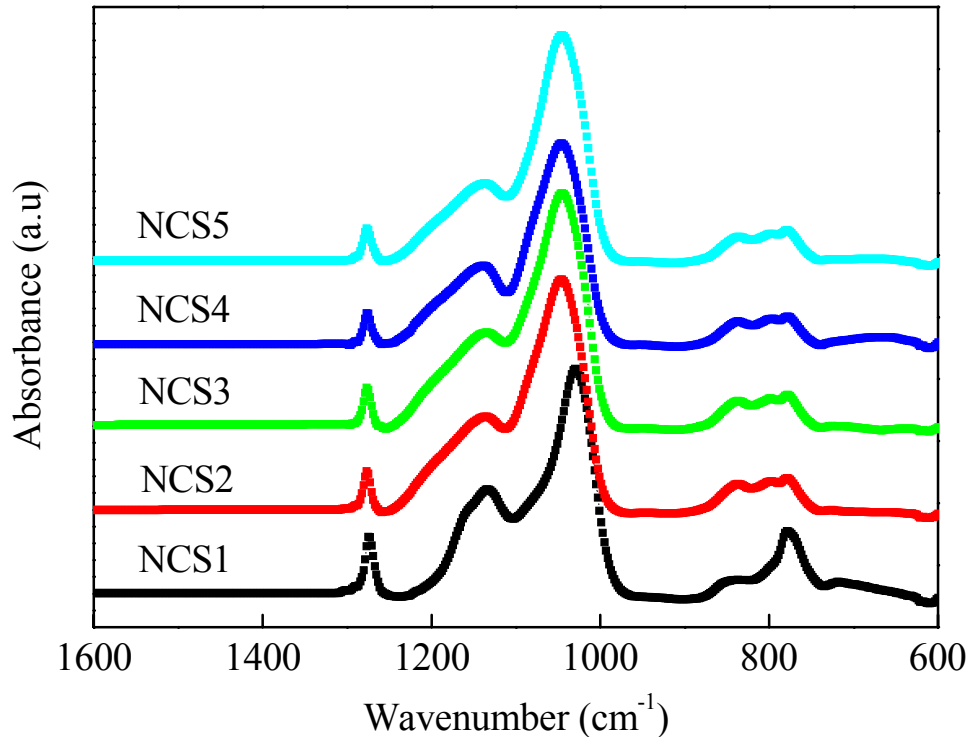
Figure 4.1 Transmission FT-IR spectra of NCS low-k films (NCS1 to NCS5) cured to 400°C in the range 700 cm^{-1}-1500 cm^{-1}

Figure 4.2 showed that the Si-O-Si network structure at 1046 cm^{-1} increased its intensity from NCS1 to NCS5, inferring that the higher degree of cross-linking in Si-O-Si matrix was achieved in NCS5. In addition, peak shift (blue shift) from 1028 cm^{-1} to 1046 cm^{-1} was clearly observed from NCS1 to NCS5, indicating that the microstructure of NCS low-k materials became denser structure because of its higher bond energies. Such denser structure was formed due to a higher cross-linking of Si-O-Si linkage. Thus, the higher cross-linking of Si-O-Si matrix and denser structure were believed to induce by more TEOS instead of MTMS. Therefore, higher cross-link matrix could be obtained through the incorporation of more TEOS in place of MTMS. In short, dense oxide consisted of a network of tetrahedral Si-O bonding obtained through the hydrolysis of TEOS monomer. In contrast, introducing Si-CH$_3$ bonds in MTMS resulted in matrix formation with only three Si-O bonds and less crosslinking.

Other distinguished peaks were also observed. Si-C peaks between 750 and 850 cm^{-1} has three hidden small peaks that were observed for NCS2 through NCS5, except for NCS1 which has the strongest absorption peak of Si-C at lower wavenumber region. NCS1's methyl groups CH$_3$ absorption peak at 1277cm^{-1} also revealed stronger absorption intensity than others NCS low-k films. In contrast, for NCS2 to NCS5 low-k films, almost similar absorbance intensity for methyl groups was observed. This referred that the more methyl groups through MTMS precursor was incorporated in NCS1 porous low-k film. A less crosslinked Si-O-Si matrix in NCS1 was found due to the incorporation of more MTMS groups which consisted of a terminal methyl group. The incorporation of methyl group via MTMS would impart a benefit in reducing the k-value since reduced the polarizability of Si-CH$_3$ compared to Si-O bond that it has replaced [136], which will be discussed further in Section 4.6.2.
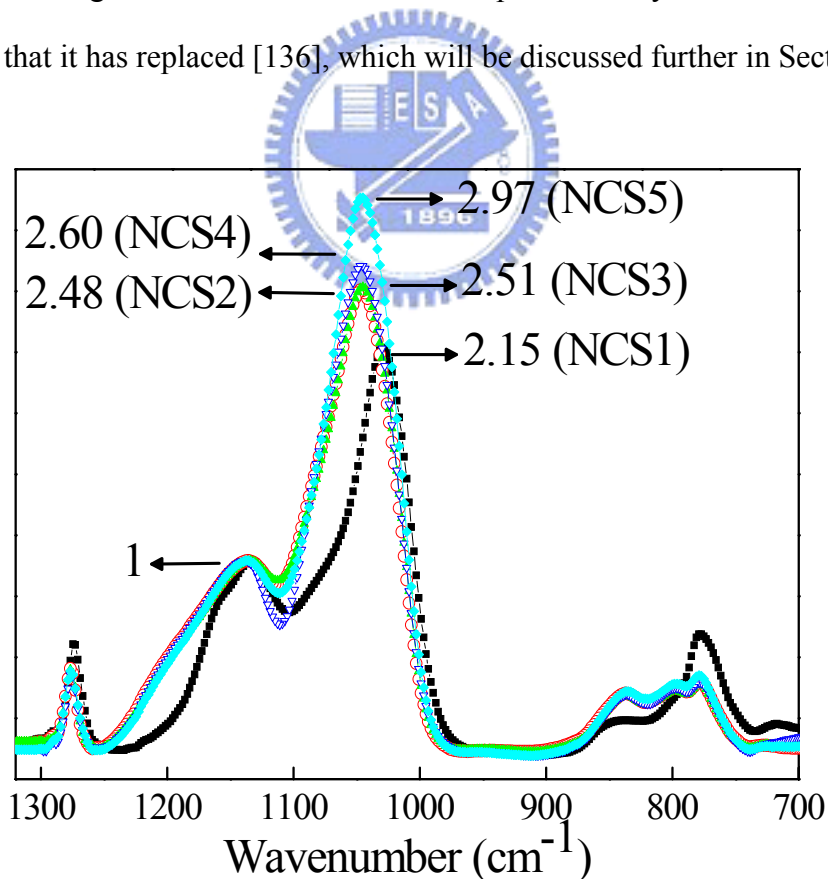
Figure 4.2 NCS low-k films Si-O-Si network ratio increased from NCS1 through NCS5

4.2.2 The impact of silica precursor loading (TEOS/MTMS) on molecular

   bonding

In order to articulate the molecular bonding of NCS low-k films, ^{29}Si NMR spectra of NCS1-5 were obtained by using powder samples. Table 4.2 listed the possible peak positions and their structural assignment for ^{29}Si NMR spectra. The nomenclature "Q4" denoted Si bonded to four O, and "T" referred to Si bonded to three O and one CH_3 groups, while "Q3" [$(SiO)_3Si(OH)$] denoted the bonding of Si to three O and one OH group, in addition to "D" for [$(SiO)_2Si(CH_3)_2$] and "M" for [$(SiO)Si(CH_3)_3$]. [137]

Table 4.2 Nomenclature, peak assignments and peak positions of ^{29}Si-NMR spectra

	Assignment	Position (ppm)
Q4	[$(SiO)_4Si$]	-119.1
Q3	[$(SiO)_3Si(OH)$]	-102.1
	[$(SiO)_3Si(OMe)$]	
T3	[$(SiO)_3Si(CH_3)$]	-64.5
T2	[$(SiO)_2Si(OH)(CH_3)$]	-56.3
	[$(SiO)_2Si(OCH_3)(CH_3)$]	
D2	[$(SiO)_2Si(CH_3)_2$]	-17.8
M1	[$(SiO)Si(CH_3)_3$]	9.2

Figure 4.3 showed ^{29}Si NMR spectra of NCS low-k materials from NCS1 to NCS5. NCS2 through NCS5 possessed predominantly a fully cross-linked structure with a sharp intensity of Q4 [$(SiO)_4Si$] group centered around -110ppm, in addition to T3 [$(SiO)_3Si(CH_3)$] group centered at -66 ppm. In contrast, NCS1 was predominantly consisted of T3 [$(SiO)_3Si(CH_3)$] group, but with very liitle Q4 group. Since T group

was comparably less cross-link compared to Q group, ^{29}Si-NMR offered strong molecular structures evidence to interpret the structure-property relation among the NCS low-k materials. Subsequently, the amount of Q and T groups were quantified using the peak integration and summarized in Table 4.3 by defining Q-group as one. NCS1 revealed the largest T-group available which was 4 times greater than Q-group. On the other side, NCS2 through NCS5 contained both T- and Q-groups, whose ratios ranged from 0.68 to 0.92.
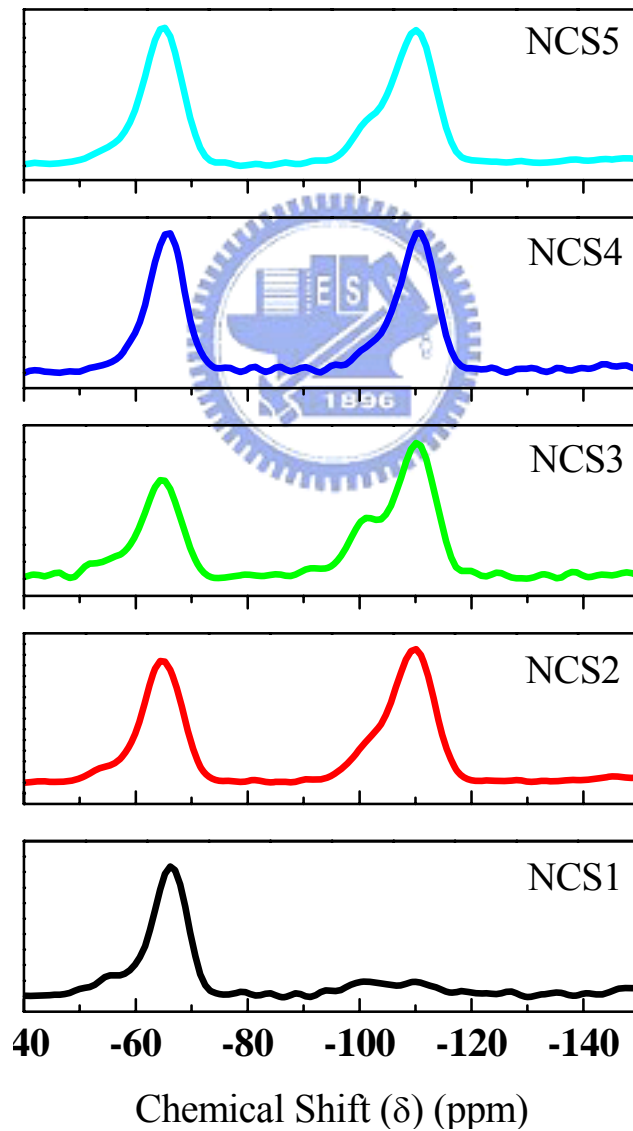
Figure 4.3 ^{29}Si solid-state NMR spectra of NCS1 to NCS5 samples.

Table 4.3 Peak area of Q and T structures for NSC1 through NCS5

Molecular	NCS low-k				
Structure	NCS1	NCS2	NCS3	NCS4	NCS5
Q[(SiO)$_4$Si]	1	1	1	1	1
T[(SiO)$_3$Si(CH$_3$)]	4	0.92	0.86	0.8	0.68

Basically, the formation of Q group or T group could be explained through Figure 4.4 below that depicted the monomer of MTMS and TEOS. MTMS has 3 active functional groups (-OR) and TEOS has 4 active functional groups. Therefore, the reaction that added more MTMS would result in higher T [(SiO)$_3$Si(CH$_3$)] groups and reaction with more addition of TEOS would possess higher Q [(SiO)$_4$Si] groups. Thus, for NCS2 to NCS5, the percentage of MTMS to TEOS was balanced to obtain the highest crosslink structure, while maintain enough T3 structure to reduce the dielectric constant.

In the meantime NCS1, the percentage of MTMS was believed to be extremely higher than TEOS, which generated a structure with very high content (~4x) of T3 groups relative to Q-group.

(a)   (b)
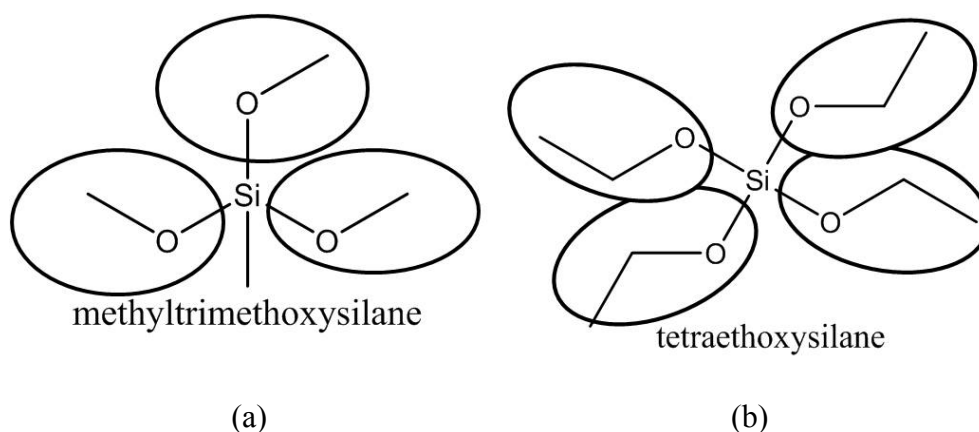
Figure 4.4 The active functional groups in (a) MTMS and (b) TEOS

Summarizing the effect of TEOS/MTMS ratio on chemical and molecular bonding, FT-IR and ^{29}Si-NMR results revealed NCS1 porous low-k chemical bonding and structure was comparatively weaker and looser than others NCS low-k. The evidences were listed as NCS1's Si-O-Si lower wavenumber (lower bond energy), higher content of Si-CH$_3$ lower polarizability bonding, and the lack of high cross-link Q-group, in the present of more T-group. The primary cause was extremely high MTMS precursor incorporated to the matrix instead of TEOS as a silica precursor.

4.2.3 The impact of TPAOH and TEOS/MTMS loading on density and porosity

X-ray reflectivity spectra of NCS1 through NCS5 low-k were shown in Figure 4.5. When the scanning proceeded at very low angle, a total reflection occurred. The initial sudden drop corresponded to a penetration of X-ray into NCS film. The angle of first sudden drop occurred was called critical angle (θ_{crit} 1). The second critical angle (θ_{crit} 2) was the characteristic of the denser silicon substrate. This first critical angle (θ_{crit} 1) was accurately related to the electron density of the film, which could be related to the bulk density of the film. Therefore, the θ_{crit} 1 was related to the density of porous NCS film illustrated by Equation 4.2

$$\theta_{crit} = \left(2\delta\right)^{1/2}$$

(4.2)

where δ was the density of porous NCS film. If the density of porous NCS film was precisely known, the film's porosity could be calculated based on Equation 4.3. [138]

$$\rho = \rho_s.\left(1 - \varphi\right)$$

(4.3)

where ρ was film density (g/cm^3), ρ_s was silica density (1.63 g/cm^3), and φ referred to porosity. Generally if the density of porous NCS films increased, the porosity reduced. Table 4.4 summarized the density and porosity of NCS low-k films by using XRR. NCS1 low-k film has the highest porosity that was 10% higher compared to NCS2 low-k film. The loading of TPAOH, a porogen increased from NCS5 to NCS1, thus porosity increased from NCS5 to NCS1. In addition to the TPAOH loading factor, more incorporated methyl groups in NCS films by lower TEOS/MTMS also rendered loose structure with more space because Si-CH$_3$ terminal group provided more steric hindrance as compared to Si-O-Si network linkage. As a result, more TPAOH loading or higher Si-CH$_3$ bonding could induce lower density or higher porosity to NCS porous low-k films.
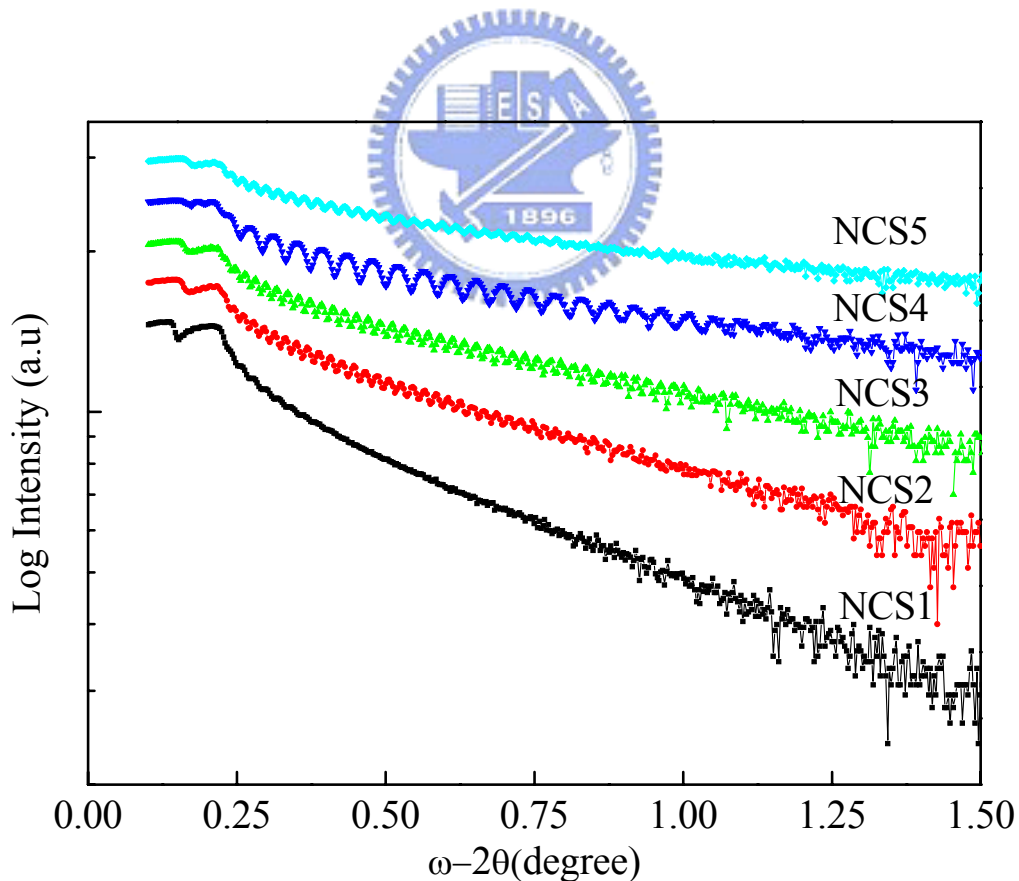
Figure 4.5 X-ray reflectivity patterns of NCS1 to NCS5 samples

Table 4.4 Density and porosity of NCS low-k films by using XRR

NCS low-k film	Density (gr/cm^3)	Porosity (%)
NCS1	1.000	38.6
NCS2	1.185	27.6
NCS3	1.194	26.9
NCS4	1.280	20.5
NCS5	1.325	18.7

4.2.4 The effect of chemical bonding/structure and porosity on film structure

Based on ^{29}Si NMR result in the section 4.1.2, NCS low-k film molecular bonding had already been validated. NCS1 low-k demonstrated the least cross-linked behavior compared to NCS2 through NCS5 low-k as a result of its smallest quantity of Q [(SiO)$_4$Si] group, which was the key component of a fully cross-linked structure. In the other perception, NCS1 owned numerous T [(SiO)$_3$Si(CH$_3$)] groups which could lowered the dielectric constant through –CH$_3$ less polarizability bond. Porosity also showed the largest for NCS1 low-k (ρ=38.6%) compared to others NCS low-k films ($\rho \leq$27%).

NCS2 to NCS5 low-k revealed higher crosslink matrix that was proved through the relevant quantity of Q and T groups in the matrix, lower porosity (ρ<27%) was also observed for NCS2 to NCS5 low-k films.

For more understanding the effect of cross-linking of Si-O-Si matrix and porosity on the film thermal shrinkage property, change of film thickness were measured before and after thermal curing processes. The chosen temperatures were pre-cured temperature of 150°C which was the temperature of solvent evaporation and 400°C that was the polymerization temperature. As graph in Figure 4.6, it was clearly observed that NCS1 soft bake cured (150°C) film has thickness which was

40% thicker than final high temperature cured sample (400°C). In the meantime, NCS2 through NCS5 NCS low-k films soft bake cured sample only differ with high temperature cured sample 5-8 % in thickness. This drastic shrinkage of thickness was due to its less cross-linked structure and higher porosity which caused the matrix to collapse and form more stable structure. This led us to closely examine the pore size its distribution, and pore morphology in various NCS porous low-k films, especially the effects of TEOS/MTMS ratios and TPAOH loadings in the subsequent sections.
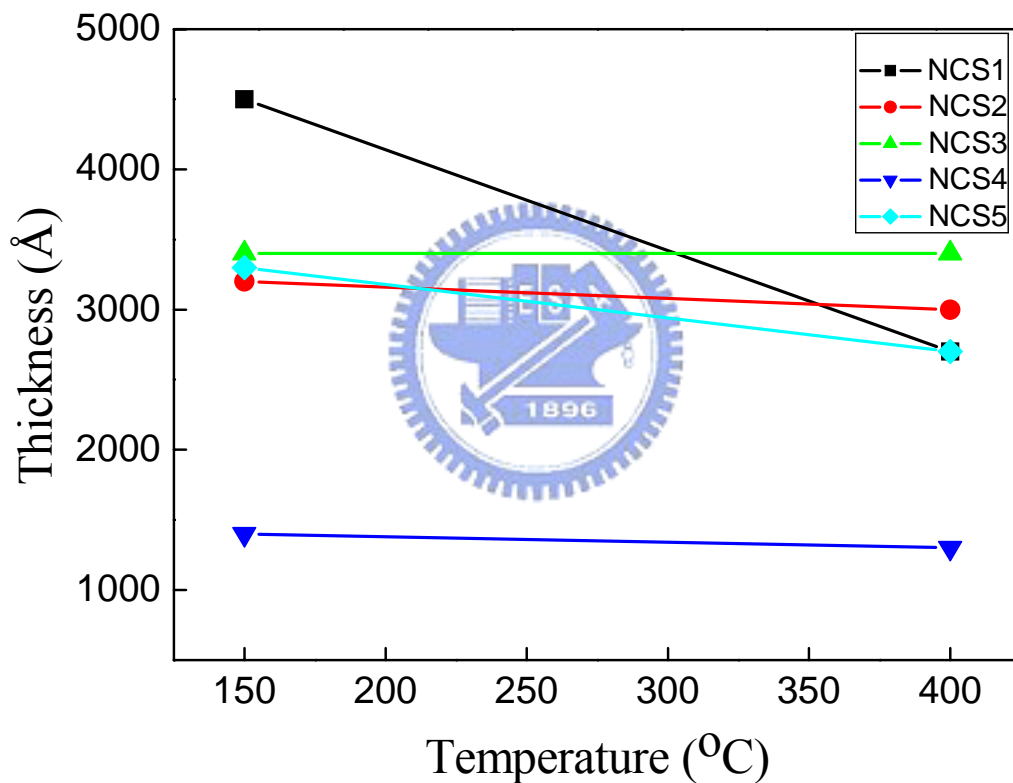
Figure 4.6 Thickness shrinkage during thermal curing process from 150°C to 400°C for NCS1 through NCS5 NCS low-k thin films.

4.3 Pore morphology and pore size/distribution characterization

The pores that formed in NCS low-k films were examined by grazing incidence small angle X-ray scattering (GISAXS). Since it was well-known that zeolite-type low-k films (NCS low-k film) consisted of micropores (<2nm) and mesopores (<20nm). [104,105] Therefore, it was challenging to cultivate such small pores. Grazing-incidence small-angle X-ray scattering (GISAXS) was also one of a non-destructive modern technique of choice since it could overall precisely determine pore shape, pore sizes and pore size distribution. [139, 140]

4.3.1 GISAXS Theorem

From the theorem of GISAXS, it was defined that the intensity of scattering pattern was proportional to the product of intra-particle structure factor (form factor), P(q) and inter-particle structure factor S(q) (structure factor): [141]

$$I(q) = P(q)S(q) \tag{4.4}$$

where q was the scattering wave vector. The scattering wave vector, q, was defined by

$$q = \frac{4\pi}{\lambda} \sin \theta \tag{4.5}$$

where θ and λ were the scattering angle and wavelength of radiation employed. The scattering intensity distribution for a polydisperse system was proportional to the ensemble average of the intra-particle structure factor (assuming no inter-particle interactions) (S(Q)=1) as given by

$$I(q) = \int_0^\infty I_0 P(q,x) f(x) dx \tag{4.6}$$

where f(x) was a normalized distribution function for size parameter, x. Size distribution function used to describe polydispersity in particle interaction (pore interaction) was the Schultz distribution. The general formula for a Schultz distribution was given by: [142]

$$fs(x) = \frac{x^z}{\Gamma(z+1)} \left[\frac{z+1}{x_{avg}} \right]^{z+1} \exp\left(-\frac{(z+1)x}{x_{avg}} \right) \tag{4.7}$$

that $\Gamma(n)$ was the gamma function and z was the polydispersity (σ) parameter defined by

$$z = \left(\frac{x_{avg}}{\sigma} \right)^2 - 1 \tag{4.8}$$

Since the form factor P(q) has been evaluated for a variety of particle shapes (spheres, rods, discs *etc.*). However, in the range of very low *q* (qxy<1). all particle shape and size could be generalized by using Guinier approximation: [143]

$$I(q) = P(q) = \exp\left(\frac{-q^2 R_g^{\,2}}{3}\right) \qquad (4.9)$$

where R_G defined as the root mean squared distance of all atoms from the center of mass of the particle that was the measure of average size of the particles R, basically referred to the average size of pores. Hence by plotting ln I(q) vs. q2, the radius of gyration could be calculated from the slope. Thus radius of gyration based on guinier approximation was

$$Slope = -\frac{1}{3} R_g^{\,2} \qquad (4.10)$$

Instead of spherical shape particle, rod-like or disk-like shape particle could be approximated by using Kratky-Porod approximation as: [144]

$$I(q) = P(q) = \frac{1}{q} \exp\left(-\frac{q^2 R_c^{\,2}}{2}\right) \qquad (4.12)$$

where Rc was the the radius of cylinder. By plotting ln I(q).q versus q^2, the radius could be estimated by

$$Slope = -\frac{1}{2} R_c^{\,2} \qquad (4.13)$$

4.3.2 Pore size and pore shape analysis by Kratky-Porod and Guinier

   Approximation

Figure 4.7 displayed GISAXS scattering patterns for NCS low-k films. For NCS1 low-k film, isotropic with well defined ring of maxima scattering pattern was observed. It represented that the existence of narrow pore size distribution and a well organized pattern of pores. The distribution of pore was assumed to be well randomly distributed. No pore-to-pore correlation could be extrapolated from NCS1 low-k film. However, NCS2 low-k film showed the same scattering pattern with anisotropy distribution. A slight anisotropy appeared for NCS2 through NCS5 low-k films. In addition, pore-to-pore correlation was observed.

In order to develop more profound structural information from the scattering patterns, initial approximation was defined by using Guinier plot (ln I(q) versus q_{xy}^2) for spherical pore shape or Kratky-Porod plot (ln I(q).Q versus q_{xy}^2) for elliptic cylindrical pore shape. Figure 4.8 illustrated the ln I(q).Q versus q_{xy}^2 of NCS1 porous low-k film for both in plane and out of plane direction. In-plane direction was referred to x-y plane direction (parallel to the substrate) and out-of-plane referred to z-direction (perpendicular to the substrate). Thus, based on Equation 4.13, the slope was directly related to the radius(R) of pores in either in-plane or out-of-plane direction.
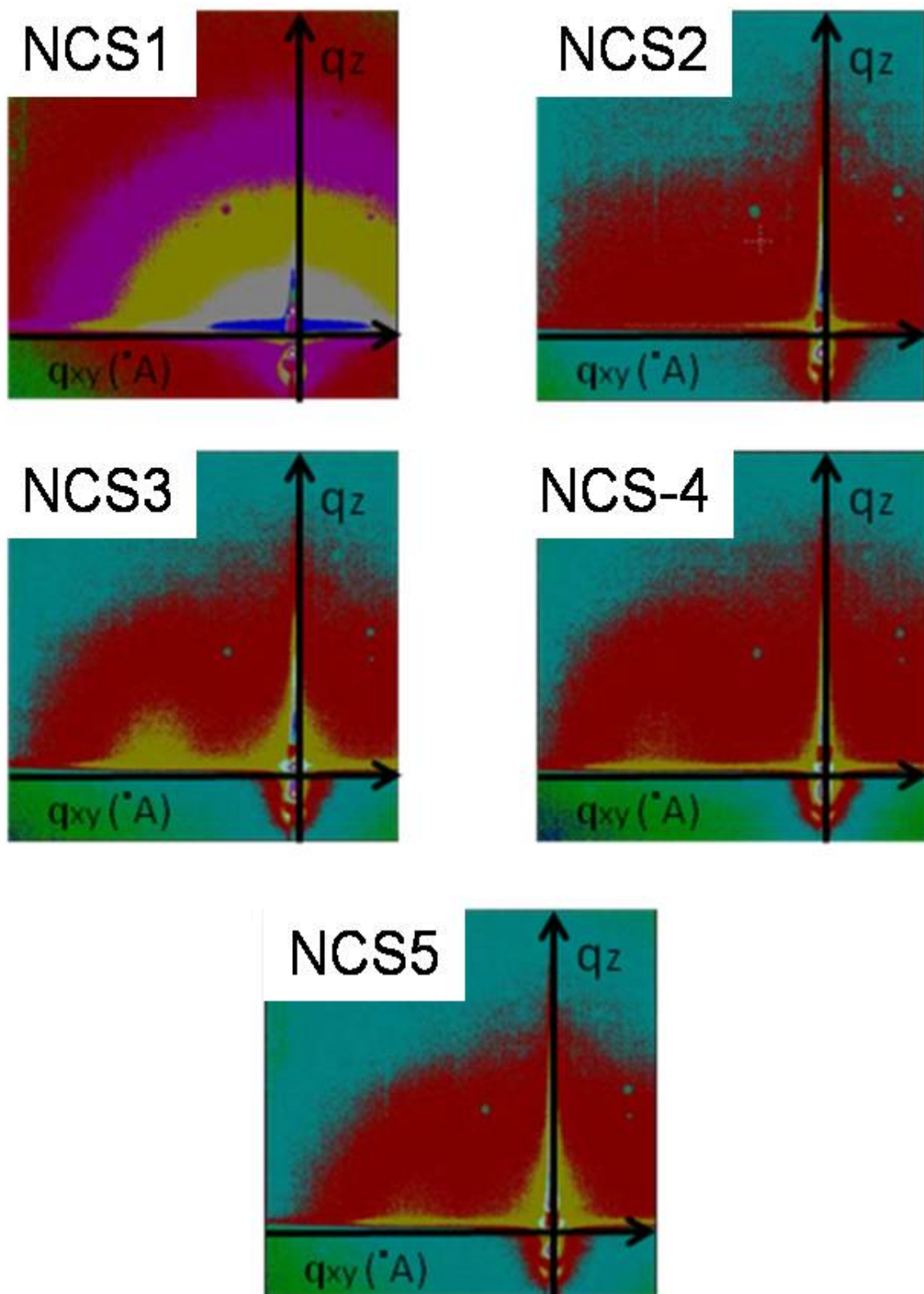
Figure 4.7 GISAXS scattering patterns of NCS low-k films

Therefore, from the outset slope observation, first radius determination could be approached. NCS1 showed significant different slope either from in-plane or out-of-plane scattering intensity, thus definitely NCS1 has different pore radius dimension either in-plane or out-of-plane. Base on the slopes of Kratky-Porod plot for NCS1, the in-plane slope was steeper than the out-of-plane slope. The steeper the slope, the larger the radius would be. The in-plane radius revealed a value of 6.3 nm, while out-of-plane radius was 1.7 nm. Thus, the elliptic cylindrical pores shape presented in the matrix which was directed parallel to the substrate for NCS1 film.
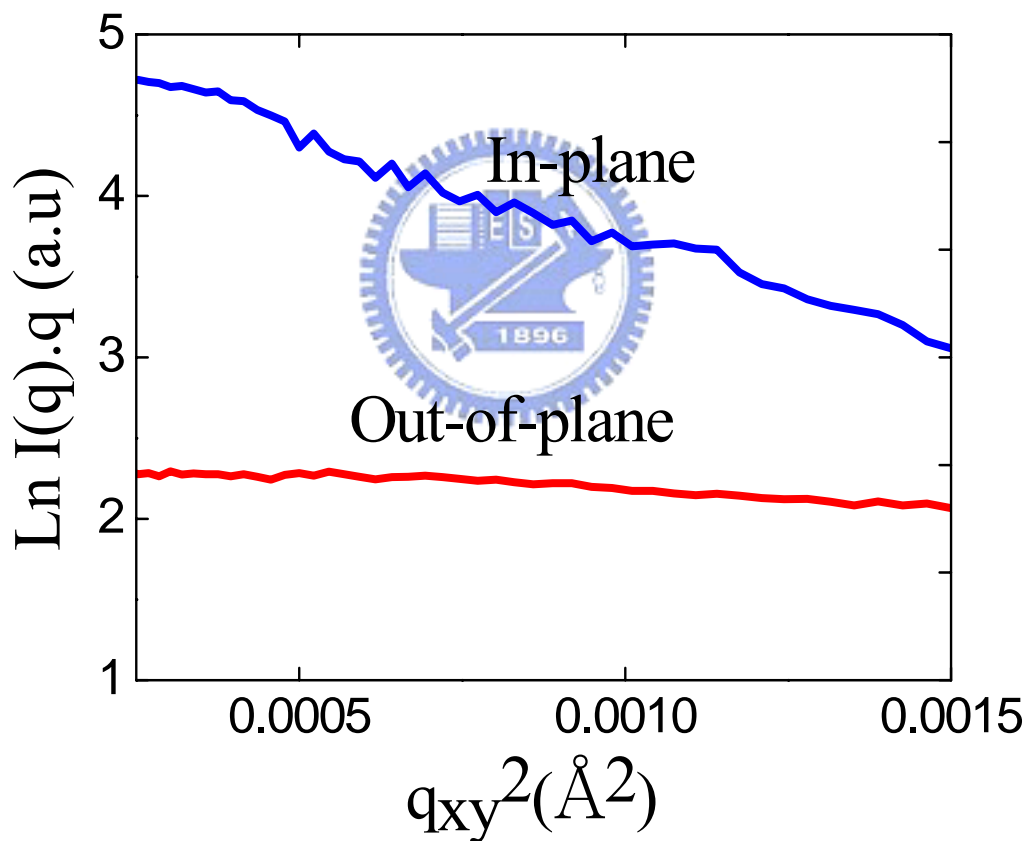
Figure 4.8 Kratky-Porod plot for NCS1 sample with elliptic cylindrical pore shape

Quantitative information about NCS2 through NCS5 low-k films scattering patterns could be extracted and approximated by using Guinier approximation. The Guinier approximation plot was further characterized to quantify the pore sizes for

NCS2 to NCS5 low-k films. Figure 4.9 showed ln I(q) versus q_{xy}^2 of NCS2 sample either in-plane and out-plane. Apparently, for NCS2 scattering pattern, both in plane and out of plane initial slope reveal almost the same magnitude which direct to assumption that pores shape was approximately spherical.

Since ln I(q) *versus* q_{xy}^2 for NCS2 through NCS5 also revealed the same slopes between in-plane and out-plane profile, only the in-plane ln I(q) *versus* q_{xy}^2 was illustrated in Figure 4.10 for NCS3 through NCS5 films. The slopes of Guinier plot for NCS2 through NCS5 samples, showed a very similar tendency. Initial observation of low-q region slope, NCS2 has maximum and minimum radius of pore, those are spherical pore size with R_{min} of 3.3nm and R_{max} of 10.5nm. In other case for NCS3 through NCS5, there was no significant difference between those slopes. The obtained Guinier pore size values were summarized in Table 4.5.
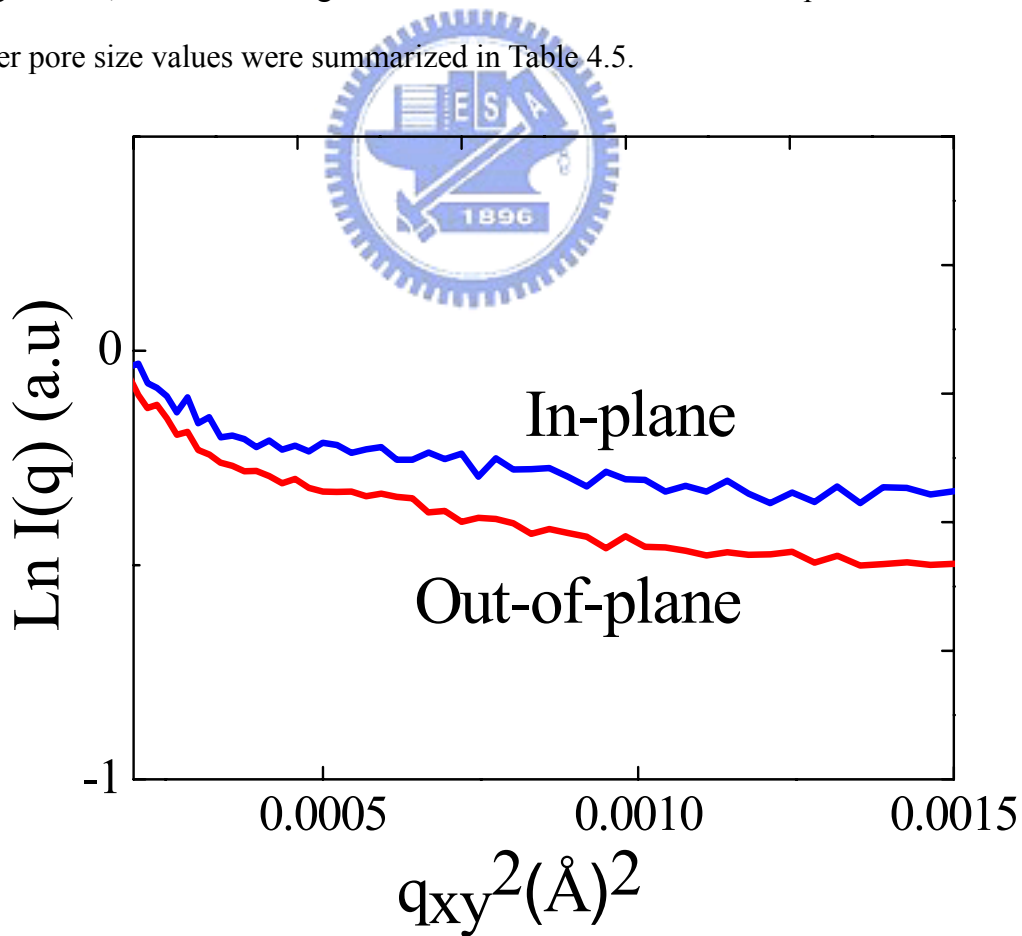
Figure 4.9 Guinier plot for NCS2 low-k film spherical pore shape
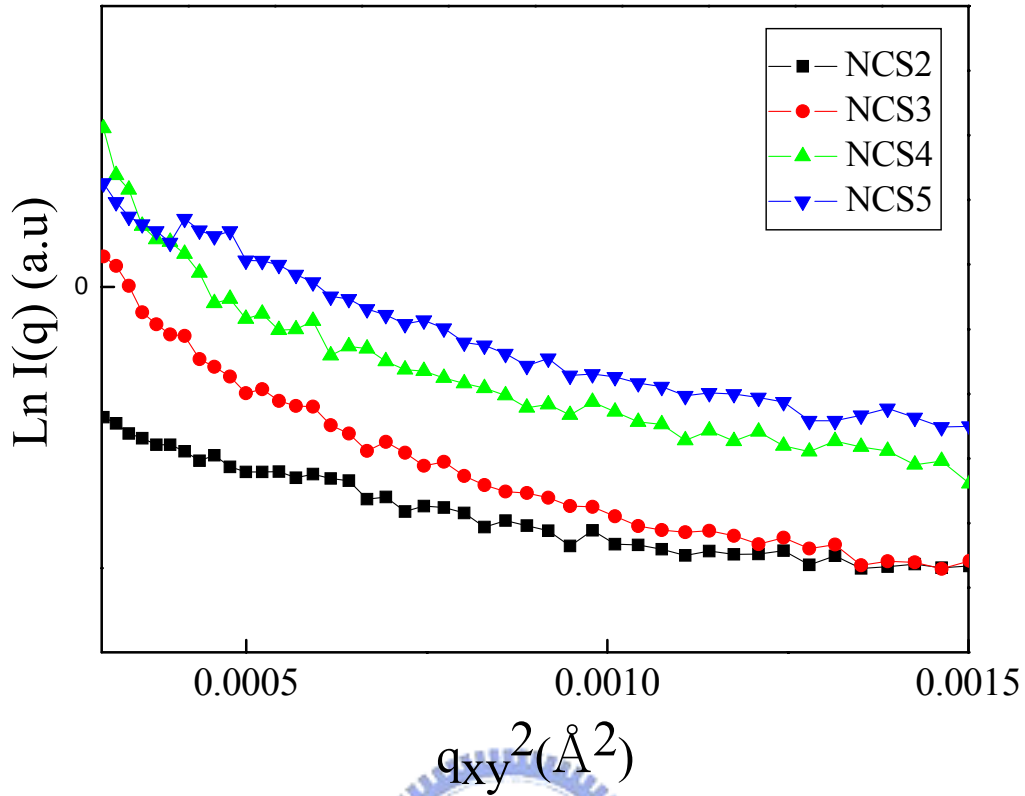
Figure 4.10 Guinier plot in-plane direction for NCS2 through NCS5 low-k films with spherical pore shape

In principle, the average distance between pores (D) could be determined from intensity maximum (q_{xymax}) which belonged to the structure factor S(Q). Thus,

$$D = \frac{2\pi}{q_{xy}} \tag{4.13}$$

As illustrated in Figure 4.11, the in-plane intensity *vs*. q_{xy} curves were plotted. The entire pore to pore correlation peak showed very broad distribution especially for NCS2 sample which was the broadest. This was probably due to our NCS films was thoroughly amorphous silica low-k film. Other explanation might be inferred to that the pore to pore distance was not very significant inside the matrix film. Thus based on the peak appearance, Table 4.5 summarized the pore to pore distance of NCS2

through NCS5 samples in horizontal direction. No correlation was observed in vertical direction.
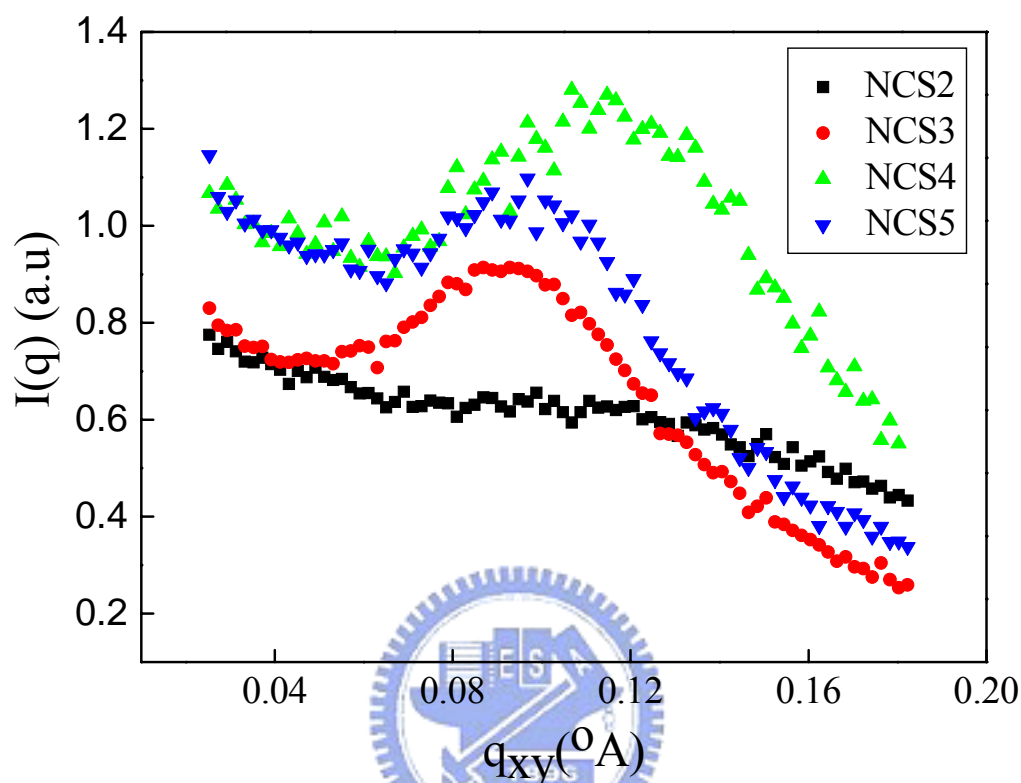
Figure 4.11 Intensity *vs.* q_{xy} plot to determine the pore to pore correlation distance

Table 4.5 Pore to pore distance and guinier pore radius estimation for NCS2 to NCS5 NCS low-k films

CT-samples	$Qxy(\text{Å})$	Pore to pore distance (D) (nm)	Range of pore radius size (nm) (Guinier)
NCS2	0.145	4.3	3.3-10.5
NCS3	0.098	6.3	4.7-9.4
NCS4	0.131	4.7	4.5-8.6
NCS5	0.106	5.9	4.5-8.2

Summarizing from first approximation by using Kratky-Porod plot and Gunier approximation has been performed which revealed that NCS1 possessed elliptic cylindrical pore shape, NCS2 to NCS5 possessed spherical pore shape. Hence, in the

next section, pore size, shape and distribution would be characterized by using fitting analysis to articulate whether approximation method was in a good agreement with fitting method.

4.3.3 Pore size, shape, and pore size distribution by GISAXS data fitting analysis and Schultz size distribution

The fitting of intensity versus q_{xy} was also carried out as showed in Figure 4.12 for NCS1 low-k film as elliptic cylindrical pore and Figure 4.13 for NCS2 to NCS5 as spherical pores. Figure 4.12 displayed NCS1 fitting profiles based on both elliptic cylindrical and spherical pore model. For spherical model in NCS1 film, the tail of fitting line rose up and deviated from the initial intensity profile. In elliptic cylindrical fitting line, the tail matched up well with the initial intensity profile. Therefore, NCS1 scattering intensity profile could be better fitted as elliptic cylindrical shape rather than spherical shape. The obtain diameter values are 19Å for out-of-plane and d= 33Å for in-plane. This agreement fit very well with the Kratky-Porod approximation assuming an elliptic cylindrical pore shape pore in NCS1 sample. This was very reasonable for well-defined scattering pattern as the one shown by NCS1 sample. Thus, the Kratky-Porod approximation could be consistently used.

Although the diameter value obtained was not totally equivalent between Kratky-Porod approximation and fitting result. Therefore, from preliminary Kratky-Porod approximation, the shape and size of NCS1 low-k film was determined to be elliptic cylindrical shape and size slightly larger than result from the fitting analysis.
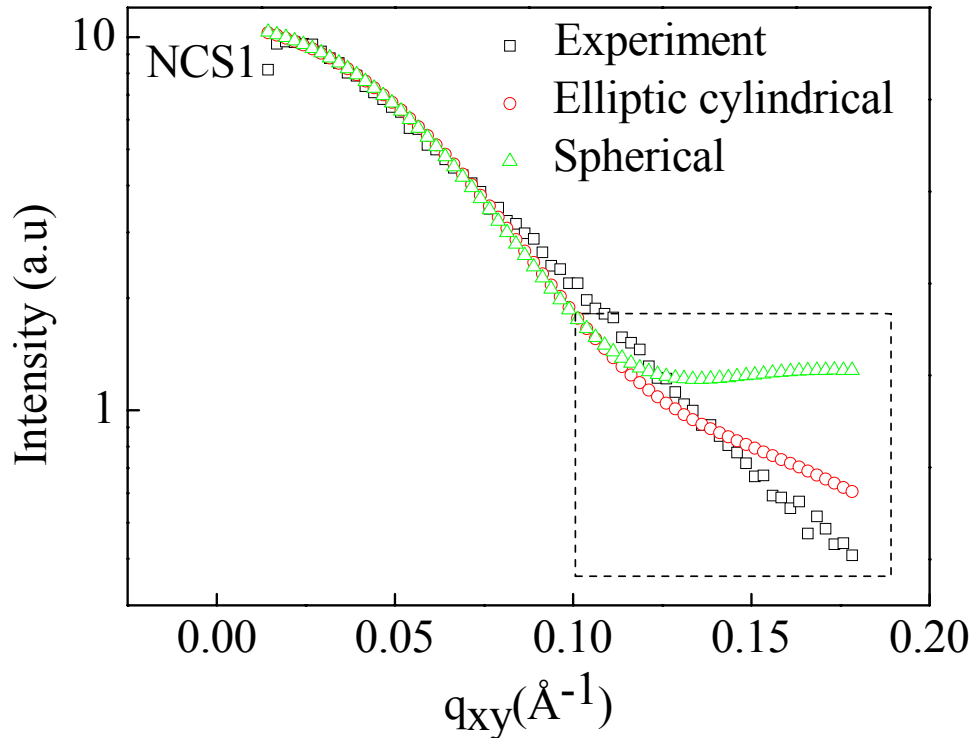
Figure 4.12 NCS1 low-k Intensity versus q_{xy} fitting curve.

Subsequently, the pore sizes for NCS2 through NCS5 films were also further calculated from the fitting intensity versus q_{xy} using spherical shape. Figure 4.13 showed the fitting lines matched well with the initial curves of NCS2 to NCS5 samples. This proved that the data could be simulated reasonably well using a spherical shape. Table 4.6 summarized the fitted parameters for NCS2 through NCS5. The two parameters of size distribution R_{avg} and σ were obtained by a least square fitting. R_{avg} indicated the mean radius of pore observable entirely and σ was the polydispersity.

Furthermore, the resultant pore size distributions derived from Schultz size distribution function fitted by the optimized parameters were shown in Figure 4.14. The peak value (D_p) was the most likely observed diameter in the distribution. [145] The most likely pore diameters observed for NCS2 to NCS5 were 0.46 nm, 0.31 nm, 0.48 nm, and 0.4 nm., respectively. The pore size distribution was all under control in the diameter smaller than 10 nm. The micropores (d < 2nm) predominantly presented

in the matrix of NCS2 through NCS5 low-k wherein NCS2 low-k revealed the narrowest pore size distribution compared to others. The pore size distributions derived from fitting analysis were in well agreement with the initial approximation using Guinier approximation, which also revealed the pore size that was smaller than 10 nm in diameter.
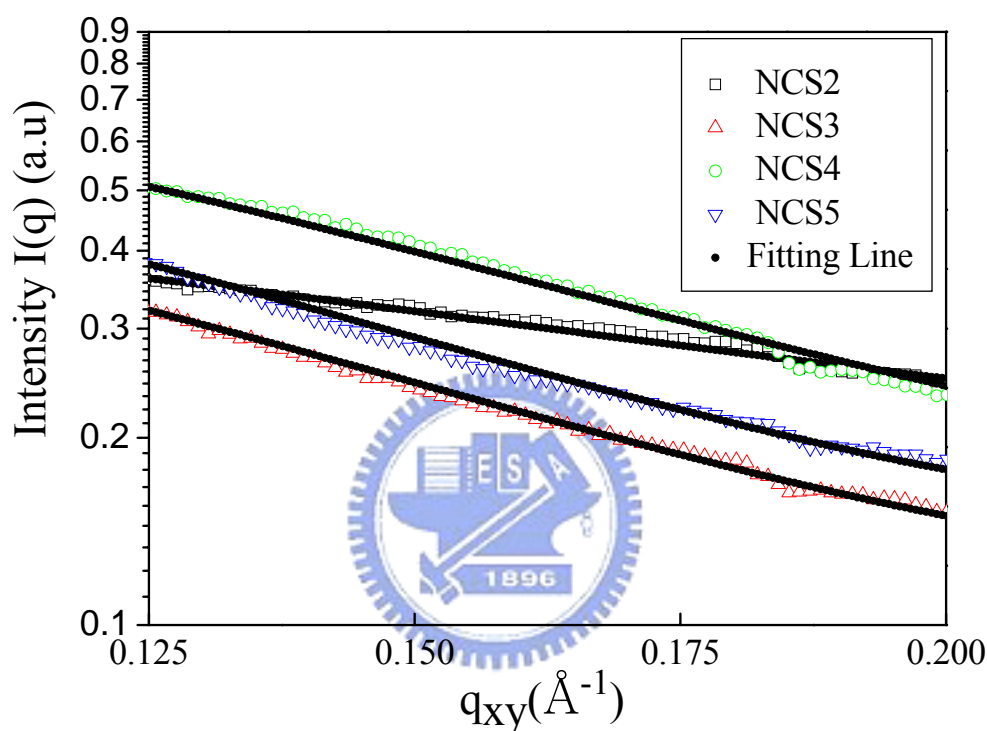
Figure 4.13 Intensity *vs.* q_{xy} fitting curves for NCS2 to NCS5 low-k materials. Black dot lines referred to the fitting lines

Table 4.6 The fitted parameters from size distribution for NCS2 to NCS5 low-k with spherical shape pores

NCS low-k	R_{avg} (nm)	σ (%)	D_p (nm)
NCS2	1.31	18.73	0.46
NCS3	1.63	11.32	0.31
NCS4	1.55	16.64	0.48
NCS5	1.64	13.63	0.40
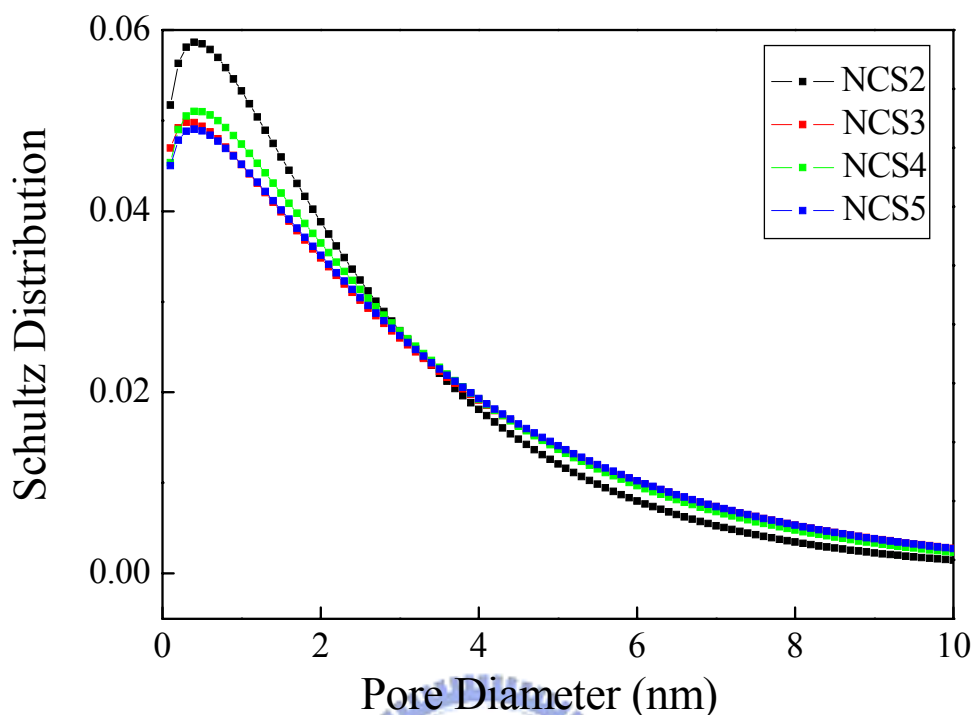
Figure 4.14 Pore size distributions of NCS2 to NCS5 low-k with spherical shape
pores

In summary, good agreement was shown by Kratky-Porod and Gunier approximation with fitting analysis outcome. Pore shape was described reasonably well instead of pore diameter which revealed a slightly larger value for approximation methods compared to fitting method.

Overall, the elliptic cylindrical pore shape of NCS1 low-k was observed because of the incorporation of large amount of methyl groups and higher porosity content leading to the collapse of structure during the cure step, thus elliptic cylindrical pore shape in vertical direction. This hypothesis was validated by the aforementioned data of ^{29}Si-NMR and FT-IR that NCS1 low-k had the less dense structure and higher porosity.

Pore size feature for NCS2 to NCS5 was spherically shaped and dominantly consisted of micropore. NCS2 has the narrowest pore size distribution compared to

NCS3 to NCS5. NCS2 to NCS5 low-k films owned stronger Si-O-Si linkage structure and lower porosity, therefore would not cause the damage of spherical pores during thermal cycle.

4.4 Mechanisms on the pore formation and pore collapse

Formation of pores inside the amorphous Si-O-Si matrix was derived after the high temperature 400 ^{o}C thermal curing process. The burnt out or decomposition of organic compound would generate pores inside the Si-O-Si linkage matrix. Generally, porous NCS low-k film's pores were generated from the organic moieties structure directing agent (SDA). The structure directing agent that NCS provided was tetrapropylammonium hydroxide (TPAOH). TPAOH has hydrophilic head group and hydrophobic end group. The hydrophobic end group was the long alkyl chains. Figure 4.15 demonstrated the typical micelle that formed when TPAOH was mixed with other hydrophilic precursor like silica (SiO$_2$) precursor (TEOS or MTMS) and water. These micelles were also called cluster for nano-clustering silica (NCS) films. The cluster size formed depended on TPAOH concentration. Lower TPAOH concentration produced smaller silica cluster, thus smaller pores, because smaller silica cluster can be packed more efficiently. (read this again)

Classification of pores by IUPAC could be divided into three categories based on the internal wide (w) listed as below: [146]

1.   micropores: w < 20 Å

2.   mesopores: 20 Å ≤ w ≤ 500 Å

3.   macropores: w > 500 Å

From above mentioned GISAXS results, NCS low-k films' pores mainly consisted of primary micropores and in the present of small amount of mesopores.

The micropores originated from initial alkyl chain length that was decomposed at elevate temperature at temperature around $350°C$ $-400°C$ and mesopores was formed through the packing of clusters inside the amorphous Si-O-Si matrix. The size of cluster formed was also smaller for the condition with lower TPAOH concentration. The packing of nano-cluster also influenced the mesopores that formed surrounding the nano-cluster and amorphous Si-O-Si. The alkyl chain would be burnt out and form pores inside the matrix of Si-O-Si. Therefore, the TPAOH concentration influenced the pore size and porosity in the way of micropores and mesopores formation.
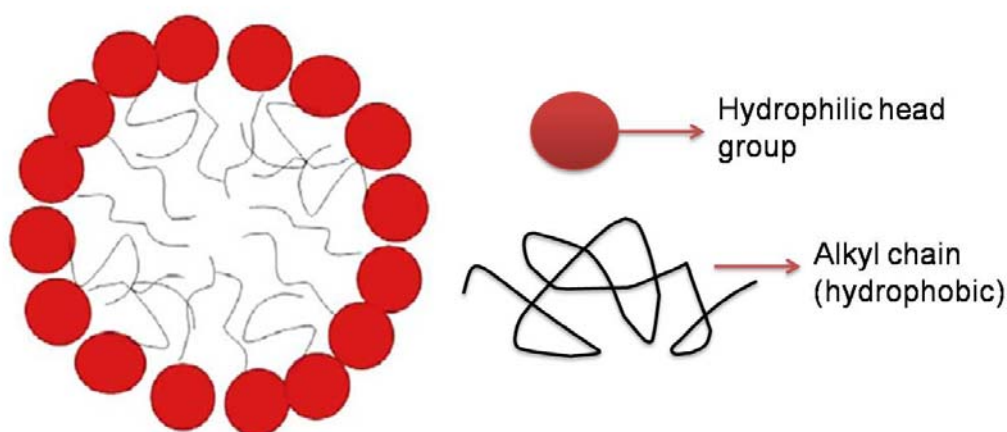
Figure 4.15 Micelle/cluster formation of structure directing agent

More information obtained from GISAXS revealed that NCS1 porous low-k film possessed elliptic cylindrical pore shape ($d_{in-plane}$ = 3.3 nm $d_{out-of-plane}$ = 1.9 nm) and NCS2 to NCS5 porous low-k films possessed spherical pore shape (d < 10nm with most population in the d = 0.5 nm).

Furthermore, the behavior of pore shape was related to the porosity and crosslink degree of Si-O-Si matrix because the porosity was the largest and the degree of crosslinking (Q-group in ^{29}Si-NMR) was the lowest for NCS1 film. Under such circumstances, too high porosity which exceeded the limit of percolation threshold

and least crosslink matrix would make the NCS1 film not sustain the thermal processing and tend to collapsed to form more stable structure. As a result, the initial spherical pore shape degraded and formed elliptic cylindrical pores with thickness degradation of 40%.

In contrast, due to lower porosity film and higher cross-link Si-O-Si matrix, NCS2 to NCS5 low-k films would maintain the spherical pore shape and only degrade for less than 8% thickness as shown in Figure 4.16.
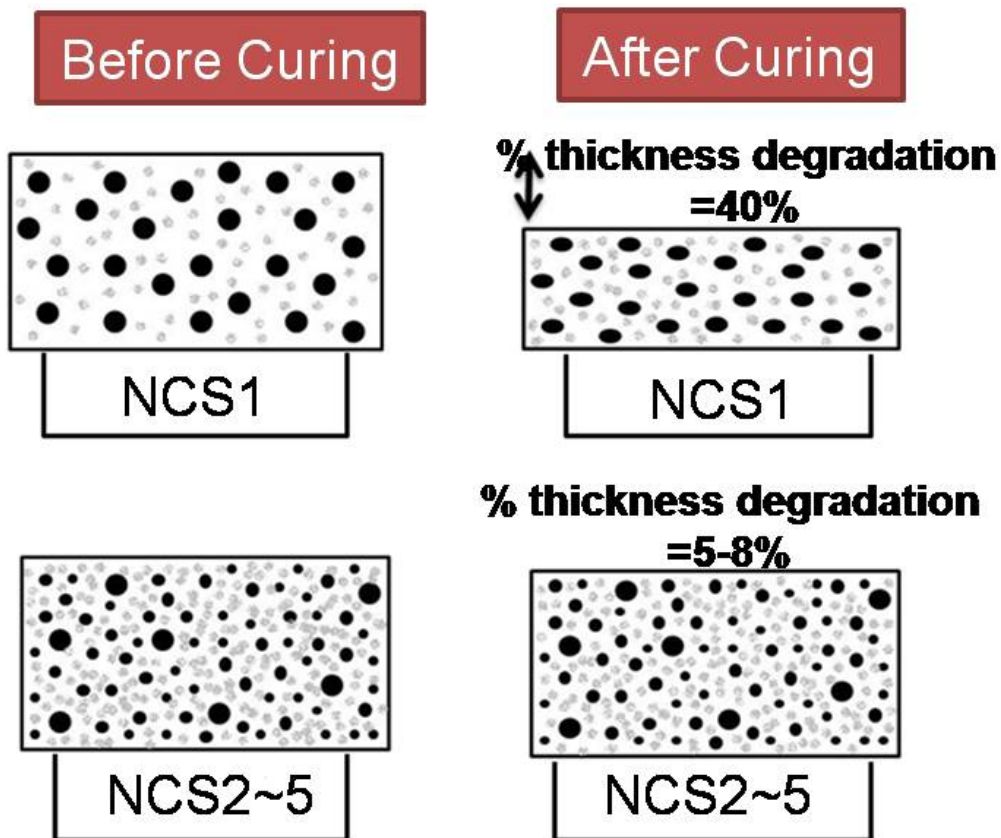
Figure 4.16 Illustration of film thickness degradation during thermal curing process. Matrix Si-O-Si linkage (black spray) and pores (black circle).

4.5 Dielectric Property

Capacitance versus area curve fitting method was applied to determine dielectric constant values of NCS1 to NCS5 low-k films as shown in Figure 4.17 in terms of porosity obtained by XRR. NCS1 low-k film revealed the lowest dielectric constant because of its higher Si-CH$_3$ groups and higher porosity. NCS5 showed the highest dielectric, 2.8 presumably due to its lower porosity (18.7%) and lowest T-group/Q-group ratio (0.68 listed Table 4.3). As the T-group/Q-group ratio and porosity increased from NCS5 to NCS2, the dielectric constant was reduced accordingly down to ~2.3.
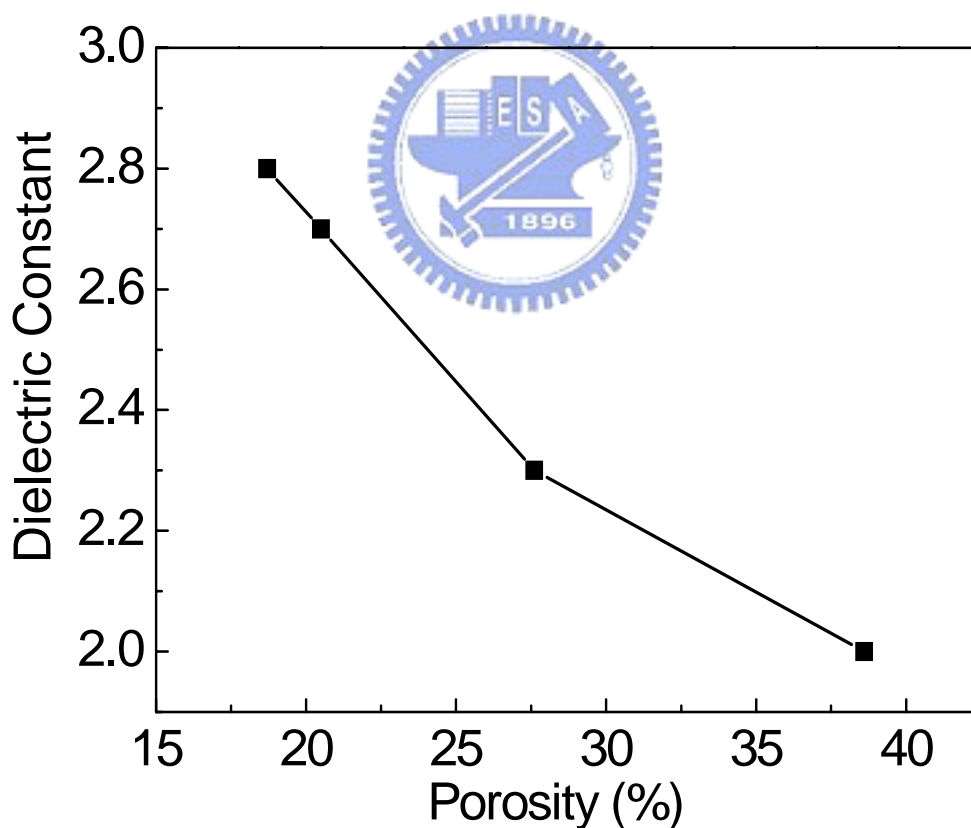
Figure 4.17 The dielectric constant versus porosity for NCS low-k films

4.6 Mechanical Property

4.6.1 Mechanical modulus and dielectric constant

Figure 4.18 demonstrated modulus versus dielectric constant of NCS films. Modulus increased almost linearly (9 to 13 GPa) as dielectric constant increased for NCS2, NCS4 and NCS5 low-k films. However, NCS1 possessed the lowest modulus 2.76 GPa, which detrimentally deviated from the linear extrapolation of NCS2-NCS5. The weak mechanical modulus of NCS1 was confirmed by FT-IR blue shift phenomenon that NCS1 has weakest Si-O-Si bonding and higher methyl Si-CH$_3$ content. ^{29}Si NMR study also showed the same outcome based on relatively high T-group/Q-group ration, ~4.0. Moreover, NCS1 also has the highest porosity (ρ =38%) as compared to other NCS films (ρ<27%).

Therefore, the modulus of NCS films was decreased under the influenced of porosity and less cross-link matrix. NCS1 possessed the lowest modulus of 2.76 GPa, others NCS low-k exhibited higher modulus in the range of 9-13 GPa. The dotted line could represent another point of view of modulus versus dielectric constant, under the same dielectric constant of κ= 2, the modulus of linear line was only dropped to 5-6 GPa. Therefore, modulus of NCS1 could be improved by modified the silica matrix precursor become higher cross-link system and slightly lower porosity (ρ<38%).
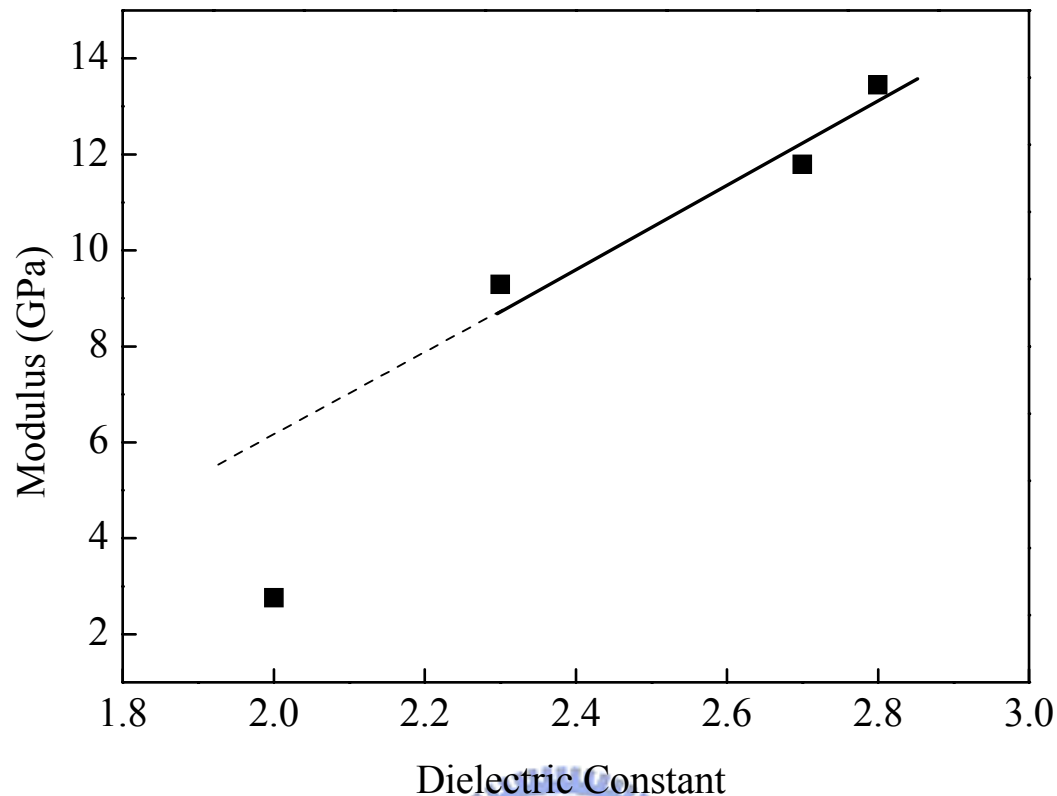
Figure 4.18 Modulus versus dielectric constant of NCS low-k films.

4.6.2 The effect of matrix cross-link on mechanical modulus

The degree of cross-link of NCS low-k films have already been described in the FT-IR section. The modulus of NCS low-k films were plotted with respect to FT-IR network/cage ratio as shown in Figure 4.19. Since cross-link degree of NCS low-k films could be represented by network/cage ratio, higher Si-O-Si network content would possess higher cross-link. Modulus of NCS low-k films increased with increasing network/cage ratio. The lowest modulus was shown by NCS1 film, since its matrix predominately consisted of Si-CH$_3$ bonding which yielded lower cross-link compared to Si-O-Si network bonding. Therefore, by replacing tetrahedral Si-O bond with three Si-O bond would reduce the modulus and dielectric constant, respectively. As reported by V. Jousseaume, *et al,* the skeleton structure was correlated to the elastic properties whatever the deposition technique used. Si-O-Si bond concentration

was the elastic properties key parameter.[147] Therefore, the least cross-link NCS1 matrix would cause the modulus dropped robustly.
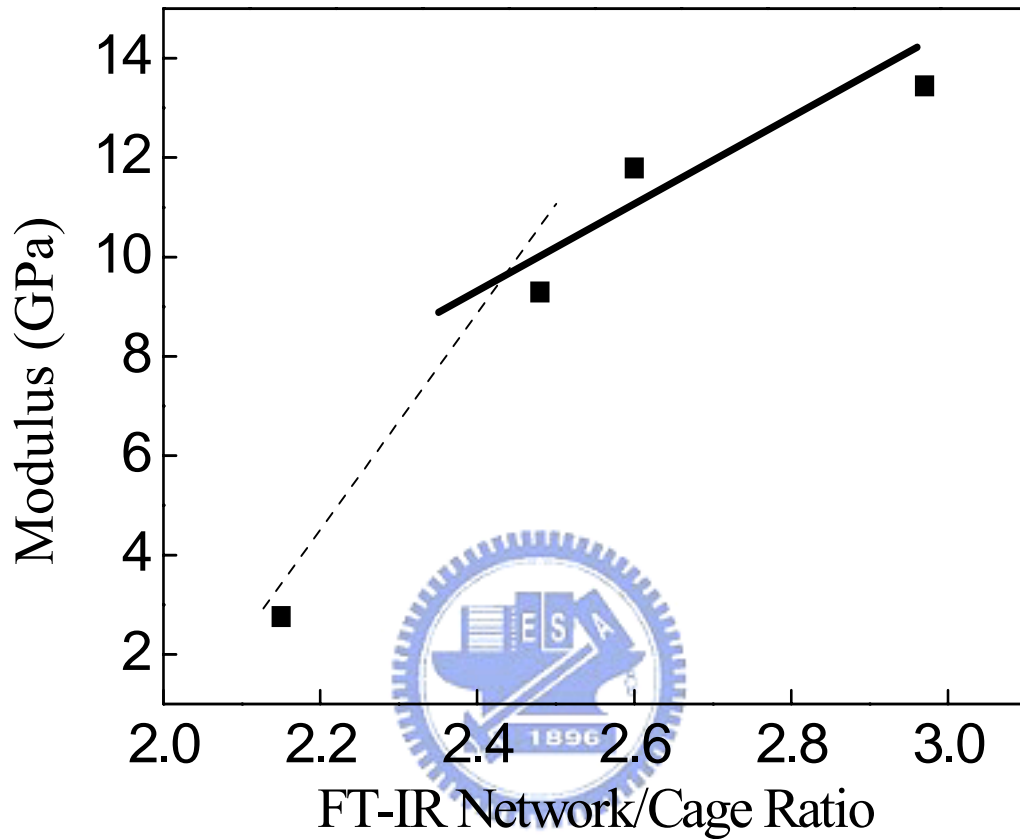
Figure 4.19 Relationship of modulus versus FTIR network/cage ratio

4.6.3 The effect of porosity on mechanical modulus

The effect of porosity on mechanical modulus could be explained through the power law exponential correlation expressed by Equation 4.14. [148]

$$E = E_0 (1 - P)^n \tag{4.14}$$

where E and E_0 were the elastic modulus of volume fraction porosity P and zero porosity. "n" described the material dependent constant.

The resulted fitting model was $E=25(1-P)^{3.2}$ for NCS2 through NCS5 with maximum goodness of fit (GOF) equal to 0.94. Remarkably, the modulus at zero porosity (E_0) or dense matrix yielded a modulus of 25 GPa. The fitting curve in Figure 4.20 only displayed the fitting curve for NCS2 to NCS5 data point because NCS1 was different in chemical composition. Therefore, NCS1 could not be included in the fitting profile. The almost linear relationship between modulus and porosity was shown inclusively. Generally, the exponent "n" was equal to n=2 for smaller closed pores. [150, 151] Others reported that a power law exponent of n=3 when pore connectivity was included (overlap). [152] The higher value of n=3.2 explained that the modulus was greatly influenced by the volume fraction of porosity and the pores were randomly distributed and connected to each other. The more disorder pores appeared to has higher n-value compare to order one. [153] Modulus dropped substantially from 13.4 GPa of NCS5 to 9.29 GPa of NCS2 as the porosity increased from 18.7% to 27.6%. As already discussed above, the modulus of NCS low-k films also influence by matrix cross-link in the way that modulus increased with increasing network/cage ratio. Therefore, modulus of NCS2 to NCS5 increased as increasing the network/cage ratio and decreasing porosity.

NCS1 showed lowest modulus which was only 2.76 GPa. The drastic modulus degradation of NCS1 film could be attributed to its less dense Si-O-Si structure and less amount of highly crosslink Q structure, $[(SiO)_4Si]$ as elucidated by FT-IR and ^{29}Si NMR, in addition to the increased in porosity to 38.6%.
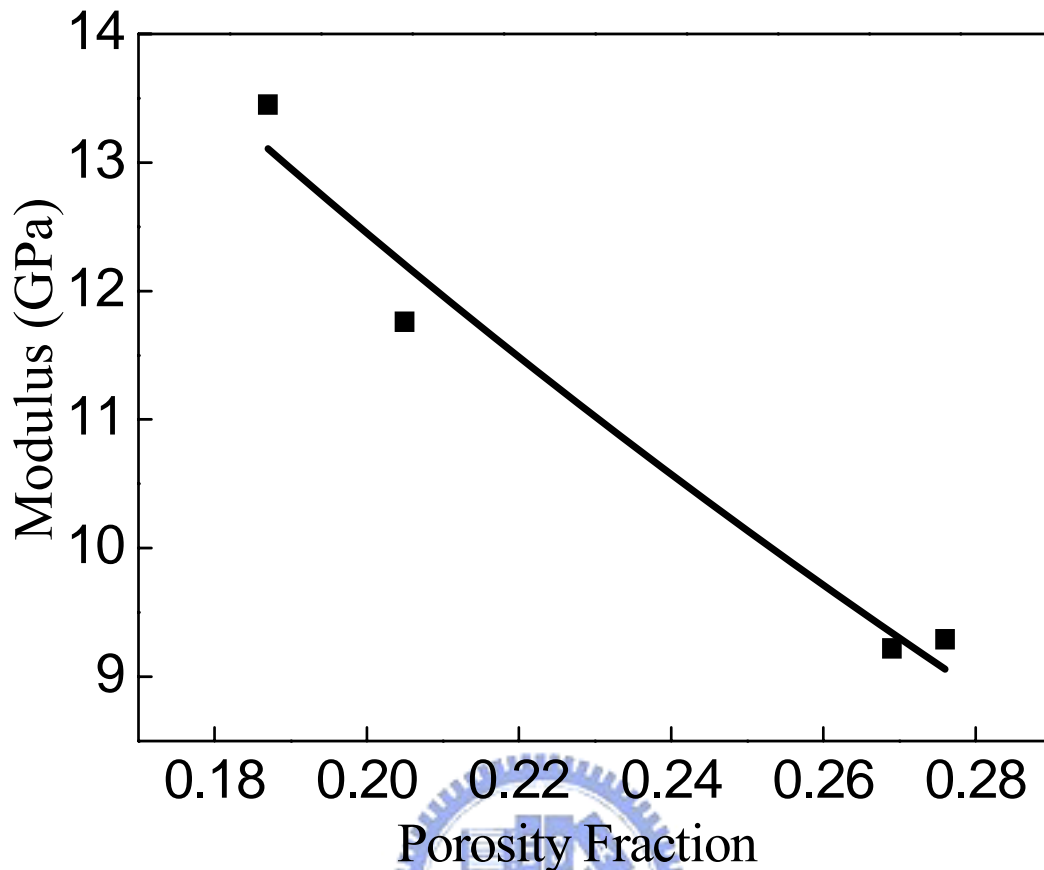
Figure 4.20 Modulus of NCS low-k versus porosity. The power law modulus versus porosity fitting curve was shown in black line.

4.6.4 The effect of pore shape on mechanical modulus

The mechanical modulus behavior which played the most important role as a basic requirement of utilization of low-k dielectric material would be our main concern. Various factors influenced the mechanical modulus of low-k film listed as pore aggregation during thermal curing, [154] pore arrangement, [155] film shrinkage during thermal curing. [156] As reportedly by H. Miyoshi *et.al* [109] pore size distribution or pore position distribution was not the main killer or defect that caused the drastic degradation in modulus as long as there is no aggregated pores.

According to GISAXS NCS low-k structural information, NCS1 low-k film possess elliptic cylindrical shape pores which were aligned parallel to the substrate,

while NCS2 to NCS5 low-k film possessed spherical shape pores inside the amorphous silica matrix. Furthermore, the mechanical modulus of is GPa for NCS1 and 9-13 GPa for NCS2 to NCS5 NCS low-k films based on nano-indentation method. For that reason, NCS2 spherical shape pores provided better mechanical modulus compared to NCS1 elliptic cylindrical shape pores. It was determined that the delicate behavior of NCS1 elliptic cylindrical shape pores related to the shrinkage during thermal curing. The relationship between pore shape and mechanical modulus itself has been studied widely in porous ceramic material field. As reported by Rice *et al*, the pore shape was related to mechanical modulus by Equation 4.15 below [157]

$$E = E_0(1 - BP)$$
(4.15)

where $E = E_0$ when P (porosity) was 0, B was a parameter related to the Poisson ratio. The parameter B was a function of pore shape. The value of B was related to the a/c or c/a of pore size as shown in Figure 4.21. The parameter B was smaller for pore with spherical shape and larger for elliptic cylindrical pore. Therefore the modulus also influenced by pore shape respectively. In the constant value of porosity, modulus was higher for spherical pores rather than elliptic cylindrical pore. [158]

Moreover, Elliptic cylindrical pores tend to weaken the NCS film modulus more than spherical pores due to a combination of a less well connected Si-O-Si linkage and greater stresses and deformation near the high curvature regions of the elliptic cylindrical pores. [159] Furthermore, H. Miyoshi et al [150] stated that the out-of-plane shrinkage of pores would decrease the elastic modulus of film. Thus, out of plane shrinkage must be suppressed for achieving the higher elastic modulus while keeping the k-value constant. Therefore, spherical shape pores also being one of the

most promising pores which could has high mechanical modulus as compared to elliptic cylindrical shape pores.
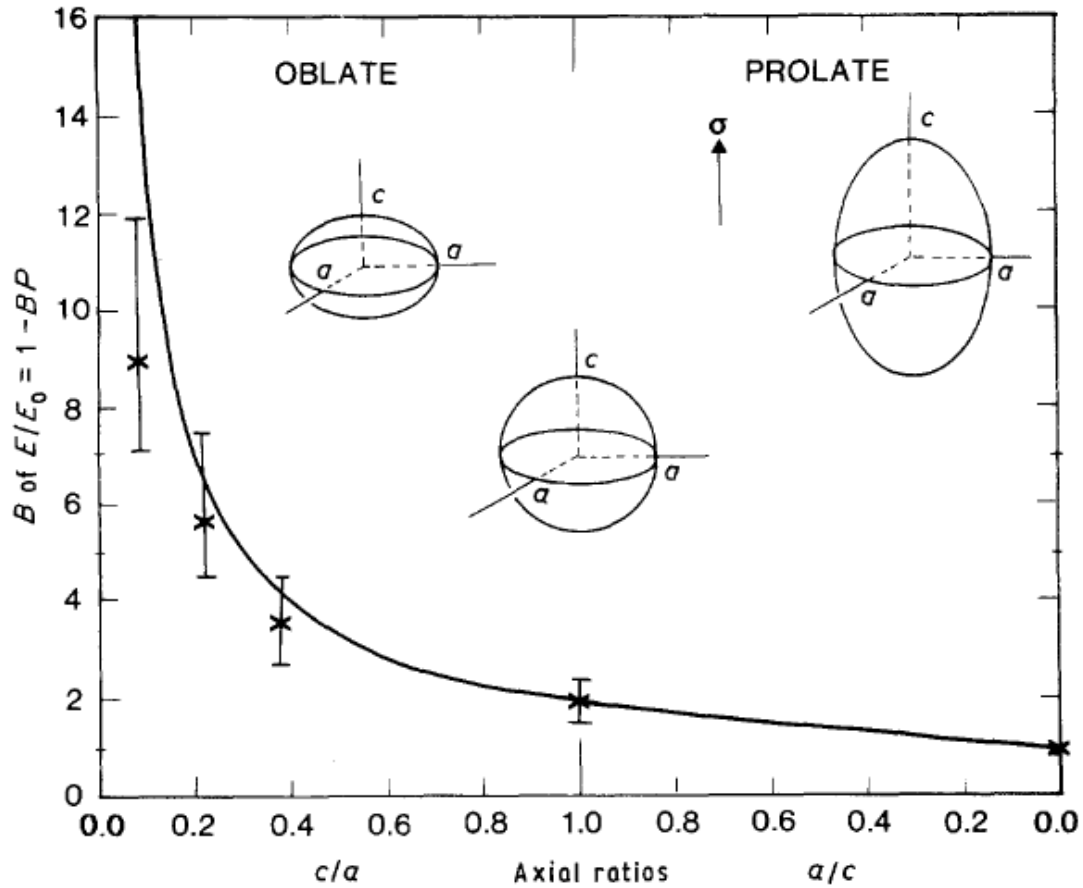
Figure 4.21 Plots of parameter "B" for equation pore shape related to modulus.

4.6.5 Factors affecting the mechanical modulus

From Section 4.6, detail discussion about factors that caused degradation of mechanical modulus has been fully described. The correlation of porosity, matrix cross-linking and pore shape have been related to mechanical modulus. Porosity and matrix crosslinking were the primary and secondary influences, while the pore shape was the alternative influence.

The initial matrix Si-O-Si linkage crosslink has been characterized through FT-IR and ^{29}Si-NMR. NCS1 demonstrated the least crosslink among all of the other NCS samples (NCS2 to NCS5). The lower wavenumber absorbance spectra of

80

Si-O-Si network structure and the lacking of Q_4 group $((SiO)_4Si)$ were the evidence of cross-link deficiency. NCS1 also revealed highest porosity that reached almost 40%. NCS2 to NCS5 showed higher cross-link Si-O-Si matrix which revealed from its higher Q_4 group $((SiO)_4Si)$ in the balance of $T_3[(SiO)_3Si(CH_3)]$ availability and higher wavenumber region Si-O-Si absorbance peak. NCS2 to NCS5 possessed different loading of porosity that was 27.6% and 18.7% respectively.

Another factor that influenced modulus was the pore shape. Since the modulus of NCS low-k films was measured subsequently after the formation of pore during thermal curing, therefore, the pore shape that formed also being influenced by the matrix cross-link and porosity that existed inside the thin film. Since low crosslink and high porosity would cause the matrix become loosen, as a result loosen matrix would tend to form more stable film structure and degrade in vertical direction which caused the inner spherical pores become elliptic cylindrical pores shape. Therefore, the pore shape that formed was mainly being the factor of matrix cross-linking and porosity. Pore shape was also a concern since modulus was obtained right after the pore formed inside the matrix film.

Furthermore, from Figure 4.22 engineering plot of modulus versus dielectric constant value was displayed. The square and fitted line were referred to amorphous silica low-k film, circle data points referred to experimental NCS low-k film and triangle data points referred to pure silica-zeolite low-k films. Pure silica-zeolite low-k films have modulus extremely higher than others because of its crystalline nature. Our experimental NCS low-k films have modulus slightly higher than conventional amorphous low-k films. Although NCS was also an amorphous low-k films, but it possessed small micropores and narrow pore size distribution, therefore under the same dielectric constant as amorphous low-k films, NCS low-k film still showed excellent mechanical modulus which was near to 10GPa. Instead for NCS1

low-k film which revealed mechanical modulus the same as amorphous low-k film, since NCS1 low-k film's majority of its matrix was composed of less crosslink Si-CH$_3$ domains.
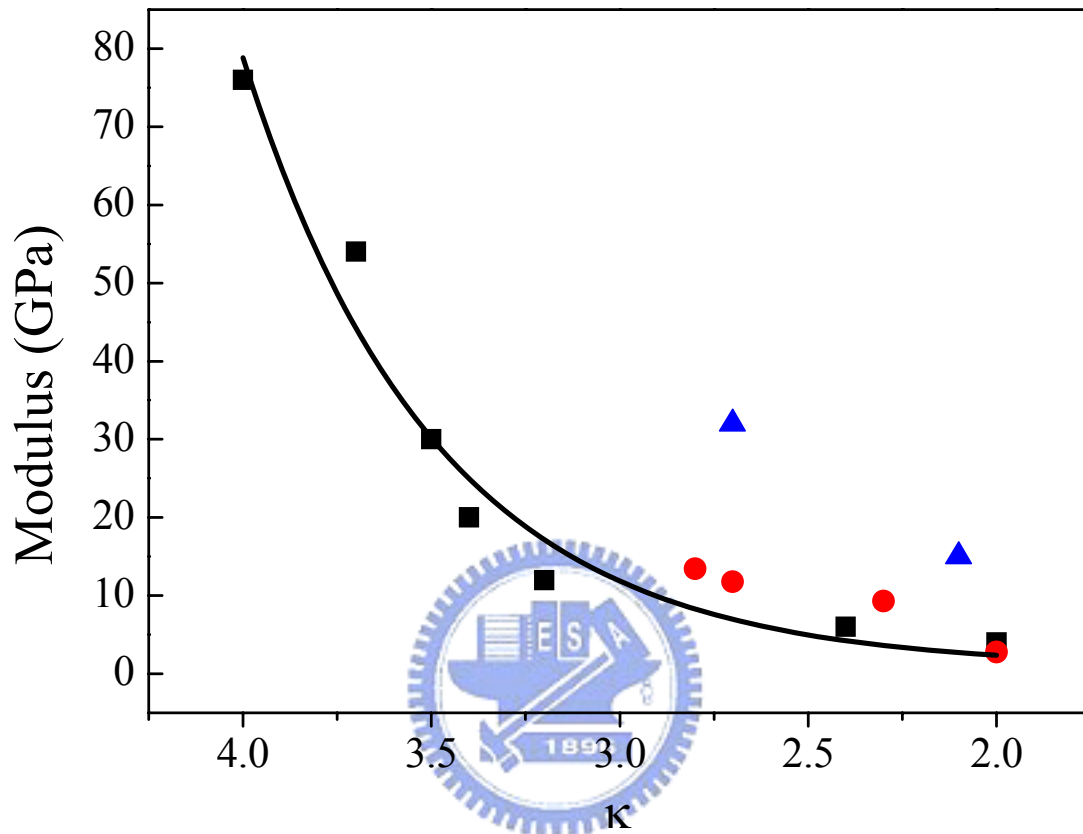
Figure 4.22 Modulus versus dielectric constant for various porous low-k films. Square and fitting line referred to amorphous silica low-k film, circle referred to experimental NCS low-k film, and triangle referred to pure silica-zeolite low-k film.

From the Section 4.6.3, NCS1 was excluded in the power law fitting section. Power law could only represent porous materials that shared the similar chemical composition but different in pores loading. Therefore, from the inquiry of FT-IR and ^{29}Si-NMR results, NCS1 could be classified into different chemical composition to others NCS films since it exhibited distinctive absorbance peak and larger amount of T$_3$[(SiO)$_3$Si(CH$_3$)] groups. NCS1 film possessed porosity equal to 38.6% and modulus of 2.76 GPa. Furthermore, extended through the power law fitting of NCS2

to NCS5 which resulted power law of $E=25(1-P)^{3.2}$. From this power law equation, further prediction of modulus if NCS1 has the similar chemical composition as NCS2 to NCS5, under the same porosity of 38.6%, prediction of NCS1's modulus would revealed higher modulus of 4.1 GPa compared to NCS1's experimental modulus of 2.76 GPa as shown in Figure 4.23. Under the same porosity, original NCS1's has lower modulus compared to prediction's one because original NCS1 possessed a matrixs mostly consisted of T_3 groups. From above discussion T_3 group originated from MTMS precursor, MTMS precursor itself has one terminal non-crosslinked methyl group (Si-CH$_3$). This non-crosslinked group offered more steric hindrance that would provide intrinsic pores. Intrinsic pores were defined by the pores that formed without the incorporation of pore generator (porogen). Commonly, MTMS was used as a silica precursor to synthesize poly(methylsilsesquioxane) (PMSQ). In the condition of 100% MTMS synthesized to form PMSQ would yield modulus as low as 4.5 GPa. This is primarily because the PMSQ monomers form a breadth of microstructure which including open networks, partial cages with relatively large cyclic structure and others more flexible Si-O-Si bond architectures that generally contribute to its low modulus. [160]

The maximum porosity or percolation threshold that could be incorporated into the NCS2 to NCS5 matrix condition was correlated to the modulus which reduced approximately to zero. In the situation of modulus approximately to zero, the corresponding porosity was 65%-70%. Therefore, the reduction of modulus was seriously influenced by porosity insertion. [161]
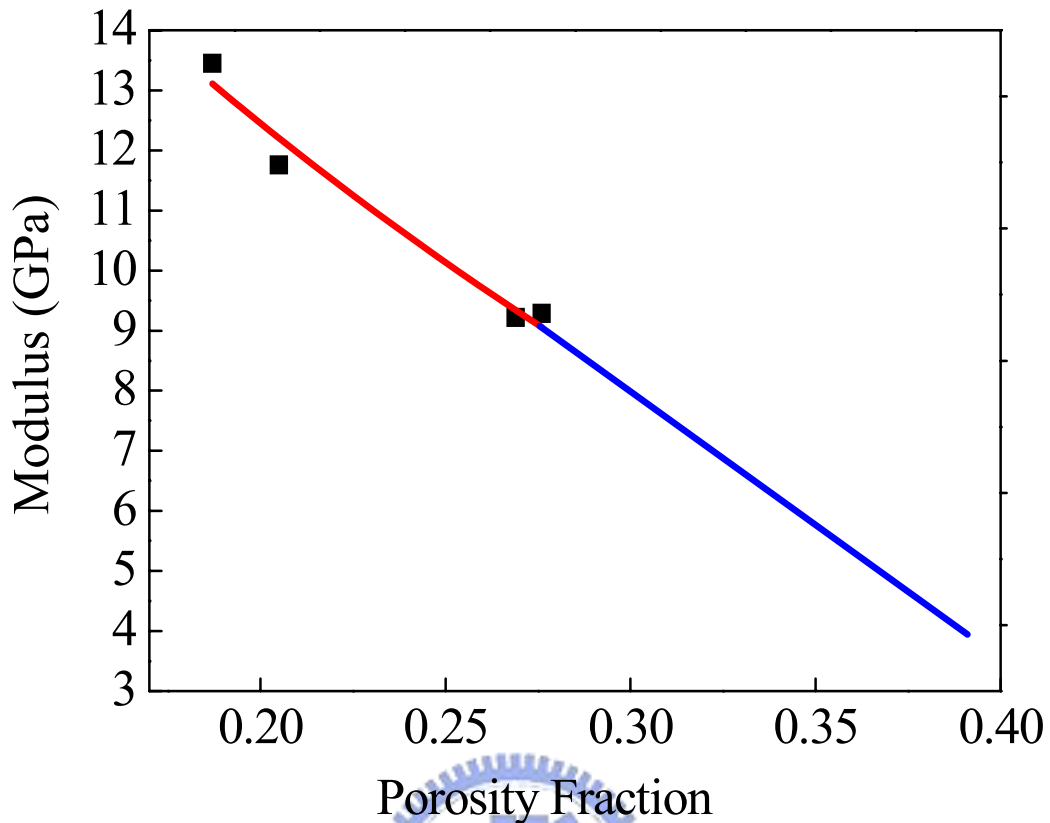
Figure 4.23 Prediction on extension of power law modulus versus porosity fraction
plot.

4.7 Thermo-mechanical property

The stress-temperature dependence of the NCS low-k films on Si substrate was shown in Figure 4.24. The thermal stress of 1st cycle was required to thermally stabilize the film. Afterward, 2nd cycle showed the same behavior of stress. Only the result of 1st thermal cycle was plotted in Figure 4.23. The positive stress (positive slope) showed that the NCS films on Si was subjected to tensile stress during thermal cycle. The nearly linear stress temperature curve indicates that the films deform elastically during thermal curing. The stress level of Si substrate for different NCS low-k films could be summarized in Table 4.7. With increasing temperature, the stress of the NCS films remains tensile. Thermal stress range increase as films was introduced to greater stress change when temperature raise up. The stress-temperature curve of NCS1 low-k film showed stable stress change during the temperature cycling.

NCS1 low-k film possessed higher porosity was a reason that Small stress change along thermal cycling. Since pores was one of the defect that stay in the Si-O-Si matrix, during thermal curing process, this defect site would become one of the thermal stress relieve site. Overall, the thermal stress range decrease with increasing porosity, indicating that the introduction of more pores would allow the low-k film became more compliant.
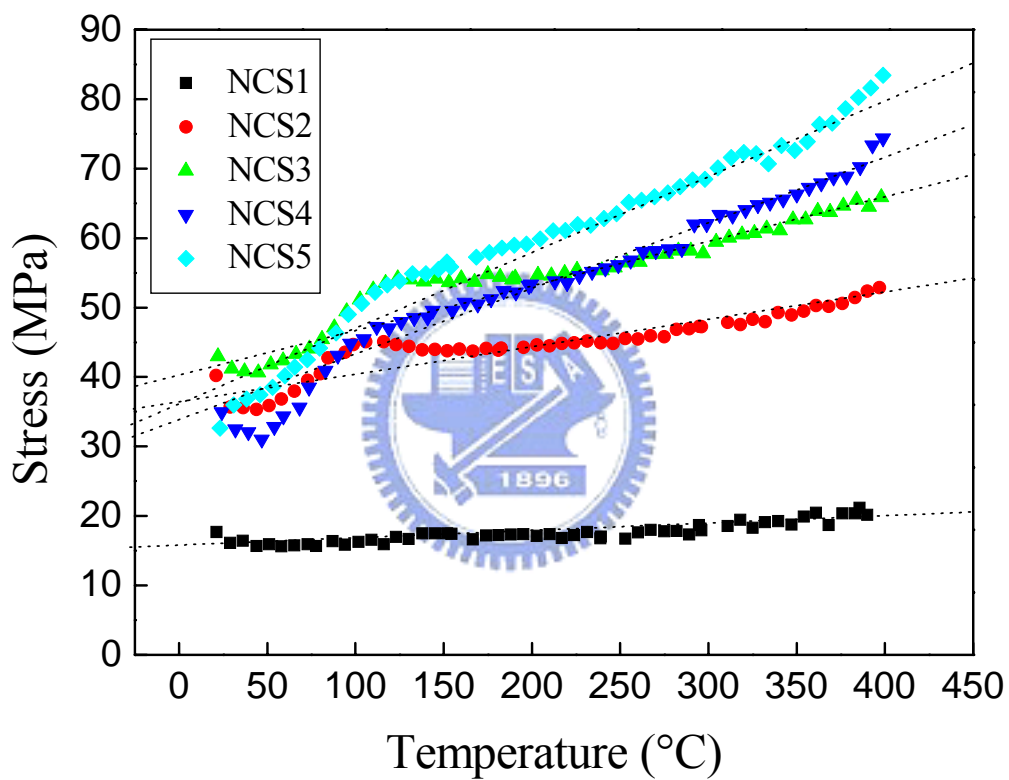
Figure 4.24 Thermal stresses of NCS low-films on Si-substrate

Table 4.7 Thermal stress range of each NCS porous low-k thin film

NCS low-k film	Thermal stress range (MPa) 25°C~400°C	Porosity (%)
	Si	
NCS1	15~20	38.6
NCS2	35~50	27.6
NCS3	40~65	26.9
NCS4	30~70	20.5
NCS5	30~80	18.7

4.8 Surface roughness analysis

The average surface morphology was measured by using AFM tapping mode system. An area size of 1 um x 1 um was scanned to measure the relative height of surface morphology. Root mean square (RMS) roughness was articulated by using nanoscope data analysis program. Figure 4.25 showed 2D surface image of each NCS low-k films. Higher RMS roughness was observed for NCS1 low-k film, while NCS2 to NCS5 showed the similar RMS roughness.
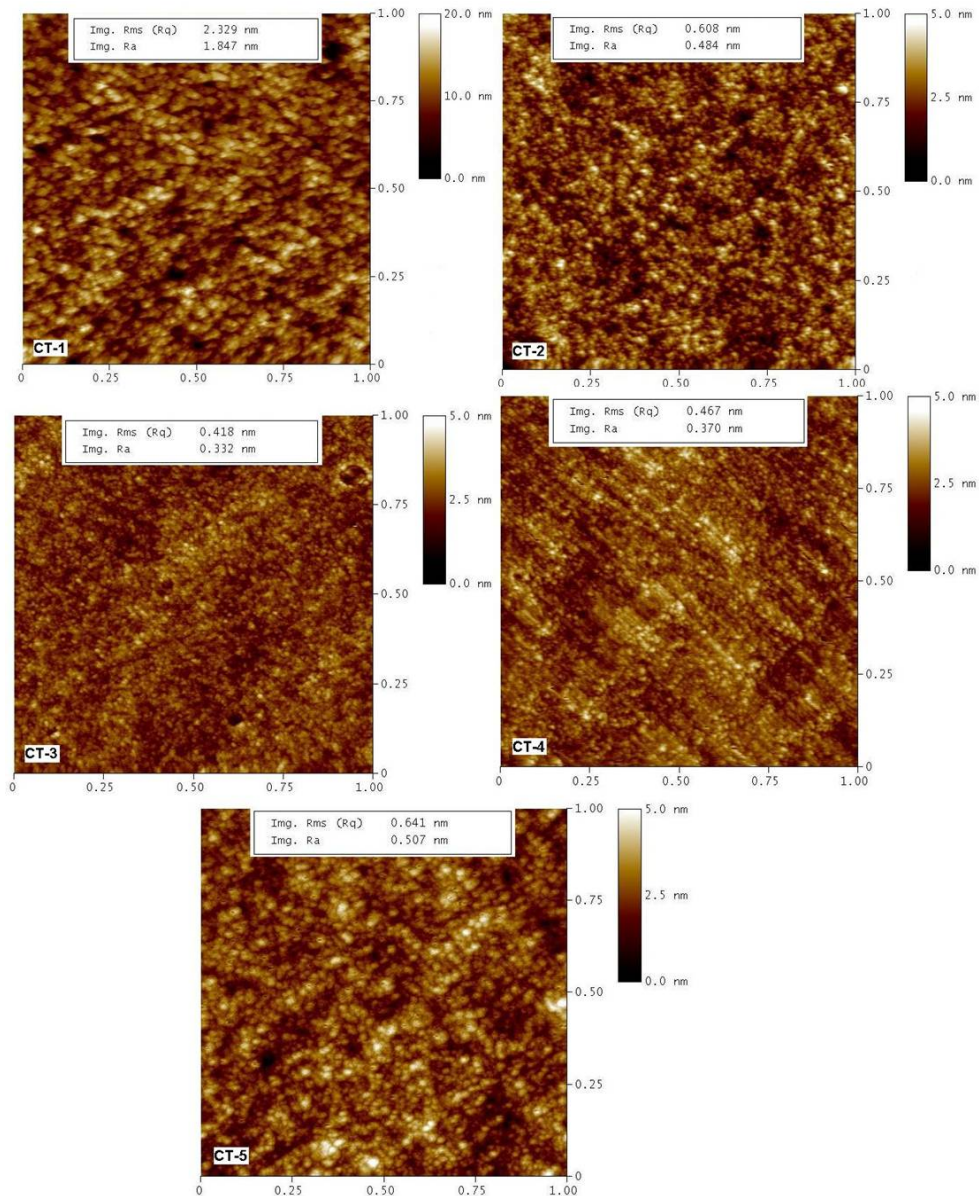
Figure 4.25 AFM image of NCS low-k films. The image size was 1 x 1 μm^2.

Figure 4.26 compared the surface roughness values obtained by AFM and XRR method for each NCS low-k films. Good surface roughness was illustrated by all NCS low-k films, in which only in the range of few nanometer root mean square roughness. As reported by S. Eslava *et al*, pure silica zeolite low-k film (PSZ) has high surface roughness because nano-particle in the size of ten of nanometers was formed.[162] Therefore, amorphous NCS low-k films with smooth surface were formed and with tightly control of pore size distribution. The smooth surface of porous NCS low-k did not need any extra polishing step as pure zeolite low-k film.
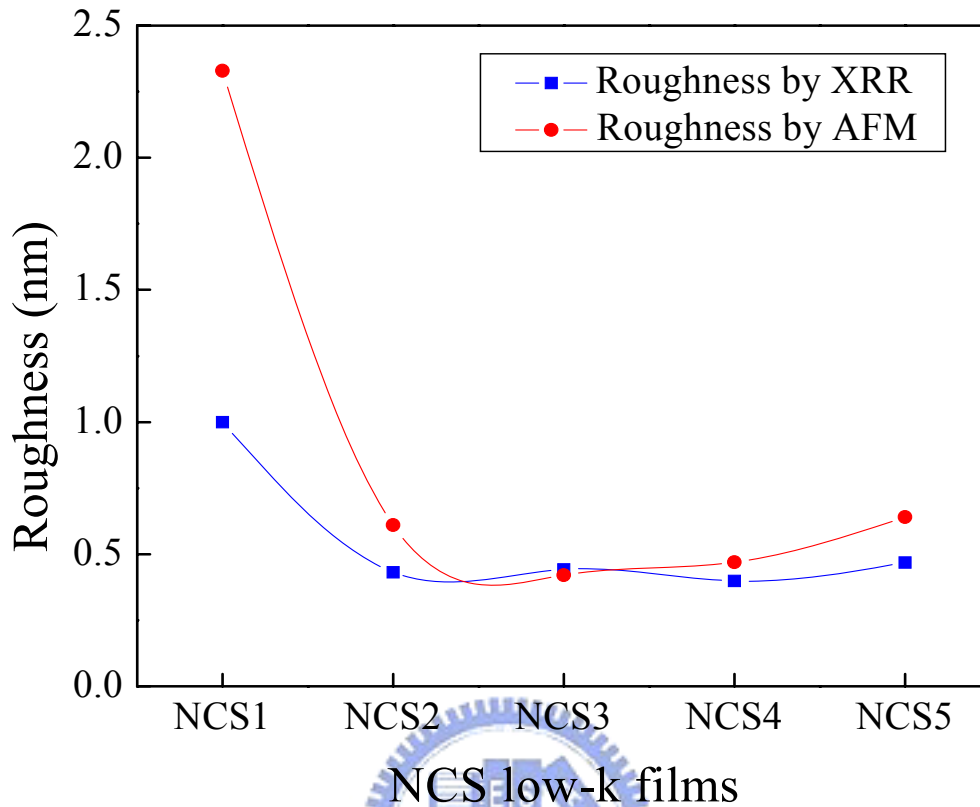
Figure 4.26 Surface Roughness measured by XRR and AFM

4.9 Summary

Chemical and molecular bonding of NCS low-k was effected by silica precursor (TEOS and MTMS) loading, higher loading of MTMS as a matrix precursor would caused lowest cross-linking because of Si-CH$_3$ bonding of MTMS was less dense compare to Si-O-Si bonding of TEOS (NCS1 low-k). The crosslink degree increase from NCS2 to NCS5 as more TEOS was added to the matrix that would increase the Si-O-Si crosslink in the balance of MTMS amount. Therefore, the silica precursor loading must attain the best composition in order to have better cross-link.

The porosity of NCS low-k film was influenced by the percentage of TPAOH added. Lower TPAOH concentration produced smaller silica cluster and smaller silica cluster can be packed more efficiently, hence producing smaller pores and result on

lower porosity. Except of TPAOH loading impact on porosity, less dense structure (more Si-CH$_3$) would also provide more free space. Thus porosity was influenced by percentage of TPAOH and less dense Si-CH$_3$ structure.

NCS2 to NCS5 revealed higher Si-O-Si matrix cross-link as interpreted by FT-IR and ^{29}Si-NMR results. The high cross-link matrix was related to the incorporation of more TEOS groups to the matrix as Si-O-Si precursor. As resulted from ^{29}Si-NMR, the Q [(SiO)$_4$Si] group availability was balanced by the existence of T [(SiO)$_3$Si(CH$_3$)] group. Therefore, for NCS2 to NCS5 the MTMS precursor was added in the relatively amount to TEOS precursor. Since TEOS and MTMS precursors would result on Q and T groups respectively. The porosity was also being controlled in the region that no pore percolation was obtained. NCS2 to NCS5 pore size are preserved in spherical shape because of higher matrix cross-link and lower porosity, therefore the matrix was rigid enough to sustain the thermal stress and only small amount of film thickness degradation was observed without causing much deterioration on pore shape.

NCS1 demonstrated the least cross-linked behavior rather than NCS2 through NCS5, as a result of its smallest quantity of Q [(SiO)$_4$Si] group, that was the key component of a fully cross-linked structure. Less cross-linked structure and higher porosity caused NCS1's matrix could not sustain the stress that come during thermal curing and collapse to form stable structure. Thermal shrinkage happened because film matrix preferred to form more stable structure. NCS1 low-k showed the highest film shrinkage compared to others NCS low-k. Since lower matrix cross-link of NCS1 and higher porosity causing thickness shrinkage during thermal curing, therefore pores degrade from initial spherical shape to elliptic cylindrical shape.

NCS1 matrix mainly composed of Si-CH$_3$ bonding that degraded the modulus significantly. NCS2 to NCS5 Si-O-Si network cross-linking and lower porosity improve the modulus. Modulus was influenced by cross-link of Si-O-Si matrix,

porosity, and pore shape   Higher degree of Si-O-Si cross-link, lower porosity, spherical pore shape have higher modulus. The main factor that influenced the modulus was the porosity. Since the modulus was decrease as the power of 3.1 with porosity increase.

Table 4.8 summarized the main property of all NCS low-k films. The dielectric constant decreased by incorporation of more methyl groups and higher porosity content. Higher elastic modulus was obtained from higher Si-O-Si matrix cross-link, lower porosity and spherical pore shape. Since κ-value of air $\sim$ 1, therefore the incorporation of pores into the Si-O-Si   matrix reduces its dielectric constant and the lower polarizability Si-CH$_3$ bond also assists the lowering of dielectric constant. NCS1 has κ=2.0 that account to its less cross-link matrix (higher Si-CH$_3$) and higher porosity. NCS2 to NCS5 matrix crosslink was improved and porosity was added in the manner of no disturbance to the modulus. Therefore, the κ=2.3 to κ=2.8 could be obtained with modulus around 10GPa. The thermal stress range decrease with increasing porosity, indicating that the introduction of more pores would allow the NCS low-k film became more compliant since the thermal stress was relieved through pores.

Table 4.8 Summarize of the properties of NCS low-k films

Sample Name	^{29}Si-NMR T	^{29}Si-NMR Q	n (refractive index)	k (Dielectric constant)	Density (g/cm^3)	Porosity (%)	Pore Shape	Pore Size (nm)	Modulus (GPa)	RMS(nm) roughness
NCS1	4	1	1.27	2.0	1.000	38.6	Elliptic cylindrical	$d\perp$ =1.9 $d_\parallel$=3.3	2.76	2.3
NCS2	0.92	1	1.29	2.3	1.185	27.6	Spherical	0.46	9.29	0.6
NCS3	0.86	1	1.30	2.4	1.194	26.9	Spherical	0.31	9.22	0.4
NCS4	0.8	1	1.32	2.7	1.220	20.5	Spherical	0.48	11.79	0.4
NCS5	0.68	1	1.32	2.8	1.325	18.7	Spherical	0.4	13.44	0.6

Chapter 5 Conclusions

The impact of chemical bonding structure, porosity on electrical, mechanical, and thermal stress property of nano-clustering silica (NCS) low-k thin film have been investigated. NCS low-k thin films have been proved to have low dielectric constant with high elastic modulus. The direct incorporation of methyl (-CH$_3$) groups by forming Si-CH$_3$ bond could replace the conventional extra-step silylation process. The higher content Si-CH$_3$ organic moieties had beneficial effect on the electrical properties of NCS low-k films.

The silica matrix TEOS/MTMS loading influenced on cross-link of Si-O-Si matrix. Higher TEOS content compared to MTMS produced higher Si-O-Si cross-link. The structure directing agent/pore generator TPAOH concentration influenced the porosity in the way that lower TPAOH concentration produced smaller silica cluster, therefore as the smaller silica cluster can be packed more efficiently, hence producing smaller pores and lower porosity.

NCS2 to NCS5 porous low-k film has κ-value ranging from κ =2.3 to κ =2.8. The silica matrix was composed by the addition of MTMS (Si-CH$_3$) in balance with TEOS (Si-O-Si). Therefore high modulus porous low-k film was obtained (E~10GPa). NCS2 through NCS5 film possessed spherical pore shape. The accommodation of Si-CH$_3$ was equilibrated by the addition of Si-O precursor, in the agreement that the Si-O-Si linkage of NCS low-k film still preserved in the present of Si-CH$_3$ groups. By adding more TPAOH, the porosity increased from NCS5 to NCS2 (micropores region enhancement) without causing much deterioration on mechanical modulus. Pore size was well controlled in the order of d<10nm with most population in the d=0.5nm.

In order to push κ-value <2.3, NCS1 porous low-k film was proposed with κ=2.0, that was obtained from less cross-link structure and higher porosity. The silica matrix

was composed by higher content of MTMS (Si-CH$_3$) instead of TEOS. But the modulus dropped to E=2.76GPa. Therefore, the incorporation of high methyl content and high porosity to NCS1 significantly reduced the κ value. Nevertheless, its Si-O-Si cross-linking was not rigid enough to sustain the thermal stress, therefore collapsed during thermal processing, formed elliptic cylindrical pore shape (d$_{in-plane}$=3.3nm d$_{out-of-plane}$=1.9nm), and ultimately devastated the elastic modulus of final thin film.

In summary, in order to reduce dielectric constant and obtain higher elastic modulus of porous NCS low-k film, the appropriate precursor loading (MTMS/TEOS/TPAOH) must be taken into consideration. Since Si-O-Si matrix cross-linking and porosity greatly influenced the final property of porous NCS low-k film such as dielectric constant and elastic modulus.

References

[1]   M. T. Bohr, *Tech. Digest IEEE Int. Electronic Device Meeting*, 241 (1995).

[2]   P. D. Moor, W. Ruythooren, P. Soussan, B. Swinnen, K. Baert, C. V. Hoof, and E. Beyne, *Mater. Res. Soc. Symp. Proc.,* **970**, 0970-Y01-02 (2007).

[3]   S. J. Martin, J. P. Godschalx, M. E. Mills, E. O. Shaffer II, and P. H. Townsend, *Adv. Mater.*, **12**, 1769 (2000).

[4]   J. L. Hedrick, R. D. Miller, C. J. Hawker, K. R. Carter, W. Volksen, D. Y. Yoon, and M. Trollsas, *Adv. Mater.*, **10**, 1049 (1998).

[5]   T. J. Shin, and M. Ree, *Macromol. Chem. Phys.*, **203**, 791 (2002).

[6]   C. V. Nguyen, K. R. Carter, C. J. awker, J. L. Hedrick, R. L. Jaffe, R. D. Miller, J. F. Remenar, H. W. Rhee, P. M. Rice, M. F. Toney, M. Trollsas, and D. Y. Yoon, *Chem. Mater.*, **11**, 3080 (1999).

[7]   T. Ramos, J. Roderick, A. Maskara, and D. M. Smith, Mat. Res. Soc. Symp. Proc., 443, 91 (1997).

[8]   A. E. Braun, Semiconductor International, Low-k Bursts Into the Mainstream... Incrementally (2005)

[9]   S. Lin, C. Jin, L. Lui, M. Tsai, M. Daniels, A. Gonzalez, J. T. Wetzel, K.A. Monnig, P. A. Winebarger, S. Jang, D. Yu and M.S. Liang, in: Proc. IITC, 146 (2001).

[11]   J. M. Paik, H. Park, and Y. C. Joo, *Microelec. Eng.*, **71**, 348 (2004).

[12]   M. Morgen, E. T. Ryan, J. H. Zhao, C. Hu, T. H. Cho, and P. S. Ho, *Annu. Rev. Mater. Sci.*, **30**, 645 (2000).

[13]   K. Mosig, T. Jacobs, K. Brennan, M. Rasco, J. Wolf and R. Augur, *Microelec. Eng.*, **64**, 11 (2002).

[14]   N. Chandrasekaran, S. Ramarajan, W. Lee, G. M. Sabde, and S. Meikle, *J. Electrochem. Soc.*, **151**, G882 (2004).

[15]   K. D. Lee, E. T. Ogawa, S. Yoon, X. Lu, and P. S. Ho, *Appl. Phys. Lett.* , **82**, 2032 (2003).

[16]   G. Dixit, L. D. Cruz, S. Ahn., Y. Zheng, J. Chang, M. Naik, A. Demos, D.

Witty and H. Msaad, *Proc. of the IEEE 2004 International Interconnect Technology Conference*, 142 (2004).

[17]   C. S. Yang and C. K. Choi, *Curr. Appl. Phys.*, **6**, 243 (2006).

[18]   A. M. Padovani, L. Rhodes, L. Riester, G. Lohman, B. Tsuie, J. Conner, S. A. B. Allen, and P. A. Kohla, *Electrochem. and Solid-State Lett.*, **4,** F25 (2001).

[19]   G. Xu, J. He, E. Andideh, J. Bielefeld, and T. Scherban, *Proc. of. The IEEE 2002 International Interconnect Technology Conference*, 57 (2002).

[20]   Z. Li, M. C. Johnson, M. Sun, E. T. Ryan, D. J. Earl, W. Maichen, J. I. Martin, S. Li, C. M. Lew, J. Wang, M. W. Deem, M. E. Davis and Y. Yan, *Angew. Chem.*, **118**, 6477 (2006).

[21]   Z. Li, S. Li, H. Luo and Y. Yan, *Adv. Funct. Mater.,* **14**, 1019 (2004).

[22]   M. Egami, *Science and Industry,* **77**, 582 (2003).

[23]   S. Nakai, M. Kojima, N. Misawa, M. Miyajima, S. Asai, S. Inagaki, Y. Iba, T. Ohha, M. Kase, H. Kitada, S. Satoh, N. Shimizu, I. Sugiura, F. Sugimoto, Y. Setta, T. Tanka, N. Tamura, M. Nakaishi, Y. Nakata, J. Nakahira, N. Nishikawa, A. Hasegawa, S. Fukuyama, K. Fujita, K. Hosaka, N. Horiguchi, H. Matsuyama, T. Minami, M. Minamizawa, H. Morioka, E. Yano, A. Yamaguchi, K. Watanabe, T. Nakamura, and T. Sugii, *Tech. Digest IEEE Int. Electronic Device Meeting*, 11.3.1 (2003).

[24]   http://www.betasights.net/wordpress/?p=540

[25]   I. Sugiura, N. Misawa, S. Otsuka, N. Nishikawa, Y. Iba, F. Sugimoto, Y. Setta, H. Sakai, Y. Koura, K. Nakano, T. Karasawa, Y. Ohkura, T. Kouno, H. Watatani, Y. Nakata, Y. Mizushima, T. Suzuki, H. Kitada, N. Shimizu, S. Nakai, M. Nakaishi, S. Fukuyama, T. Nakamura, E. Yano, M. Miyajima, and K. Watanabe, *Microelec. Eng.*, **82**, 380 (2005).

[26]   K. Ito, R. S. Yu, K. Sato, K. Hirata, Y. Kobayashi, T. Kurihara, M. Egami, H.

Arao, A. Nakashima, and M. Komatsu, *J. Appl. Phys.* **98**, 094307 (2005).

[27]   G. E. Moore, *Electronics*, **38**, 8 (1965).

[28]   J. Singh, Semiconductor Devices: Basic Principles (John Wiley & Sons, New York, 2001), Chap. 10.

[29]   "International technology roadmap for semiconductors," 2008. Update.

[30]   P. T. Liu, T. C. Chang, Y. L. Yang, Y. F. Cheng and S. M. Sze, *IEEE Trans. On Electronic Devices,* 47, 1733 (2000).

[31]   D. Edelstein, J. Heidenreich, R. Goldblatt, R. Schulz, L. Su, and J. Slattery, *IEEE Int. Electronic Device Meeting*, **1997**, 773.

[32]   R. D. Goldblatt, *Proc. of Int'l Interconnect Technology Conference*, **263**, 261 (2000).

[35]   2008 ITRS Summer Public Conf.

[36]   P. Atkins and J. de Paula, *Atkins' Physical Chemistry*, 7th ed. (Oxford University Press, New York, 2002).

[37]   S. O. Kasap, Principles of Electrical Engineering Materials and Devices (McGraw-Hill, New York, 1997), Chap. 7.

[38]   K. J. Miller, H. B. Hollinger, J. Grebowicz, and B. Wunderlich, Macromolecules, **23**, 3855 (1990).

[39]   K. Maex, M. R. Baklanov, D. Shamiryan, F. Iacopi, S. H. Brongersma, and Z. S. Yanovitskaya, J. Appl. Phys. **93**, 8793 (2003).

[40]   http://www.semiconductor.net/article/CA164243.html.

[42]   V. L. Shannon, M. Z. Karim, Thin Solid Films, **270**, 498 (1995).

[43]   M. J. Shapiro, S. V. Nguyen, T. Matsuda, D. Dobuzinsky, Thin Solid Films, **270**, 503 (1995).

[44]   C. C. Chang, S. K. J. Jian, and J. S. Chen, *J. Electrochem. Soc.,* **153**, G901 (2006).

[45]   R. H. Baney, M. Itoh, A. Sakakibara, and T. Suzukit, *Chem. Rev.*, 95, 1409 (1995).

[46]   J. Bremmer, Y. Liu, K. Gruszynski and F. Dall, *Mater. Res. Soc. Symp. Proc.*, **37**,476 (1997).

[47]   Y. Liu, J. Bremmer, K. Gruszynski and F. Dall, *VLSI Multilevel Interconnection Conf.*, **655**, 1997, Santa Clara, CA.

[48]   M. J. Loboda, *Microelectron. Eng.*, **50**, 15 (2000).

[49]   H. G. P. Lewis, D. J. Edell, and K. Gleason, *Chem. Mater.*, **12**, 3488 (2000).

[50]   Q. Wu and K. Gleason, *J. Vac. Sci. Technol. A,* **21**, 388 (2003).

[51]   A. Grill, *Thin Solid Films*, **398-399**, 527 (2001).

[52]   A. Grill and V. Patel, *Appl. Phys. Lett.*, **79**, 803 (2001).

[53]   C. C. Chiang, M. C. Chen, L. J. Li, Z. C. Wu, S. M. Jang, and M. S. Liang, *J. Electrochem. Soc.*, **151**, G612 (2004).

[54]   M. L. O'Neill, R. N. Vrtis, J. L. Vincent, A. S. Lukas, E. J. Karawacki, B. K. Peterson, and M. D. Bitner, *Mater. Res. Soc. Symp. Proc.*, **766**, E8.17.1 (2003).

[55]   A trademark of Novellus Systems (http://www.novellus.com).

[56]   A trademark of Applied Materials (www.appliedmaterials.com).

[57]   S. J. Martin, J. P. Godschalx, M. E. Mills, E. O. Shaffer II, and P. H. Townsend, *Adv. Mater.*, **12**, 1769 (2000).

[58]   M. Fayolle, G. Passemard, M. Assous, D. Louis, A. Beverina, Y. Gobil, J. Cluzel and L. Arnaud, *Microelectron. Eng.*, **60**, 119 (2002).

[59]   T. Ramos, S. Wallace, and D. M. Smith, *Mat. Res. Soc. Symp. Proc.*, **495**, 279 (1998).

[60]   C. M. Flannery, C. Murray, I. Streiter and S. E. Schulz, *Thin Solid Films*, **388**, 1 (2001).

[61]   A. Jain, S. Rogojevic, S. V. Nitta, V. Pisupatti, W. N. Gill, P. C. Wayner, J. L. Jr., T. E. F. M. Plawsky, G. S. Standaert, *Mat. Res. Soc. Symp. Proc.*, **565**, 29 (1999)

[62]   T. Ramos, K. Roderick, A. Mascara, and D. M. Smith, ''Processings of Advanced Metallization Conferences (AMC)'' Advanced Metallization and

Interconnect Systems for ULSI Applications, 445 (1996).

[63]   C. Jin, J. D. Luttmer, D. M. Smith, and T. A. Ramos, MRS Bull. **22**, 39 (1997).

[64]   K. Chung, E. S. Moyer, and M. Spaulding, U.S. Patent No. 6,231,989 (2001).

[65]   E. S. Moyer, K. Chung, M. Spauding, T. Deis, R. Boisvert, C. Saha, and J. Bremmer, *Proceedings of IITC*, 1999.

[66]   J. L. Hendrick, R. D. Miller, C. J. Hawker, K. R. Carter, W. Volksen, D. Y. Yoon, and M. Trollsas, *Adv. Mater.*, **10**, 1049 (1998).

[67]   M. Gallagher, N. Pugliano, J. Calvert, Y. You, R. Gore, N. Annan, M. Talley, S. Ibbitson, and A. Lamola, Presented at the MRS Spring Meeting, 2001.

[68]   M. L. Che, J. Leu, Y. H. Chen, C. Y. Huang, and S. Choang , *ECS Trans*., **6**, 591 (2007).

[69]   Y. F. Lu, G. Z. Cao, R. P. Kale, S. Prabakar, G. P. Lopez, and C. J. Brinker, *Chem. Mater*., **11**, 1223 (1999).

[70]   M. R. Baklanov *et al.*, *Proceedings of the Advanced Metallization Conference* Materials Research Society, Pittsburgh, PA, (2002).

[71]   M. Petkov, M. H. Weber, K. G. Lynn, and K. P. Rodbell, *Appl. Phys. Lett*., **79**, 3884 (2001).

[72]   F. Iacopi *et al.*, Microelectron. Eng. **64**, 351 (2002).

[73]   F. Ciaramella, V. Jousseaume, S. Maitrejean, M. Verdier, B. Remiat, A. Zenasni, and G. Passemard, *Thin Solid Films*, **495**, 124 (2006).

[74]   K. Chung and S. Zhang, U.S. Patent No. 6,313,045 (2001).

[75]   B. Zhong *et al.*, Presented at the MRS Spring Meeting, 2002.

[76]   Y. W. Chen, W. C. Wang,   W. H. Yu, E. T. Kang, K. G. Neoh,   R. H. Vora, C. K. Ong, L. F. Chen, C. K. Ong and L. F. Chen, *J. Mater. Chem.*, **14**, 1406 (2004).

[77]   S. Yang, P. A. Mirau, C. S. Pai, O. Nalamasu, E. Reichmanis, E. K. Lin, H. J. Lee, D. W. Gidley, and J. Sun, *Chem. Mater.*, **13**, 2762 (2001).

[78]   E. M. Freer, L. E. Krupp, W. D. Hisberg, P. M. Rice, J. L. Hendrik, J. N. Cha, R D. Miller, and H. C. Kim, *Nano Lett.*, **5**, 2014 (2005).

[79]   C. C. Yang, P. T. Wu, W. C. Chen, and H. L. Chen, *Polymer*, **45**, 5691 (2004)

[80]   C. V. Nguyen, K. R. Carter, C. J. Hawker, J. L. Hedrick, R. L. Jaffe, R. D. Miller, J. F. Remenar, H. W. Rhee, P. M. Rice, M. F. Toney, M. Trollsas, and D. Y. Yoon, *Chem. Mater.*, **11**, 3080 (1999).

[81]   Y. Toivola, S. Kim, R. F. Cook, K. Char, J. K. Lee, D. Y. Yoon, H. W. Rhee, S. Y. Kim, and M. Y. Jin, *J. Electrochem. Soc.*, **151**, F45 (2004).

[82]   B. Lee, Y. H. Park, Y. T. Hwang, W. Oh, J. Yoon, and M. Ree, Nature Materials, **4**, 147 (2005).

[83]   Q. R. Huang, W. Volksen, E. Huang, M. Toney, C. W. Frank, and R. D. Miller, *Chem. Mater.*, **14**, 3676 (2002).

[84]   S. Yang, P. A. Mirau, C. S. Pai, O. Nalamasu, E. Reichmanis, J. C. Pai, Y. S. Obeng, J. Seputro, E. K. Lin, H. J. Lee, J. N. Sun, and D. W. Gidley, *Chem. Mater.*, **14**, 369 (2002).

[85]   J. H. Yim, Y. Y. Lyu, H. D. Jeong, S. A. Song, I. S. Hwang, J. Hyeon-Lee, S. K. Mah, S. Chang, J. G. Park, Y. F. Hu, J. N. Sun, D. V. Gidley, *Adv. Funct. Mater.*, **13**, 382 (2003).

[86]   J. H. Yim, M. R. Baklanov, D. W. Gidley, H. G. Peng, H. D. Jeong, and L. S. Pu, *J. Phys. Chem. B*, **108**, 8953 (2004).

[87]   J. H. Yim, J. B. Seon, T. D. Jeong, L. Y. S. Pu, M. R. Baklanov, and D. W. Gidley, *Adv. Funct. Mater.*, **14**, 277 (2004).

[88]   A. M. Padovani, L. Rhodes, S. A. B. Allen, and P. A. Kohl, *J. Electrochem. Soc.*, **149**, F161 (2002).

[89] A. M. Padovani, L. Rhodes, S. A. B. Allen, and P. A. Kohl, *J. Electrochem. Soc.*, **149**, F171 (2002).

[90] S. Z. Yu, T. K. S. Wong, X. Hu, K. Pita, and V. Ligatchev, *J. Electrochem. Soc.*, **151**, F123 (2004).

[91] B. D. Lee, Y. H. Park, Y. T. Hwang, W. Oh, J. Yoon, and M. Ree, *Nature Materials*, **4**, 147 (2005).

[92] H. W. Ro, K. J. Kim, P. Theato, D. W. Gidley, and D. Y. Yoon, *Macromolecules,* **38**, 1031 (2005).

[93] B. J. Char, S. Kim, and K. Char, *Macromol. Res.*, **13**, 176 (2005).

[94] H. W. Ro, K. J. Kim, P. Theato, D. W. Gidley, and D. Y. Yoon, *Macromolecules*, **38***, 1031 (2005).

[95] H. W. Su, W. C. Chen, *Mat. Chem. and Phys.*, **114**, 736 (2009).

[96] A. Zenasni, F. Ciaramella, V. Jousseaume, C. L. Cornec, and G. Passemard, *J. Electrochem. Soc.,* **154**, G6 (2007).

[97] V. Jousseaume, A. Zenasni, L. Favennec, G. Gerbaud, M. Bardet, J. P. Simon, and A. Humbert, *J. Electrochem. Soc.,* **154**, G103 (2007).

[98] T.C. Chang, T.M. Tsai, P.T. Liu, C.W. Chen and T.Y. Tseng, *Thin Solid Films*, **469**, 383 (2004).

[99] A. Zenasni, B. Remiat, C. Waldfried, C. L. Cornec, V. Jousseaume, and G. Passemard, *Thin Solid Films*, **516,** 1097 (2008).

[100] N. Kemeling, K. Matsushita, N. Tsuji, K. Kagami, M. Kato, S. Kaneko, H. Sprey, D. Roest and N. Kobayashi, *Microelec. Eng.*, **84**, 2575 (2007).

[101] I. L. Berry III, C. Waldfried, and K. Durr, *Mater. Res. Soc. Symp. Proc.*, **990**, 0990-B02-01 (2007).

[102]   E. Mickler, C. T. Lin, A. T. Krishnan, C. Jin, M. Jain, *Proc. of the IEEE 2001 International Interconnect Technology Conference*, 190 (2004).

[103]   S. Li, Z. J. Li, and Y. S. Yan, *Adv. Mater.*, **15**, 1528 (2003).

[104]   S. Li, J. N. Sun, Z. J. Li, H. G. Peng, D. Gidley, E. T. Ryan, and Y. S. Yan, *J. Phys. Chem. B*, **108**, 11689 (2004).

[105]   Z. B. Wang, A. P. Mitra, H. T. Wang, L. M. Huang, Y. H. Yan, *Adv. Mater.*, **13,** 1463 (2001).

[106]   Z. B. Wang, H. T. Wang, A. P. Mitra, L. M. Huang, Y. S. Yan, *Adv. Mater.,* **13**, 746 (2001).

[107]   Z. Li, C. M. Lew, S. Li, D. I. Medina and Yan, *J. Phys. Chem. B*, **109**, 8652 (2005).

[108]   E. T. Ryan, C. Labelle, S. Nitta, N. C. M. Fuller, G. Bonilla, K. McCullough, C. Taft, H. Lin, A. Simon, E. Simonyi, K. Malone, M. Sankarapandian,D. Dunn, M. A. Zaitz, S. Cohen, N. Klymko, B. K. Moon, Z. Li, S. L, Y. Yan, J. Liu, P. S. Ho, *Mater. Res. Soc. Symp. Proc.*, **863**, B2.1.1 (2005).

[109]   S. Eslava, F. Iacopi, M. R. Baklanov, C. E. A. Kirschhock, K. Maex, and J. A. Martens, *J. Am. Chem. Soc.,* **129**, 9288 (2007).

[110]   S. Eslava, S. Delahaye, M. R. Baklanov, F. Iacopi, C. E. A Kirschhock, K. Maex, and J. A. Martens, *Langmuir*, **24**, 4897 (2008).

[111]   Y. S. Mor, T. C. Chang, P. T. Liu, T. M. Tsai, C. W. Chen, S. T. Yan, C. J. Chu, W. F. Wu, F. M. Pan, W. Lur, S. M. Sze, J. Vac. Sci. Technol. B 20 (2002) 1334-1338.

[112]   T. C. Chang, P. T. Liu, Y. S. Mor, T. M. Tsai, C. W. Chen, Y. J. Mei, F. M. Pan, W. F. Wu, and S. M. Sze, *J. Vac. Sci.,Technol. B.*, **20**, 1561 (2002).

[113]   R. M. de Vos, W. F. Maier, and H. Verweij, *J. Membr. Sci.*, **158**, 277 (1999).

[114]   S. Eslava, C. E. A. Kirschhock, S. Aldea, M. R. Baklanov, F. Iacopi, K.

Maex, and J. A. Martens, Microporous and Mesoporous Materials, **118**, 438 (2009).

[115]   R. Aelion, A. Loebel, and F. Eirich, *J. Am. Chem. Soc.*, **72**, 5705 (1950)

[116]   G. Dixit, L. D. Cruz, S. Ahn, Y. Zheng, J. Chang, M. Naik, A. Demos, D. Witty and H. Msaad, *Proc. of the IEEE 2004 International Interconnect Technology Conference*, 142 (2004).

[117]   N, Tajima, T. Ohno, T. Hamada, K. Yoneda, S. Kondo, N. Kobayashi, M. Shinriki, Y. Inaishi, K. Miyazawa, K. Sakota, S. Hasaka, and M. Inoeu, Jpn. J. Appl. Phys., 46, 5970 (2007).

[118]   C. S. Yang, and C. K. Choi, *Curr. Appl. Phys.*, **6**, 243 (2006).

[119]   S.M. Bilodeau, A.S. Borovik, A.A. Ebbing, D.J Vestyck, C. Xu, J.F. Roeder, and T.H. Baum, *Mat. Res. Soc. Symp. Proc.*, **812**, F6.18.1 (2004).

[120]   L.L. Chapelon, J. Vitiello, D. Neira, J. Torres, J.C. Royer, D. Barbier, F. Naudin, G. Tas, P. Mukundhan, and J. Clerico, *Microelec. Eng.*, **8**3, 2346 (2006).

[121]   K. H. Lee, J. H. Yim, and M. R. Baklanov, *Microporous and Mesoporous Materials*, **94**, 113 (2006).

[122]   J.B. Vella, A.A. Volinsky, I.S. Adhihetty, N.V. Edwards, and W.W. Gerberich, *Mat. Res.Soc. Symp. Proc.,* **716**, B12.13.1 (2002).

[123]   M. P. Petkov, *Mat. Res. Soc. Symp. Proc.*, **731**, W5.20.1 (2002).

[124]   Y. Liu, A. Knorr, W. L. Wu, D. Gidley, and B. Kastenmeier, *Mater. Res. Soc. Symp. Proc.*, **863**, B3.1.1 (2005)

[125]   N. Aoi, T. Fukuda and H. Yanazawa: Proc. Int. Interconnect Technology Conf., 72 (2002)..

[126]   D.W. Krevelen, *Properties of Polymers, 3rd edn.*, Elsevier, New York, (1990).

[127]   S. Li, *Proc. IEEE Int. Interconnect Technol. Conf.*, 146, (2001).

[128]   S. Yang, P. A. Mirau, C. S. Pai, O. Nalamasu, E. Reichmanis, E. K. Lin, H. J. Lee, D. W. Gidley, and J. N. Sun, *Chem. Mater.*, **13**, 2762 (2001).

[129]   S. Eslava, M. R. Baklanov, A. V. Neimark, F. Iacopi, C. E. A. Kirschhock, K. Maex, and J. A. Martens, *Adv. Mater.*, **20**, 3110 (2008).

[130]   M. H. Ree, J. W. Yoon, and K. Y. Heo, *J. Mater. Chem.*, **16**, 685 (2006).

[131]   P. Zaumseil, Innovations for High Performance Microelectronics, 497, Frankfurt (Oder) / Germany.

[132]   http://staff.chess.cornell.edu/~smilgies/gisaxs/GISAXS.php
[133]   W. C. Oliver and G. M. Pharr, *J. Mater. Res.*, **7**, 1564 (1992).

[134]   G. G. Stoney, *Proc. R. Soc. Lond. A*, **82**, 172 (1909).

[135]   A. Grill, and D.A. Neumayer, J. Appl. Phys., **94**, 6697(2003).

[136]   K. M. Williams, J. Huang,, M. Schulberg, and P. V. Cleemput : IEEE (2001).

[137]   T. Abell, K. Houthoofd, F. Iacopi, P. Grobet and K. Maex, *Mat.Res.Soc.Symp.Proc.*,**863**, B1.8.1 (2005).

[138]   W. L. Wu, W. E. Wallace, E. K. Lin, G. W. Lynn, C. J. Glinka, E. T. Ryan, and H. M. Ho, *J. Appl. Phys.*, **87**, 1193 (2000).

[139]   B. Lee, J. Yoon, W. Oh, Y. Hwang, K. Heo, K. S. Jin, J. Kim, K. W. Kim, and M. Ree, *Macromolecules*, **38**, 3395 (2005).

[140]   S. W. Yeh, K. H. Wei, Y. S. Sun, U. Jeng, K. S. Liang, *Macromolecules*, **37**, 12 (2004).

[141]   S. W. Yeh, K. H. Wei, Y. S. Sun, U. Jeng, K. S. Liang, *Macromolecules.*, **37**, 12 (2004).

[142]   E. Y. Sheu, *Phys. Rev. A.*, **45**, 2428 (1992).

[143]   A. Guinier and G. Fournet, Small Angle Scattering of X-Rays, (Wiley, New York, 1955).

[144]   G. Porod, Small Angel X-ray Scattering, (Academic Press INC., London, New York, Eds, O.Glatter; O. Kratky, 1980). p. 17.

[145]   U. S. Jeng, Y. S. Sun, H. J. Lee, C. H. Hsu, K. S. Liang, S. W. Yeh, K. H. Wei, *Macromolecules.*, **37**, 4617 (2004).

[146]   D. H. Evertt, *Pure Appl. Chem.*, **31**, 579 (1972).

[147] V. Jousseaume, C. L. Cornec, F. Ciaramella, L. Favennec, A. Zenasni1, G. Simon, J. P. Simon, G. Gerbaud, and G. Passemard, *Mater. Res. Soc. Symp. Proc.,* **914**, 0914-F04-06 (2006).

[148] R.W. Rice, *J. Mater. Sci.*, **40**, 983 (2005).

[150] L. J. Gibson and M. F. Ashby, *Cellular Solids: Structure and Properties*, 2nd ed., Cambridge Univ. Press, Cambridge, UK (1997).

[151] K. K. Phani, S. K. Niyogi, and A. K. De, J. Mater. Sci. Lett., 7, 1253 (1988)

[152] H. Miyosi, H. Matsuo, Y. Oku, H. Tanaka, K. Yamada, N. Mikami, S. Takada, N. Hata and T. Kikkawa, *Jpn. J. Appl. Phys.*, **43**, 498 (2004).

[153] R. E. Williford, X. S. Li, R. S. Addleman, G. E. Fryxell, S. Baskaran, J. C. Birnbaum, C. Coyle, T. S. Zemanian, C. Wang and A. R. Courtney, *Microporous and Mesoporous Materials*, **85**, 260 (2005).

[154] N. Aoi, T. Fukuda and H. Yanazawa, Proc. Int. 2002 Interconnect Technology Conf., California, 2002 (IEEE Press, New Jersey, 2002) p. 72.

[155] H. Miyoshi, H. Matsuo, Y. Oku, H. Tanaka, K. Yamada, N. Mikami, S. Takada, N. Hata and T. Kikkawa, *Jpn. J. Appl. Phys.*, **43**, 498 (2004).

[156] H. Miyoshi, H. Matsuo, H. Tanaka, K. Yamada, Y. Oku, S. Takada, N. Hata and T. Kikkawa, *Jpn. J. Appl. Phys.*, **44**, 1161 (2005).

[157] R. W. Rice, *J. Mater. Sci.*, **28**, 2187 (1993).

[158] C.W.Bert, *J. Mater. Sci.*, **20**, 2220 (1985).

[159] A. P. Roberts and E. J. Garboczi, J. Am. Ceram. Soc., 83, 3041 (2000).

[160] H. W. Ro, K. Char, E. Jeon, H. J. Kim, D. Kwon, H. J. Lee, J. K. Lee, H. W. Rhee, C. L. Soles, and D. Y. Yoon, *Adv. Mater.*, **19**, 705 (2007).

[161] J. Kovacik, *J. Mater. Sci. Lett.*, **18,** 1007 (1999).

[162] S. Eslava, C. E. A. Kirschhock, S. ALdea, M. R. Baklanov, F. Iacopi, K. Maex, and J. A. Martens, Microporous and Mesoporous Materials, 118, 458 (2009).